1997

Experimental and theoretical investigation of tandem laser welding

Michael Richard Frewin
University of Wollongong

EXPERIMENTAL AND THEORETICAL INVESTIGATION OF TANDEM LASER WELDING

by

M. R. Frewin (BE Hons, BA Hons)

Submitted in completion of the
requirements for the degree of
Doctor of Philosophy
in the School of Materials Engineering
at the University of Wollongong

July 1997

DECLARATION

I hereby declare that the work presented in this thesis has not been submitted to any other university or institution for a higher degree and that due credit has been assigned where the work of others has been described.

Michael R. Frewin.

ACKNOWLEDGMENTS

I am very grateful to my supervisors, Professor D.P. Dunne and Dr D.A. Scott, for their support and guidance throughout all stages of this work. I also wish to thank Mr D.F. Bicleanu for many invaluable discussions during the course of my study. I am indebted to Mr J. Baumer and Mr L. Garcia for their expertise in the use of the Nd:YAG laser, as well as Mr G. Tillman and Ms S.B. Emms for their technical assistance in the fields of optical and scanning electron microscopy. Special thanks are due to my parents and wife for their endless support and encouragement.

I wish to acknowledge the financial support provided by the Cooperative Research Centre for Materials Welding and Joining, incorporating C.S.I.R.O. Division of Manufacturing Technology, the University of Wollongong and B.H.P. Research Port Kembla.

SYNOPSIS

This thesis presents a comparative study of single- and tandem-beam welding with a pulsed Nd:YAG laser. When two beams from the same laser are used in tandem to weld a material, it is the intensity distribution of the composite processing beam which is important. This is similar to being able to select the mode of the laser beam, as the relative intensities, spacing and spot sizes of the two beams can be varied. The potential benefits of such a scheme over single-beam laser processing were determined to be the removal of potential contaminants to the weld with a minor beam ahead of the main welding beam; the ability to control the heating and cooling rates of the workpiece by employing a minor beam to effectively pre-heat or post-heat the weld; an improvement in the microstructure and formability of the steel welds examined in this study; and the modification of the penetration characteristics of single-beam laser welding with the same total power.

Although correlations of welding parameters with the metallurgical features of conventional fusion welds are well established, information on process-structure-property relationships associated with pulsed laser welds is more limited. A characterisation of weld metal and heat-affected zone microstructures observed in laser-welded AISI 1006 steel and two types of coated steel was therefore performed. Single- and tandem-beam Nd:YAG laser welds in the bead-on-plate configuration were used for this purpose, both in overlapping and non-overlapping bead configurations. As very rapid heating and cooling cycles occur during laser welding, the microstructures observed in the weld metal were the result of rapid solidification producing thin columnar austenite grains extending from the fusion boundary, which transformed to martensite and/or ferritic products during fast cooling to ambient temperature. The heat-affected zone structure in the base plate was also rationalised in terms of the rapid thermal cycling experienced. The intercritical reheated subzone was found to be the dominant region in the heat-affected zone of both the single- and tandem-beam welds, with the former displaying narrower heat-affected zones. Since microstructural development has a critical effect on the mechanical properties of welds, microstructural

characterisation has played an integral role not only in understanding pulsed laser welding, but also in the selection of optimum welding conditions for each material.

As an aid in the understanding of pulsed laser welding, three-dimensional numerical and analytical models of the heat flow during both single- and tandem-beam pulsed laser welding of AISI 1006 steel were developed. Model predictions of fusion zone and heat-affected zone dimensions were compared with experimental measurements. Each model was tested on a material with quite different thermophysical properties, namely A5005 aluminium alloy. Full thermal histories were also generated, and the consequences of such predictions were correlated with the microconstituents of the welds formed. A more direct check of the theoretical work, apart from the measurement of weld bead dimensions and the consequent estimations of temperature contours, was the direct comparison of temperature-time predictions with pyrometric measurements of the surfaces of sheet steel during welding. The measured temperatures were in reasonable agreement with model predictions.

The experimental, numerical and analytical results have already assisted researchers within the Cooperative Research Centre for Materials Welding and Joining to design a new type of laser processing head. This welding head gives the same performance as two separate fibres and heads, while making use of the output from a single optical fibre. It can accept a standard optical fibre, collimate the diverging laser beam, divide this laser beam into two, and then refocus each beam individually onto the material being welded. This tandem fibre-optic laser welding head offers the potential to achieve higher weld quality in laser-weldable materials, and to allow the welding of presently difficult-to-weld materials.

The development of new numerical and analytical models of pulsed laser welding, and the characterisation of weld metal microstructures in coated and uncoated steels, represent a significant contribution to the field of laser welding. By interweaving experimental and modelling strands, a much better understanding of the complex processes of both single- and tandem-beam pulsed laser welding has been achieved.

TABLE OF CONTENTS

PUBLICATIONS UNDER CANDIDATURE

1. Frewin, M.R. and Scott, D.A. "Review of analytical and numerical modelling techniques for continuous and pulsed laser welding", in *Proc. Int. Conf. on Materials in Welding and Joining*, pp. 131-136, Adelaide, Aug. 1995, Institute of Metals and Materials Australasia, Melbourne, 1995.

2. Frewin, M.R. and Scott, D.A. "Numerical and experimental investigation of pulsed Nd:YAG laser welding", in *Proc. 14th Int. Cong. on the Applications of Lasers and Electro-Optics* (eds J. Mazumder, A. Matsunawa and C. Magnusson), pp. 904-913, San Diego, California, Nov. 1995, Laser Institute of America, Orlando, Florida, 1995.

3. Frewin, M.R., Dunne, D.P. and Scott, D.A. "Microstructural characterisation of pulsed Nd:YAG laser welds in AISI 1006 steel", in *Proc. 2nd Int. Seminar and Exhibition on Materialography*, pp. 39-44, Sydney, May 1996, Institute of Metals and Materials Australasia, Melbourne, 1996.

4. Frewin, M.R., Scott, D.A. and Dunne, D.P. "Numerical and experimental investigation of tandem pulsed Nd:YAG laser welding", in *Proc. 15th Int. Cong. on the Applications of Lasers and Electro-Optics* (eds W. Duley, K. Shibata and R. Propawe), pp. 214-223, Detroit, Michigan, Oct. 1996, Laser Institute of America, Orlando, Florida, 1996.

5. Frewin, M.R. and Scott, D.A. "Laser Welding, Part I - Review of analytical and numerical modelling techniques for continuous and pulsed laser welding", submitted to *Welding Journal*, June 1997.

6. Frewin, M.R. and Scott, D.A. "Laser Welding, Part II - Finite element model for a pulsed heat source", submitted to *Welding Journal*, June 1997.

7. Frewin, M.R., Dunne, D.P. and Scott, D.A. "Structural evolution of pulsed Nd:YAG laser welds in AISI 1006 steel", submitted to *Science and Technology of Welding and Joining*, July 1997.

8. Scott, D.A., Frewin, M.R., Baumer, J. and Emms, S.B. Tandem fibre-optic laser welding, Australian Welding Research Report No. 10, Cooperative Research Centre for Materials Welding & Joining and the Welding Technology Institute of Australia, Sydney, Aug. 1995.

CHAPTER 1

INTRODUCTION

1.1 BACKGROUND

The use of intense laser radiation to weld materials is not just an alternative to conventional heat sources, but rather it offers the possibility to fabricate components from difficult-to-weld materials, often in configurations in which either distortion or access precludes the use of conventional welding techniques[1]. Moreover, laser welding is suited to high-speed production welding, and is a non-contact, low energy input process which gives rise to a fine-scale, rapidly solidified weld zone microstructure.

The standard arrangement for laser welding is shown in Figure 1.1. The beam from the laser is directed to the workpiece using mirrors. Just before reaching the workpiece the beam is focussed using a lens to increase the power density. Some of the electromagnetic radiation of the laser beam is reflected, while the rest is absorbed by the material and converted into heat energy, raising its temperature. With increasing power density, the material may melt, vaporise or ionise to form a plasma. Welding is normally performed with the material to be welded positioned near the focal point of the lens where the power density is a maximum. Coaxial to this beam a gas shroud is often employed, so an inert shielding gas can be directed over the weld to prevent reaction of the hot metal with the surrounding atmosphere. This gas also serves to protect the optics from weld spatter and fume. The material to be welded is clamped onto an x-y-z table which is moved under the beam to follow the joint line. The table is controlled by a Computer Numerical Controller (CNC) which is usually connected to the laser controller.

The two main types of laser currently used in this field are the carbon dioxide (CO_2) laser and the solid-state neodymium-doped yttrium-aluminium-garnet (Nd:YAG) laser[2-5]. In CO_2 lasers the active medium is a mixture of carbon dioxide, helium and nitrogen, which is electrically excited to produce laser radiation of wavelength 10.6 μm. Such lasers are commercially available with output powers up to 25 kW. Most of the lasers used for high-productivity welding are in the 2 to 5 kW range[6-9]. They can deliver power continuously (continuous wave) or in a series of pulses. Lasers incorporating both operating modes are available, but cw CO_2 lasers are the most common.

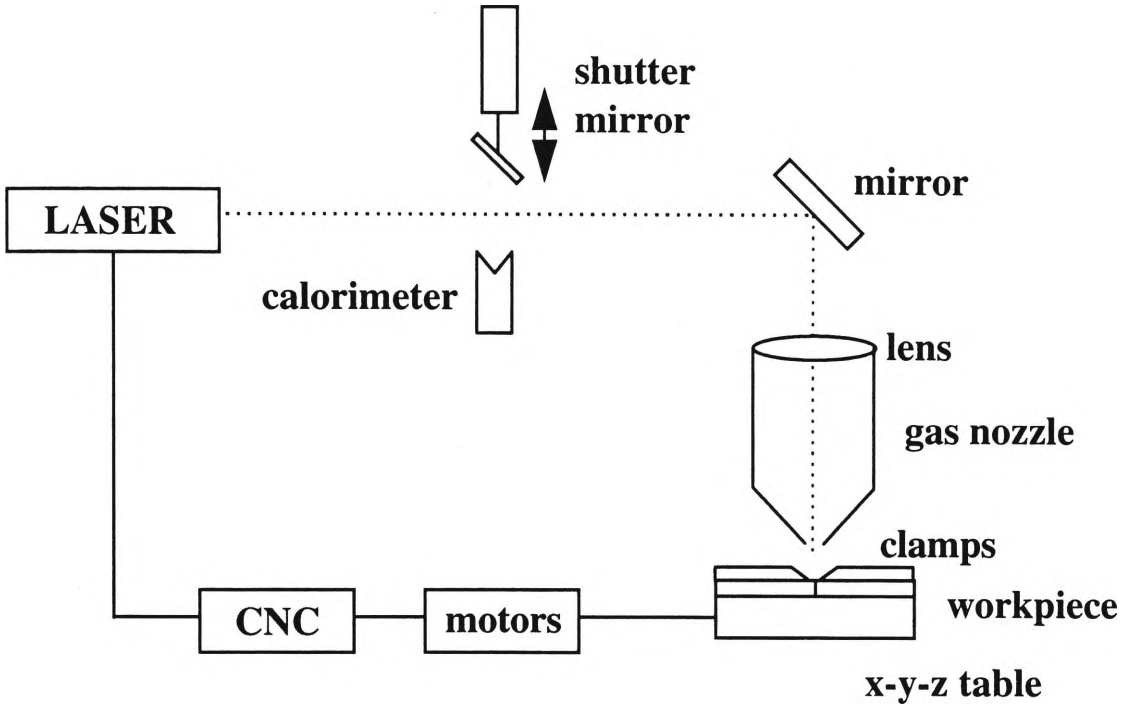

Figure 1.1 Laser welding using conventional optics.

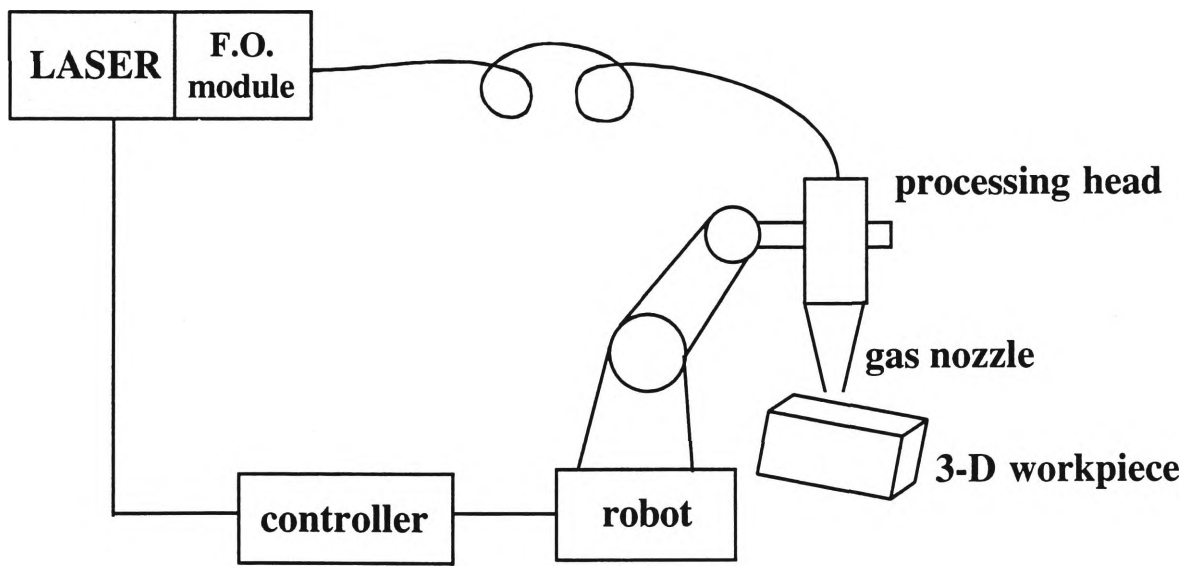

Figure 1.2 Fibre-optic laser welding with a robot.

Nd:YAG lasers contain about 1 vol% of neodymium dopant. This is the active medium in the YAG host crystal and when excited by an electric discharge lamp, the Nd^{3+} ions in the YAG crystal produce laser radiation of wavelength 1.06 μm, one tenth the wavelength of CO_2 lasers. Pulsed, cw and combined output lasers are commercially available. The maximum average power is currently around 3 kW for both pulsed and cw lasers[10,11].

The 1.06-μm wavelength of the Nd:YAG laser is transmitted with little attenuation through glass and so allows beam transmission using optical fibres[12-17]. For this reason, conventional transmissive optics used in CO_2 lasers can be replaced with a fibre-optic cable which is connected directly to the laser (Figure 1.2). The beam is focussed by lenses into the end of the fibre and is subsequently refocussed onto the workpiece as the beam emerges from the fibre. A processing head accommodates these lenses and the connection to the fibre. The fibre-optic delivery system is often connected to a robot which can move the processing head over a three-dimensional workpiece and therefore process in difficult-to-access regions. This system also allows laser processing to occur remote from the laser, and more than one optical fibre can be connected to the laser to service multiple workstations. The advent of industrial high-power Nd:YAG lasers, coupled with their ability to be delivered to workstations via optical fibres, has made such flexible systems increasingly popular in recent years.

There is not only a growing interest in this very versatile type of arrangement, but there is also a need for a deeper understanding of the interaction of Nd:YAG laser radiation with matter. Many of the new physical, chemical and metallurgical phenomena associated with this technology are poorly understood, even though their effects often lead to a reduction in the overall efficiency and efficacy of the process. Correlations of welding parameters with the metallurgical features of conventional fusion welds in low-carbon steels are well established, whereas information on process-structure-property relationships associated with continuous or pulsed laser welds is more limited.

Moreover, there have been many models which have sought to elucidate the physical mechanisms involved in conventional welding processes; there exist fewer models of continuous or pulsed laser welding[18]. A knowledge of the heating and cooling

rates is essential for predicting microstructural changes, the size of fusion and heat-affected zones, distortion, residual stress fields and mechanical properties.

The development of these models involves the formulation of mathematical equations which describe the complex physical processes of heat and mass transfer. These equations can be solved by analytical or numerical techniques. Numerical methods typically involve finite element or finite difference approaches. Such models are necessary when closed-form solutions cannot be produced because of complex initial conditions, boundary conditions and geometries. Even if a solution can be obtained, a numerical evaluation may still be required, which may be as complex as the full numerical solution of the problem. This does not imply that numerical solutions are always preferable to analytical solutions, for the latter usually offer greater insights into the solution, its overall behaviour and the parameter dependence of the problem.

1.2 STATEMENT OF OBJECTIVES

The first objective of the present study was to address the need for more comprehensive process-structure-property relationships associated with pulsed laser welds in low-carbon steel. To achieve this objective, a characterisation of fusion zone (FZ) and heat-affected zone (HAZ) microstructures observed in laser-welded AISI 1006 steel was performed. Autogenous Nd:YAG laser welds in both bead-on-plate and butt configurations were used for this purpose. Both overlapping and non-overlapping spot weld arrangements were considered. As very rapid heating and cooling cycles occur during pulsed laser welding, the microstructures observed in the weld metal were explained in terms of the rapid thermal cycling experienced.

The second objective was to model, using both numerical and analytical approaches, the thermal history of a laser weld. The model predictions of weld zone dimensions were compared with experimental measurements of weld beads on AISI 1006 steel. A further check was to measure the time dependence of the surface temperature of the steel using a fast optical pyrometer. To fully assess the capabilities and limitations of the numerical and analytical models of pulsed laser welding, an

aluminium alloy of commercial importance (A5005) was incorporated into the study. The measured weld bead dimensions were compared with the models' calculations in order to assess the predictive accuracy of the models for a material with very different thermal properties.

The third objective was to investigate the possibility of employing two laser beams for welding. As a laser beam is focussed to a very small diameter, a very high power density is achieved. Although this results in a relatively small weld diameter, small heat-affected zone and deep penetration, the high cooling rates can produce brittle microstructures and weld defects. For this reason, the workpiece can be pre-heated in a furnace. This step is not only time-consuming, but can also affect the mechanical properties of the base metal. An alternative technique is to use a pre-heat beam located ahead of the main welding beam. By varying the distance between the two beams, it is possible to control the thermal cycles experienced by the weld zone.

Moreover, when two beams from the same laser are used in tandem to weld a material, it is the intensity distribution of the composite processing beam which is important. This is similar to being able to select the mode of the laser beam, as the relative intensities, spacing and spot sizes of the two beams can be varied. The additional benefits such a scheme may produce over single-beam laser processing are:

- the possibility of removing paint and anti-corrosion coatings, which may be considered as contaminants, with a minor beam ahead of the main welding beam; and

- the modification of the speed and penetration characteristics of single-beam laser welding with the same total power.

In this study the numerical and analytical models of single-beam pulsed laser welding were extended to consider the presence of a second beam located before or after the main welding beam. Model predictions of fusion zone and heat-affected zone dimensions were compared with experimental measurements of weld beads on AISI 1006 steel. Pulsed Nd:YAG laser welds were again used for this purpose, both in overlapping and non-overlapping spot weld arrangements. The microstructures observed

in the weld metal were explained in terms of rapid solidification theory. The results of this work were used as an aid in selecting optimum laser conditions for welding AISI 1006 steel in the butt configuration.

Finally, these experiments were extended to consider bead-on-plate and butt welding of two different types of coated steel, namely:

- zinc-coated deep-drawing steel; and
- zinc/aluminium alloy-coated structural steel.

These coated steels are of commercial importance and were supplied by BHP Sheet and Coil Products. For each coated steel, an optimum tandem-beam arrangement was determined to provide sufficient zinc and aluminium ablation prior to welding. Hardness, tensile and formability tests were performed to assess the quality of the welds. A comparative study between single- and tandem-beam welding was also undertaken.

1.3 THESIS OUTLINE

In Chapter 2 of the present study a survey of the published literature pertaining to laser welding is presented. This area is of interest not only to the scientific community, whose goal it is to understand the physical processes which occur, but also to the industrial community in which lasers now play an important and growing role in the manufacturing sector. The needs and aims of these two communities are inextricably linked. Industry requires fast, efficient, cost-effective and flexible manufacturing techniques in order to increase its market and profit. In such a highly technological field as industrial lasers, maximising the serviceability and reliability of the laser in industrial applications depends upon advances in understanding the laser-material interaction process, and thereby improving its efficiency and effectiveness[1].

In Chapter 3, a description of the experimental design used in the present study is provided, and the materials chosen to fulfil this design. The methods of assessment

employed to characterise the observed laser welds are described. The results of the study are presented and discussed in Chapter 4.

Chapter 5 presents the numerical and analytical models of single- and tandem-beam pulsed laser welding. The results of these models are compared with experimental measurements. A précis and discussion of all the modelling and experimental results are then presented in Chapter 6. The implications of the present study are also discussed. The conclusions and recommendations for further study are presented in Chapter 7.

CHAPTER 2

LITERATURE REVIEW

2.1 INTRODUCTION

This chapter presents a review of literature pertaining to experimental and theoretical investigations of both single- and tandem-beam laser welding. Section 2.2 starts with a general description of the physical mechanisms associated with the absorption of intense laser radiation. A thorough understanding of these mechanisms is a prerequisite to exploiting the advantages of laser welding. In section 2.3 the operating characteristics of single-beam laser welding are described. This knowledge then allows the identification of the areas in which processing with two beams may be advantageous.

At the present time, lasers are currently being employed to weld some of the more common metals used in fabrication[6]. The problems currently encountered when welding these materials with a single laser beam are outlined in section 2.4. Finding solutions to these problems and widening the applicability of the laser to newer structural materials such as aluminium and magnesium alloys depends on theoretical studies of laser-material interactions, combined with a wealth of empirical data on their processing characteristics. Only a combination of calculations predicting the individual, interacting physical processes with experimental evidence will allow a full understanding of the process.

Section 2.5 presents a review of various heat transfer models for continuous and pulsed laser welding with a single beam. This review is not intended to be exhaustive; rather, it offers a selection of the pioneering attempts to model the laser welding process. Inherent problems and shortfalls are discussed, as well as possible solutions and improvements.

Section 2.6 presents a review of tandem-beam experiments and models. The potential benefits of using two laser beams to overcome some of the problems associated with single-beam laser welding are also described. As part of the present study involves the characterisation of laser weld microstructures, a discussion of the literature pertaining to laser weld metallurgy is then provided in section 2.7. Finally, the concluding remarks of section 2.8 reveal how the present study will contribute to the field of laser welding.

2.2 FORMATION OF LASER WELDS

The interaction of intense laser radiation with a material is a dynamic process. When a laser beam is focussed at or near the surface of a material, rapid heating of the material occurs[19-22]. Much of the laser radiation is reflected, but the small amount absorbed can cause the material to melt, vaporise or even ionise to form a plasma. Depending on the power density, either a conduction or keyhole weld is formed[23].

In conduction welding, the power density is insufficient to cause the material to vaporise. The laser beam is absorbed at the surface of the material, and the transfer of energy into the material is by thermal convection and conduction. This results in a weldment whose width is approximately twice the penetration depth.

In keyhole welding, the incident power density is high enough to cause vaporisation, and a "keyhole" is formed in the material which is kept open by the high vapour pressure of the suddenly vaporised solid (Figure 2.1). The absorptivity of this vapour at the laser wavelength is usually much higher than that of the solid, and so more efficient transfer of energy to the material is possible. The energy of the laser beam, absorbed by the vapour (and some plasma), is then transferred to the surrounding liquid walls of the keyhole.

The amount of laser power entering the keyhole is determined by the simple overlap of the laser spot with the keyhole itself. The major absorption mechanisms are Fresnel absorption at the walls of the molten material[24], as well as absorption and scatter by the vapour/plasma particles. The energy absorbed by the particles is kinetically transferred to the walls of the keyhole, which are heated to around the boiling point of the material, thus providing the evaporation necessary to keep the keyhole open.

At low power densities the keyhole does not penetrate fully through the material. Inadequate energy coupling may even cause the keyhole to collapse. On the other hand, at very high power densities a plume of metal vapour and plasma may form above the surface of the material, causing scatter and back-reflections of the laser light.

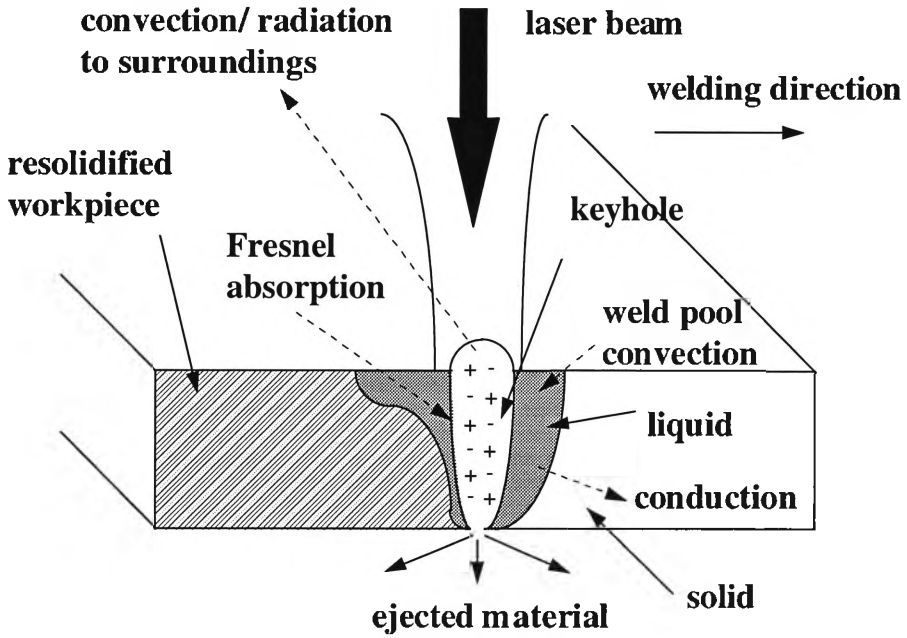

Figure 2.1 Mechanisms of keyhole welding.

During keyhole welding with a continuous laser, a stable column of vapour and plasma is formed within the material. During pulsed laser welding, however, the plasma-filled keyhole forms and dissipates prior to the subsequent laser pulse. These conditions can still be described by models used for continuous laser welding with appropriate modifications. Although some interactions are dependent on the laser wavelength, the physical principles of the interaction of intense laser radiation with materials remain the same.

During laser welding, the presence of a plasma-filled keyhole plays a very important role[25]. The mechanisms of absorption within the keyhole have been the subject of many papers[26-28]. Herziger[29] has summarised many of the theoretical treatments of these phenomena until the early 1980s. Understanding the basics of this absorption process is important to all laser applications, and in particular to laser welding where careful control of the laser parameters is essential to achieve sound welds.

2.3 CHARACTERISTICS OF SINGLE-BEAM LASER WELDING

2.3.1 Power

The depth of penetration during laser welding is a strong function of the laser power density. In the two extremes of laser power, lack of penetration will occur at low laser powers; at high powers dropout of the molten material will occur under the influence of gravity. In the intermediate range various effects such as undercut, "ropiness" and "humping" can occur[30]. Swift-Hook and Gick[25] have modelled the formation of a keyhole weld during continuous laser welding, and have found that for fixed laser power the weld penetration is inversely proportional to the speed of processing. Despite the theory having a number of simplifying assumptions, this prediction is largely supported by experiment[31]. In the case of pulsed lasers, the welding speed is mainly determined by the pulse repetition rate, the spot size and the desired overlap[32, 33]. Speed is largely independent of power.

2.3.2 Spot size and mode

When the laser beam is focussed onto the surface of the workpiece, a circular spot weld is usually produced. The area of this spot is termed "spot size". The "mode" of the laser beam influences the distribution of the laser power within the spot. Both parameters determine the power density incident on the workpiece, and therefore have a large bearing on the resulting weld. The Gaussian or TEM_{00} mode will give the best penetration for fixed laser power as it is the mode which has the highest power density and focussability[4].

It is primarily the laser source itself, consisting of the laser mirrors, apertures and the geometry of the lasing medium, which determines the mode of the laser. Unless specifically designed to be so, this cannot be changed by the laser operator. On the other hand, the spot size of the laser, within the optical constraints of the raw laser beam, is determined by the optics employed by the laser operator. The diameter and focal length of the objective lenses and the position of the workpiece in relation to the focal position are the major parameters which affect the spot size on the workpiece. Fine tuning of the optical train, for instance by the use of achromatic lenses, is also possible. The use of different optical fibres, such as stepped-index or graded-index fibres, can also change the power distribution of the laser beam.

As different modes affect the laser welding characteristics, so too can two overlapping laser beams have an effect on the processing characteristics. The "mode" and "spot size" of the processing beam in tandem fibre-optic processing effectively become user-selectable, and therefore characteristics of the resultant weld can be modified[34].

2.3.3 Wavelength

The absorption of laser radiation is governed not only by the thermophysical properties of the material, but also by the wavelength of the electromagnetic radiation. Below the melting temperature, the surface reflectivity of the solid material will determine the amount of laser radiation absorbed. At higher temperatures the higher

absorptivity of vaporised and ionised phases of the material overrides the wavelength dependence of the solid material. Different physical mechanisms are therefore responsible for the absorption of laser radiation during keyhole welding. In conduction-limited welding, where the surface reflectivity is important, the lower reflectivity of most metals at shorter wavelengths favours processing with Nd:YAG lasers rather than CO_2 lasers. During keyhole welding, metal vapour absorbs and scatters CO_2 laser radiation more than Nd:YAG laser radiation. This makes keyhole welding with Nd:YAG lasers slightly less efficient than with CO_2 lasers, although Nd:YAG lasers are less susceptible to plasma scattering and defocussing above the weld. These effects are discussed in more detail in Section 2.3.7.

2.3.4 Focal position

For maximum penetration, the focal position of the laser beam should be located at or below the surface of the material[35]. The distance into the material is determined by the power density required to achieve keyholing: for a given laser power and welding speed, keyholing will occur for a certain beam spot size (and all sizes less than that), which corresponds to a range of focal positions above and below the focal position. When the focus is set within the material, at a distance corresponding to the maximum spot size (minimum power density) for keyholing, this condition ensures that this minimum power density is maintained for the maximum distance into the workpiece.

2.3.5 Welding speed

The welding speed determines the energy per unit length that is delivered to the material. Consequently, it directly affects the amount and rate at which heat is absorbed by the material. This in turn affects the shape of the weld bead, and the amount and type of gas shielding required for the weld[36].

2.3.6 Joint tolerances

As the spot size of a laser beam is very small (typically 1-2 mm in diameter), close-fitting joint configurations are necessary if consistent welds are to be produced. The maximum allowable tolerance is largely a function of the beam diameter and the thickness of the parts to be welded. By employing a slightly larger beam diameter, more of the material can be melted, thereby allowing larger gaps. For butt welding, the maximum gap size is generally about one tenth of the thickness of the material to be welded. For lap welding, tolerances on mismatch and gap are less stringent, being about one quarter of the thickness of the parts being welded[37].

2.3.7 Shielding gas

An inert shielding gas is normally employed to protect the weld pool from oxidation. Laser welding of some materials may be performed without a gas shield if surface oxidation is acceptable. In the case of keyhole welding, the presence of plasma above the material can be detrimental to the welding process, as it can absorb and scatter the laser radiation before it reaches the workpiece. A shielding gas with a high ionisation potential therefore offers the additional advantage of being able to absorb a lot of energy from the hot metal vapour without ionising, thereby reducing the plasma density.

Two important considerations are the flow rate of the shielding gas and the nozzle design. Their selection must not lead to rippling of the molten surface of the weld pool. Furthermore, the gas must be distributed over the full area of the weld pool until it is cool enough not to react with the atmosphere[37].

2.4 LASER WELDABILITY OF MATERIALS

Dawes[37] has reviewed many of the common materials and their suitability for laser welding. For pure metals with a reasonable absorption coefficient at the laser wavelength, this requires the two metals within the joint to have overlapping liquid temperature ranges. They must also be mutually soluble. The introduction of alloying

elements and their reaction to rapid heating and cooling can have a substantial effect on the structure of the weld. Some steels and most aluminium alloys suffer microstructural damage during laser welding[38-42].

Dawes has presented a summary of the mechanical properties of laser welds made in a variety of structural steels. Individual alloying elements contribute to the weldability of steels. Oxygen, for instance, is a source of porosity and occasionally cracks[43]. "Killed" steels in which the oxygen content has been reduced are therefore preferred for laser welding. The carbon content of a steel has a major effect on the weld quality. As a general rule, low-carbon steels tend to weld reliably[44, 45]. Fast cooling rates result in transformation hardening to produce weldments which are considerably harder than the base metal[46]. Although the weldment still exhibits good ductility and toughness, it is susceptible to cold cracking. Nevertheless, steels with carbon contents of up to 0.3% have been successfully welded[7].

Other alloying elements also affect the susceptibility of the weldment to cold cracking. The influence of these alloying elements can be related to a carbon equivalent, C_{eq}, by empirical equations such as that recommended by the International Institute of Welding[47]:

$$C_{eq} = C\% + \frac{Mn\%}{6} + \frac{Cr\% + Mo\% + V\%}{5} + \frac{Ni\% + Cu\%}{15} \qquad (2.1)$$

A carbon equivalent less than 0.4 indicates that the steel is weldable. Sulphur and phosphorus are also present in the steel. Combined levels in excess of 0.04% often cause solidification cracking. Solidification cracking occurs at high temperatures under circumstances where the material has a low ductility and is subjected to high contractual stresses. It is common in materials containing compounds which have widely differing melting temperatures. In steel the main elements which contribute to solidification cracking are high levels of carbon, sulphur, phosphorus and boron.

Austenitic stainless steels are ideally suited to laser welding because the rapid heating and cooling rates do not allow precipitation of Cr-rich carbides to occur at grain

boundaries. These carbides tend to reduce the corrosion resistance of the steel[48]. In addition, these steels have a much lower thermal conductivity than carbon steels and a higher absorptivity, so higher penetration depths can be achieved in austenitic stainless steels than in carbon steels. Ferritic stainless steels, which usually have lower Cr and Ni concentrations than austenitic stainless steels, also weld reliably. Martensitic stainless steels understandably produce very hard and brittle weldments. As conventional pre-heating and tempering sometimes alleviate this problem, this is one specific area which may benefit from the use of tandem laser radiation.

Aluminium and aluminium alloys are difficult to laser weld because of their high thermal conductivity and low absorptivity at laser radiation of both l0.6-μm and l.06-μm wavelength. These materials suffer many weld defects including porosity, cracking, blowholes and a loss of alloying elements. Tosto *et al.*[39] have examined aluminium alloy welding and concluded that sandblasting or pickling did improve the absorption of laser radiation. They discovered that nitrogen was the best shielding gas and that a slight defocussing of the laser produced the best welding results. Several researchers[41, 49, 50] have looked at these problems experimentally. Yamaoka *et al.*[40] found that hot cracking could be reduced in A6063 Al alloy by adding filler wires (A4047) to the weld. Porosity in these welds appears to be caused by high concentrations of hydrogen. Automotive companies are studying the compatibility of A5000 and A6000 series aluminium alloys with laser welding[51-54]. Alloys A5251 and A6061 have been successfully welded using 5 kW CO_2 lasers, and recently a 3 kW Nd:YAG laser was successfully used to weld A8000 series Al alloys[55].

Finally, surface coatings are often used to provide corrosion resistance to steels, and are common in the automotive, agricultural and appliance industries. Welding steels which have been electro-plated or hot-dip galvanised with a zinc-based coating presents some problems[56]. Due to the rapid heating and cooling cycles, zinc vapour can become trapped in the weldment, causing porosity. Butt configurations usually do not present a problem as zinc vapour is allowed to escape above and below the weld. On the other hand, lap configurations do not allow zinc vapour to escape easily, and can be susceptible to high degrees of porosity. High-power lasers can produce enough heat

ahead of the weld pool to boil off some volatile coatings. However, low-power lasers and pulsed lasers do not have this ability. Using a tandem laser arrangement may enable such lasers to successfully weld these materials. This type of arrangement would also allow the more efficient use of high-power lasers. A number of industries would benefit from such improvements, including the automotive industry[57-66].

2.5 MODELS OF CONTINUOUS AND PULSED LASER WELDING

2.5.1 Development of a model

The development of a laser welding model is usually divided into the following main stages:

- selection of model type
- scope of model
- construction of model
- solution of model equations
- validation of model
- implementation of model.

The two basic types of model are the approximate numerical model and the closed-form analytical model, although hybrid numerical-analytical models are possible. For example, it may be necessary to determine the thermal history of a material which has been butt welded with a continuous laser source of intensity 2 kW, moving at a speed of 1000 mm/min. Alternatively, the problem might be one of determining the thermal history in a bead-on-plate weld which has resulted from a moving laser heat source pulsing at 20 Hz, with each pulse lasting just 3 ms. Without too much effort, the governing equations, boundary conditions and initial conditions of these problems can be formulated. However the difficulty in these two examples lies in the fact that several complex mechanisms of heat transfer are present. Owing to the wide range of temperatures involved, the temperature dependence of the numerous thermophysical properties also complicates the respective analyses. This complexity is increased further

by the presence of a moving solid-liquid interface whose position is not known *a priori* and must be determined as part of the solution. Hence analytical solutions to these types of problems are difficult to obtain.

One possible alternative is to make simplifying assumptions, to ignore the difficulties and reduce the problem to one that can be handled. Sometimes this procedure works. However, more often than not, it leads to serious inaccuracies or simply incorrect results. With the evolution of high-speed digital computers and software codes, a more viable alternative is to retain the complexities of the problem and find an approximate numerical solution.

Numerical techniques can be employed to predict the transient development of the weld pool. The structure of the model allows each phenomenon to be addressed individually, thereby gaining a greater insight into the competing interactions. The temperature dependence of the thermophysical properties and the movement of the solid-liquid interface can be considered without difficulty. There has therefore been considerable interest in the use of numerical models to obtain time-dependent solutions of these processes.

The most commonly used numerical method is the finite element model. A system with an infinite number of unknowns (the response at every location in the system) is transformed into one with a finite number of unknowns, related to each other by elements of finite size. These elements connect at their nodes to form a mesh which simulates the geometrical form required. A piecewise approximation of the governing equations is then performed. The basic premise of this method is that a system can be approximated by replacing it with an assemblage of discrete elements. Since these elements can be organised in a variety of ways, they can be used to represent exceedingly complex shapes. An example of a three-dimensional mesh which can be implemented to model continuous or pulsed laser welding is shown in Figure 2.2. This example shows how a fine mesh is employed in the area of laser beam irradiance, where high temperature gradients are expected, grading to a coarser mesh away from this zone. Symmetry about the weld centre-line is assumed, so only half the workpiece need be modelled.

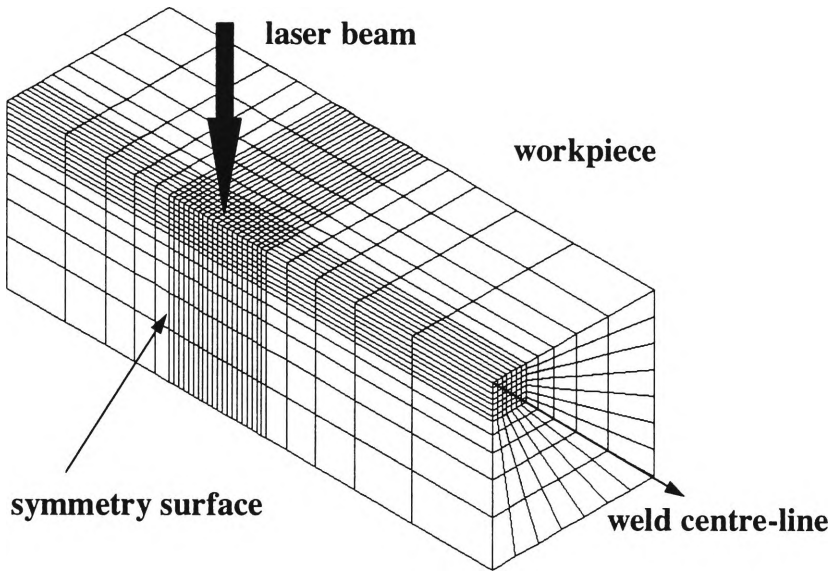

Figure 2.2 Finite element mesh for continuous or pulsed laser welding.

Other numerical techniques are the finite difference method and the boundary integral method. The former technique gives a pointwise approximation to the governing equations. The model is formed by writing difference equations for an array of grid points. The latter technique is based on an integral representation of the governing equations in terms of initial values, boundary values and Green's functions.

Of the three main numerical methods, the finite element method has the best capability for non-linear analysis and dealing with complex geometry[67]. It is the most compatible with integrated CAD/CAM software systems. For thermal analysis alone, a strong argument can be made in favour of the finite difference method. However, for thermo-elasto-plastic analysis the argument is stronger for the finite element method. The boundary integral technique is not well developed for non-linear analysis.

2.5.2 Analytical models of continuous laser welding

Until the mid 1930s, most of the work on heat flow assumed an essentially exploratory nature, which helped in the understanding of basic controlling variables relating to conventional welding techniques, process parameters and the geometry of the workpiece. In 1946, Rosenthal[68] developed the first analytical solutions of heat flow in one, two and three dimensions. Point, line and plane heat sources were considered. Consequently, the analysis was subject to serious error for temperatures close to the heat source. Away from the heat source, however, a good correlation between experiment and theory was evident. This region can be identified as that portion of the material undergoing heating and cooling cycles by conduction only. The limitation of the analytical solutions in the close proximity of the heat source may be attributed to the simplifying assumptions of the heat source and the temperature-independent thermophysical properties. Attempts to incorporate more realistic terms in Rosenthal's solutions could only provide limited success in the vicinity of the heat source.

Rosenthal's solutions represent the starting point of analytical solutions applied to welding techniques in general. It was not until 1973, eight years after the invention of the first carbon dioxide laser, that Swift-Hook and Gick[25] developed the first heat

transfer model for continuous laser welding. In a similar manner to Rosenthal, the laser beam was modelled as a moving line source. It was assumed that the melting temperature isotherm determined the location and shape of the fusion zone. The width and depth of the fusion zone were then related to the laser power and velocity of the workpiece. Since the formation of a keyhole was neglected, their model produces only partial agreement with experimental results and applies mainly to conduction laser welding. Convective flow in the weld pool was not considered.

In 1976, Klemens[69] produced a more sophisticated model of the continuous laser welding process. The model assumes a plasma-filled keyhole which is held open by a balance between vapour pressure within the keyhole, surface tension and hydrodynamic pressure in the molten region surrounding the keyhole. The model provides a more refined picture of the influence of heat flow, vapour flow, surface tension and gravity on the keyhole and shape of the fusion zone.

Up to that point all models of conduction and keyhole laser welding were mainly confined to conduction within the workpiece. Convective flow in the weld pool was not examined in any great detail. Modelling of the fluid flow around the keyhole has only occurred in the last few years. This is important because the mixing of the metal during welding provides the homogeneity of the weld bead. Theories can provide an estimate of the amount of energy needed to drive such fluid flows (and hence its effect on the welding speed), as well as the vertical cross-section of the keyhole (and therefore the penetration depth).

This aspect was extensively investigated in 1976 by Andrews and Atthey[70], who considered fluid flow in a molten pool resulting from a stationary laser beam. Convective flow in the weld pool is three-dimensional. Three distinct driving forces for weld pool convection exist, namely the buoyancy force, the Marangoni force and the plasma force. The buoyancy force is caused by temperature and concentration gradients within the weld pool. These gradients induce flow. The cooler, more dense material sinks under the influence of gravity, forcing the hotter, less dense material to rise. The Marangoni force also arises from temperature and concentration gradients in the weld

pool. The plasma force, however, results from the pressure gradient in the weld pool. The laser power density required for plasma formation is in the order of 10^{10} W m^{-2}, although this number depends on both the wavelength of the laser and the thermophysical properties of the workpiece[23].

The hydrodynamic model of Andrews and Atthey incorporates only the effects of gravity and surface tension. The underlying assumptions are that the vapour pressure inside the keyhole is taken to be equal to the atmospheric pressure and 100% of the incident power is absorbed at the surface of the workpiece. In practice, the former assumption is only valid for shallow keyholes, whereas the latter simplification is unjustified. Absorptivity is a function of a number of variables such as the nature of the surface, the level of oxidation, surface temperature, power density of the beam, and the amount of plasma present. The assumption of a constant value is unlikely to be realistic. Nevertheless, this pioneering model provides a valuable insight into the development of the keyhole during continuous laser welding.

In 1977 Cline and Anthony[71] integrated the point source over the workpiece surface to yield a Gaussian power distribution. This assumption eliminated singularities in the temperature calculations and showed that spot size has a strong influence on the maximum temperature attained by the workpiece. The model assumes 100% absorption and calculates an exponential decrease of the temperature in the vertical direction. Conduction and keyhole welding conditions were both considered, whereas weld pool convection was not included in the model.

In 1986, Davis *et al.*[72] examined convective flow. Their model starts with the basic assumption that the Peclet number, which is the ratio of convected to conducted heat, is small. It also assumes that the variation in the size of the keyhole with distance parallel to the beam has a negligible effect on the flow around the hole. Hence the convective flow is essentially two-dimensional. Weld pool convection is modelled by solving the Navier-Stokes equations of motion.

This approach is a highly complex and time-consuming exercise. A simple approach is to compensate for the weld pool convective heat transfer with an artificially high thermal conductivity for the material in the weld pool. Typically, a thermal conductivity of as much as 10 times its actual value at the solidus temperature has been used in conventional welding models[73]. The difficulty associated with this technique is that various values of conductivity for the molten material must be trialled until a reasonable weld pool shape is obtained. Anisotropic conductivities can also be used for this purpose. Although this technique has been employed in conduction models of conventional welding processes, it has not been explored in the context of laser welding models. Other significant modelling efforts are presented in the references[74-80].

2.5.3 Numerical models of continuous laser welding

The complexity of the heat source distribution and the non-linearities associated with temperature-dependent thermophysical properties make it impossible to obtain closed-form analytical solutions with a high degree of reliability in areas close to or within the weld zone. Although numerical modelling offers solutions to these problems, a knowledge of selected thermophysical properties for the range of temperatures of interest is still required. Detailed information on thermophysical properties is difficult to obtain, since there is currently limited experimental data for the properties of most materials at high temperatures. Consequently, most numerical modelling efforts have used constant or assumed values for selected thermophysical properties.

Mazumder and Steen[81] developed the first numerical model of the continuous laser welding process. This model implements the finite difference technique for a Gaussian intensity distribution and starts with the assumption that the absorptivity of the incident radiation below the boiling point is 20%. Convective flow in the weld pool and the temperature dependence of the thermophysical properties are not considered, however the non-linearities of convection and radiation to surroundings are included in the model. The absorptivity of the laser radiation is considered to be 100% when the temperature exceeds the boiling point. As a result, matrix points remain in the conducting network at fictitiously high temperatures to simulate the convection and

radiation heat transfer mechanisms within the plasma. Attenuation of the laser radiation within the keyhole is described by Beer-Lambert's law, namely $P = P'\exp(-\alpha L)$, where α is the attenuation coefficient and is considered to be independent of position within the keyhole. P is the beam power at depth L and P' is the power of the beam at the workpiece surface. The model can be used to predict temperature distributions, the size and shape of fusion and heat-affected zones, maximum welding speeds and the effect of workpiece thickness. The model therefore provides a good physical insight into some of the process mechanisms.

In 1984, Chan *et al.*[82] developed a two-dimensional finite difference model for convective heat flow by solving the Navier-Stokes equations. The main finding was that the recirculating velocity near the surface is as much as two orders of magnitude higher than the velocity of the heat source. This means that the weld pool might rotate as many as five times before solidifying. However, in the case of pulsed laser welding, the very short pulse durations of typically 1-10 ms, with solidification times in the same range, do not allow sufficient time for the circulation of a short-lived weld pool. The mechanism of weld pool convection is not expected to be a dominant mode of heat transfer. A list of numerical models,, as well as combined numerical/analytical models, which consider similar aspects of the continuous laser welding process, is shown in the references[83-87].

2.5.4 Pulsed laser welding models

During pulsed laser welding, the material is heated intermittently with a succession of short-duration pulses to produce a series of overlapping spot welds. Consequently, the material is subjected to a large number of thermal cycles. Predictions of accurate heating and cooling rates using analytical methods are very difficult to obtain.

Nevertheless, Bechtel[88] developed analytical solutions to the heat conduction equation for the pulsed laser heating of materials. Both surface and volume generation of heat were considered and the results obtained were compared with each other. Comparisons with experimental results were only briefly alluded to. It was found that if the depth of thermal diffusion during the laser pulse is large compared to the optical

attenuation depth, the surface and volume generation models give nearly identical results. However, if the thermal diffusion depth is close to or less than the optical attenuation depth, the two types of model give significantly different results. Specific numerical results are provided for a tungsten target irradiated by pulses of different durations and the implications of the results are discussed with respect to the heating of metals by picosecond laser pulses.

Zacharia *et al.*[89] developed a two-dimensional numerical model employing the finite difference technique. This model describes convective flow and heat transfer in the fusion zone. The four main assumptions of the model are:

(1) the fluid flow and heat transfer in the fusion zone are two-dimensional;
(2) the fluid flow is primarily driven by the surface tension gradient;
(3) the heat source is Gaussian; and
(4) vaporisation effects are negligible.

This numerical model correlates calculated thermal cycles and cooling rates with features of the solidification structure. Temperature-dependent thermophysical properties are not included in this model. Russo *et al.*[90] only partly considered this added complexity. Their two-dimensional numerical analysis of the pulsed laser welding process assumes surface tension to vary linearly with temperature, while kinematic viscosity is assumed to vary exponentially with temperature.

Further published research on modelling pulsed laser welding is limited. Vishnu *et al.*[91] developed a three-dimensional solution for the temperature distribution due to an instantaneous, stationary Gaussian heat source. This solution was then extended to consider a single moving heat source and finally a series of heat pulses. These theoretical calculations were compared with empirical results for gas-tungsten arc welds. However it is possible that this model could be modified to describe pulsed laser welding.

Gellert and Egli[92] developed a basic one-dimensional model which describes the melting of copper by a pulsed heat source. A one-dimensional model of pulsed laser

heating of optical surfaces was constructed by Jette and Benson[93], while Arutyunyan *et al.*[94] developed a general hydrodynamic model of the interaction of pulsed radiation with matter.

2.5.5 Improved modelling methods

The complexity of the task of modelling a system with so many interacting phases has prevented the widespread application of predictions based on the models, such as penetration depth, weld speed, weld strength and homogeneity for any given material. Although there is scope for improvement, such theoretical achievements have been extremely useful in understanding the physical processes involved and in determining which of the processes will have a dominant effect on the weld.

The models discussed above have all assumed a certain power distribution of the laser beam. Typical assumptions include line or Gaussian profiles. The true shape of the beam profile, however, may not warrant these assumptions (Figure 2.3)[95]. As weld size and shape are strongly dependent on the distribution of the heat source, it is essential to incorporate an accurate description of the heat source. For this reason, commercial beam analysers can be used for measuring beam profiles. The output data can be used as the direct input for the numerical program used to model the laser welding process.

This is one method which can be employed to improve the accuracy of the numerical approach. Other methods include the following:

- Minimisation of the mesh size near the heat source. Although this improves solution accuracy and numerical stability, the solution process is computationally demanding.

- Implementation of finite element codes such as ANSYS, ABAQUS or NASTRAN to develop adaptive meshing and remeshing schemes.

- The development of more hybrid analytical/numerical models. For example, fast analytical methods can be employed to determine boundary conditions on a restricted

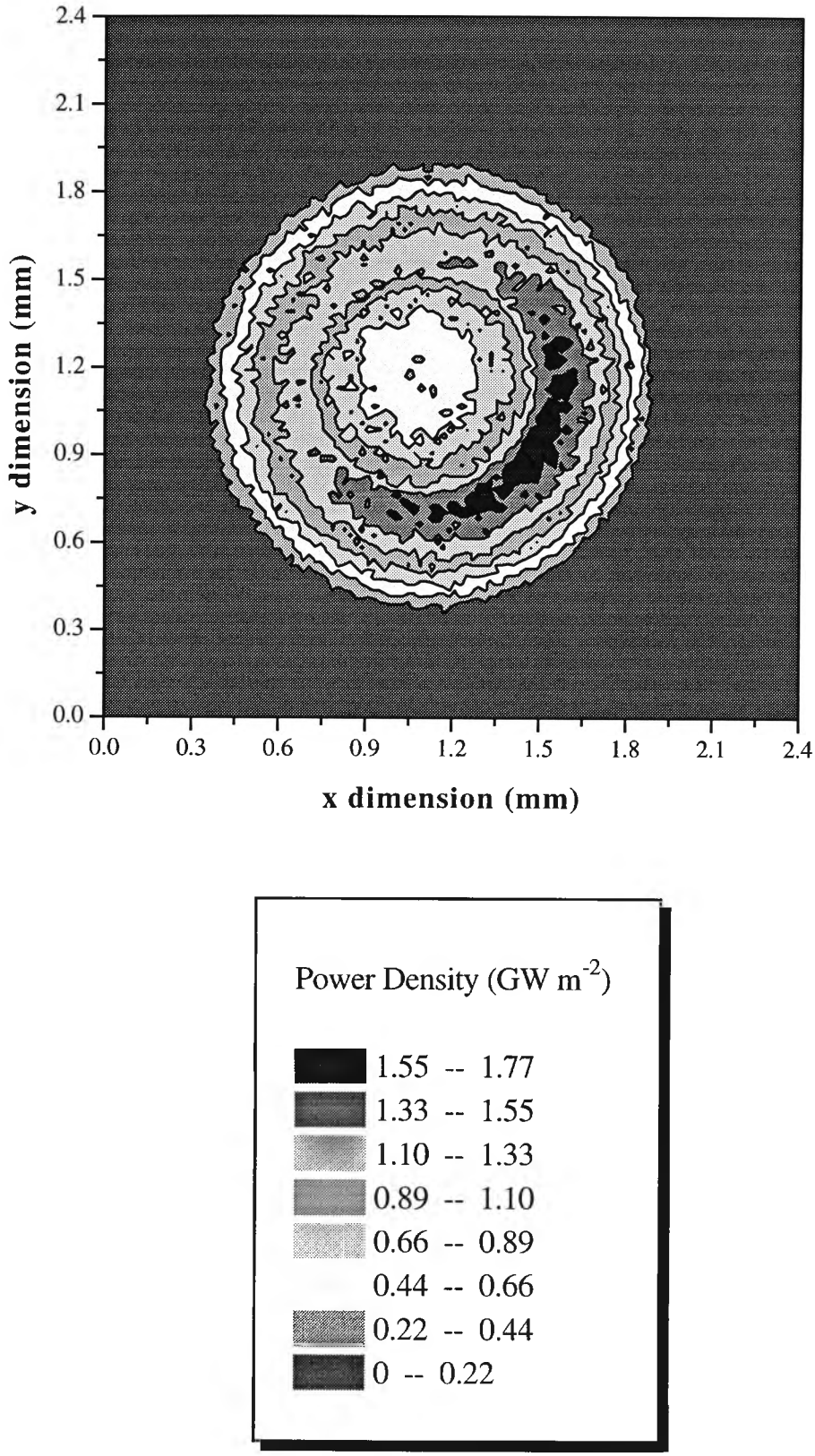

Figure 2.3 Crescent-shaped beam profile of a pulsed Nd:YAG laser. Laser conditions: 7 J, 3 ms, focus - 5 mm.

domain surrounding the heat source. Numerical solutions within this domain can then be performed by applying these boundary conditions.

Although the development of PCs, mainframe computers and software packages has improved the efficiency and applicability of numerical methods, a trade-off still exists between computational accuracy and solution time. This balance is critical in the construction phase of a laser welding model.

2.6 TANDEM-BEAM RESEARCH

2.6.1 Tandem-beam experiments

The use of two laser beams in tandem allows the possibility of modifying the laser-material interaction process. The lead beam could be used to pre-heat the material to a near-molten state where its absorption characteristics are significantly different to those of the unheated material[22, 96]. The present experiments have determined if the penetration depth is affected by this advance beam.

The idea of using twin heat sources in welding is not new. Steen[97] proposed a technique called arc augmented laser processing, where an electric arc was used to assist a laser in the welding and cutting of materials. It was found that the arc root contracted to about the size of the focus of the laser beam on the surface of the material and thus large amounts of energy could be channelled to this small point from the less expensive energy source of a TIG or MIG arc. This effectively simulated the action of a much larger laser source than was used. This technique, although revisited by other researchers[98, 99], has not become an industrial reality.

More recently there has been much interest in shaping laser beams for specific purposes such as improved welding and cutting, welding of dissimilar materials[100], and cladding[101]. Brief articles have alluded to various collaborative research efforts in this area, but no details have been published[102, 103].

Very few papers have been published on the use of two laser beams for materials processing. Aruga *et al.*[38] have used a cw Nd:YAG laser beam to pre-heat samples of aluminium alloys prior to a following pulsed Nd:YAG laser beam. These experiments showed the feasibility of using two laser sources to weld otherwise difficult-to-weld aluminium alloys of interest to the automotive industry. No physical explanation was offered as to why this tandem laser experiment produced satisfactory welds. Banas[104] commented on the use of splitting a very high power CO_2 laser beam (14 kW) into two beams of equal intensity, either parallel or perpendicular to the direction of welding. This reduced the possibility of "humping", a weld metal instability, by effectively reducing the power density of the welding beam and delivering the energy in two beams of half the peak intensity. Glumann *et al.*[105] proposed combining two separate CO_2 laser beams to achieve a higher energy input, but did not look at the influence of combined beam shape on the characteristics of the weld. Williams *et al.*[30] showed that a pulsed excimer laser could be used to ablate the galvanised coating from mild steel prior to welding with a Nd:YAG laser or a CO_2 laser. The removal of the coating was clearly demonstrated, although this method was designed only to pre-treat coated materials; it was not a simultaneous tandem process and would be far too slow for any medium- to large-scale production work.

2.6.2 Tandem-beam models

Kannatey-Asibu et *al.*[106-108] have published several papers describing a mathematical model of the thermal history of a sheet of steel subjected to a continuous dual heat source. Initially, two point sources of heat travelling in a straight line were analysed. For the material being heated, the temperature can be described by the equation:

$$\frac{\partial T}{\partial t} - v\frac{\partial T}{\partial x} - \alpha\nabla^2 T - \frac{q}{\rho c} = 0, \qquad (2.2)$$

where:

T = temperature (K),

t = time (s),

v = welding speed (m s^{-1}),

q = heat input per unit time per unit volume (W m^{-3}),

α = thermal diffusivity (m^2 s^{-1}),

ρ = density (kg m^{-3}),

c = specific heat (J kg^{-1} K^{-1}).

If constant thermophysical properties are assumed, this equation takes a linear form. It was solved for each source independently and the solutions were then superimposed. As expected, Kannatey-Asibu *et al.* found a difference in the cooling rates of the material when single- and dual-beam irradiation were used. The introduction of the second heat source results in a reduction in the cooling rate. Furthermore, the greater the welding velocity, the greater the difference in the cooling rates between single- and dual-beam irradiation. It was also found that the rate at which heat is input to the material has a more complex effect; the net result of which is that at higher heat inputs the difference between single and dual heat sources is more evident. Conversely, for high thermal conductivities, the difference between single- and dual-source irradiation is decreased. This means that the split-beam laser welding system is more effective at lowering the cooling rate for materials with low conductivity rather than high conductivity.

In a more recent paper Liu and Kannatey-Asibu[108] analysed the more realistic arrangement where the "minor" pre-heating source is a defocussed Gaussian beam, and the trailing, major heat source is assumed to be a line source for deep penetration or keyhole welding. This paper gives a much more detailed analysis of the problem, including analysis of the penetration of the two types of sources, the influence of the Gaussian distribution of the pre-heating source, cooling rates, inter-beam distances, weld pool sizes and peak temperature calculations. For larger Gaussian beams, the peak temperature is lower and the weld bead larger. Under typical conditions, cooling rates could be reduced from about 1000 K s^{-1} in the case of a single irradiating source, to less than 600 K s^{-1} using dual laser irradiation. As indicated in previous papers, for the same power of the major heat source a higher-power pre-heating source results in a lower cooling rate, for a given temperature; and the higher the temperature, the larger the

difference. Finally, it was determined that both the weld pool size and the cooling rate increase as the inter-beam spacing is decreased.

The work of Liu and Kannatey-Asibu must be considered with reference to their assumptions. Their model makes use of Beer-Lambert's law with an assumed beam power attenuation coefficient determined by Mazumder and Steen[81]. This attenuation coefficient has an approximate value of 800 m^{-1} for low-carbon steel and only applies to attenuation within the plasma-filled keyhole. It does not apply to the attenuation of laser radiation once the radiation is within the solid material, as is assumed in their model. In reality, the attenuation coefficient for solid low-carbon steel is likely to approach infinity[88]. An alternative method of formulating the problem of laser heating would be to consider that the laser energy is absorbed at the surface of the solid, rather than being attenuated within the volume of the solid. This alternative approach has been adopted in the present study.

These analytical simulations have served as a useful guide to the analytical modelling which was performed in the present study. Pulsed laser sources were modelled, rather than the continuous heat sources used in the above work, adding another level of complexity to the problem. The analysis was taken an important step further by measuring the energy distribution across the laser beam for different energies and focal positions. These "beam profiles", along with the temperature dependence of the thermophysical properties, were incorporated into the numerical model of the process. The numerical model was then calibrated with experimental measurements of fusion and heat-affected zone dimensions. The results were compared with analytical predictions, as well as direct measurements of the surface temperature of the material. This was performed using a fast optical pyrometer.

The requirements of such a system are demanding and must be capable of measuring surface temperatures in the range 20 °C to 1500 °C, within an area less than 1 mm^2 at a rate of at least 10 kHz. The pyrometer should also be able to measure cooling rates transverse to the weld centre-line as high as 10^5 to 10^6 K s^{-1}, as is the case during

pulsed laser welding. A commercial instrument was purchased for these measurements, as it was the only product found capable of meeting the demands of the experiments.

2.7 WELD METALLURGY

Although pulsed laser welding is associated with very rapid thermal cycling, the weld metallurgy and its relationship to cooling times exhibit some characteristics of conventional welding processes, as well as structures characteristic of rapid cooling rates. Literature on conventional weld metallurgy does provide some understanding of the structures and physical chemistry of the welds, but more relevant is the literature dedicated to those aspects of weld metallurgy arising from continuous cooling transformation (CCT) diagrams[109], where there is an attempt to describe weld metal microstructures as a result of an interactive process of continuous cooling, rather than the standard phase equilibrium diagrams. Rapid solidification theory, which encompasses the high cooling rates experienced in laser welds, is also relevant. Below is a brief review of relevant aspects of this work.

There is currently a wealth of information on laser weld macrostructures and associated weld defects. This information is normally presented at any major laser applications conference[110]. The problem of HAZ cracking during laser welding, which often originates from steels with too high a carbon content, has been investigated by many authors[44-46, 111-113]. However, correlations between laser welding parameters and microstructural features are less abundant. Both Vitek *et al.*[114] and Zacharia *et al.*[89] have published excellent descriptions of solidification structures in austenitic stainless steels. These authors showed that the high solidification rates associated with laser welding produce significantly different microstructures to those found after conventional welding. Rapid solidification therefore provides one means by which the normal solidification structure can be altered. The formation of high-temperature structures can be suppressed due to the presence of highly non-equilibrium conditions, leading to a variety of new structures and metastable phases. The present study has linked model predictions of the temperature distribution in and around a laser weld with the formation of certain solidification microstructures.

The metallurgy of conventionally produced welds, such as TIG and MIG welds, has been studied extensively by authors such as Savage *et al.*[115], Lancaster[116] and Jones[117]. This work does have some relevance to the present study. However, the cooling rates involved in laser welding can be as high as 10^6 K s^{-1}, far in excess of even the scope of CCT diagrams and similar techniques used to describe "faster" cooling rates encountered in arc welding, typically 10^0 to 10^3 K s^{-1} [118, 119].

An excellent description of the capabilities and limitations of CCT diagrams for steels has been published by Harrison and Farrar[118]. Three basic zones in a weld cross-section are considered: grain-refined heat-affected zone (HAZ), grain-coarsened HAZ and the weld metal itself. Unfortunately, because of the wide range of peak temperatures experienced by different parts of the metal during welding, an almost infinite number of CCT diagrams would be required to describe the transformation behaviour at every point in the steel. However, general features of the three major regions can be identified and correlated with well-known descriptive terms of the phases and morphology of metals. The effects of different compositions on CCT diagrams are also discussed and can be used as a starting point in the analysis of laser-welded materials.

In the case of laser welding, and the subsequent rapid cooling fronts associated with weld metal solidification, it is beneficial to review literature pertaining to rapid solidification. A detailed account of this phenomenon has been provided by Savage *et al.*[115], who noted that during the usual solidification process the transformation of a liquid phase to a solid normally occurs by a process of nucleation and growth. In fusion welding processes the nucleation process is not evident since a solid-liquid interface is always present and epitaxial growth may occur from the unmelted base metal. It is also pointed out that segregation always occurs on solidification of weld metals, as they are never pure. Savage *et al.* proposed a schematic representation of the influence of growth rate and temperature gradient on the pattern of solidification, depending on the percentage of solute present in the alloy. The distribution patterns of the solute for cellular and dendritic growth patterns were described and experimental demonstrations of these proposed mechanisms were presented. Cross-sections presented by Coyle[120] have shown that in pulsed laser welds, a cellular-dendritic microstructure exists, the relative ratio of dendrite to cellular growth depending on the position in the weld. This

is understandable because as the weld metal solidifies, either from the edge of a continuous seam or from the circumference of a laser spot weld inwards, the temperature gradient tends to decrease in this direction, resulting in a transition to a dendritic growth mode in the weld centre.

Several authors have looked at the calculation of cooling times for weldments. For conventional welding, Degenkolbe *et al.*[121] have characterised weld thermal cycle times by the time taken for the material to cool from 800 °C to 500 °C, $t_{8/5}$. This approach is generalised to various joint designs by semi-empirical "efficiency" and "weld" factors, which can lead to general relationships between weld properties such as yield strength, tensile strength, hardness and the cooling time. While this type of work is valuable in establishing links between welding conditions and the consequent properties of welds, it must be remembered that the cooling times involved in laser welding are much shorter and weld properties will change accordingly.

The general field of the rapid solidification of metals and alloys has been reviewed by Jones[117]. This is not as mature an area of research as conventional welding solidification, but the cooling times involved are comparable with those encountered in laser welding. Consequently, the relationships established between solidification fronts, cooling rates and weld properties are much closer to those in the present laser welding study.

Rapid solidification can lead to large departures from the equilibrium constitution of the material being processed, resulting in extensions in the solid solubility and the formation of non-equilibrium crystalline phases. Jones has calculated the cooling rate for a slab, cylinder and sphere of molten material as the melt front progresses towards the centre of the melt. The heat flow considerations for these geometries dictate that there is a limiting thickness for achieving a given rate of cooling, e.g. 10 mm for 10^2 K s^{-1}, 0.1 mm for 10^6 K s^{-1}, and 1 μm for 10^{10} K s^{-1}. Moreover, this limiting thickness is the threshold value of distance below which the cooling rate and the velocity of the cooling front are controlled by the magnitude of the heat transfer coefficient. In many techniques for producing rapidly solidified materials, such as in the production of glassy metals by melt

spinning or spray methods, this heat transfer coefficient can be quite small, because of a limited contact time with the cooling surface, or the quenching of liquid droplets by gas blasts, etc.

In laser welding, physical contact between the melt and the chill surface is effectively perfect. However, it must be borne in mind that different parts of the weld will have very different cooling rates, the highest being near the HAZ where energy is transferred rapidly to the surrounding solid material, and lowest on the weld centre-line where cooling rates, as discovered in this project, are controlled by the shape and size of the laser beam.

2.8 CONCLUSIONS

The published literature relevant to the present experimental and theoretical study of pulsed laser welding has been reviewed. As the use of two laser beams is new, there is very little literature which has directly addressed the problems associated with the present research. However, this study encompasses a wide range of research fields, including laser technology, laser welding characteristics, laser-materials interaction, the weldability of materials, mathematical modelling of heat transfer associated with asymmetric, time-varying sources, and rapid solidification theory. This study will contribute to the understanding of the laser welding process. It offers the potential to achieve higher weld quality in laser-weldable materials, and to allow the laser welding of presently difficult-to-weld materials.

CHAPTER 3

MATERIALS, EXPERIMENTAL DESIGN AND TECHNIQUES

3.1 INTRODUCTION

The laser system employed to generate the experimental results in this study was a LASAG KLS522 pulsed Nd:YAG laser equipped with one 5-m fibre-optic cable, one 10-m fibre-optic cable and two LL-BK1 processing heads. The maximum average output of the laser was 500 W. Each processing head incorporated standard two-element optics to refocus the beam emerging from each optical fibre. Small amounts of spherical aberration inherent in each design gave rise to different intensity distributions as a function of focal position. The measurement and subsequent modification of these intensity distributions for the modelling work are discussed in sections 3.3.1 and 3.3.2, respectively. Argon shielding gas was used for all experiments.

During tandem-beam pulsed laser welding, two laser beams intermittently interact in tandem with the workpiece over very short time intervals. This results in very rapid heating and cooling cycles. The weld bead is the product of a number of overlapping spot welds, and every point in the weld area experiences a complex series of thermal cycles during the passage of each laser beam. In order to understand and subsequently exploit this very complex process, it was necessary to start with the relatively simple experiment of the effect of a single pulse of energy delivered into AISI 1006 steel. The experiment was extended by considering a series of overlapping spot welds. A second beam was then introduced into the analysis and the same procedures were repeated for tandem laser beam irradiation. The additional variable of inter-beam distance in the tandem case also required a study of the influence of inter-beam distance on the observed microstructures.

The numerical and analytical models of single- and tandem-beam pulsed laser welding were assessed by comparing the predictions of weld bead dimensions with the results of these experiments. AISI 1006 steel of thickness 0.9 mm was used in all cases. The numerical model was used for both keyhole and conduction-limited welds, whereas the analytical model was employed for just conduction-limited welds. Chapter 5 provides descriptions of each model. In order to test the capabilities of the models for a different material, A5005 aluminium alloy was chosen to perform comparisons between experiment and theory for a select set of conditions.

A more direct check of the theoretical work, apart from the measurement of weld bead dimensions and the consequent estimations of temperature contours, is the comparison of model predictions with actual measurements of temperature as a function of time during laser welding. These measurements have already been performed by Scott *et al.*[122], who recorded the temperature of various points on both the top and bottom surfaces of AISI 1006 steel during single-beam laser welding. A Compotherm BP100E fast optical pyrometer was employed for this purpose. This instrument was able to measure (or sample) the temperature of a point on the workpiece within 36 μs, and so repeated fast measurements of any given point on the surface of the workpiece yielded the thermal history of that point. This temperature-time dependence was directly compared with the appropriate output from the finite element model.

Once the effects of single- and tandem-beam irradiation were understood, the potential advantages of tandem laser beam welding were exploited by considering two different types of coated steel. A detailed description of these materials, as well as a list of the experiments performed, is provided in sections 3.2 and 3.3, respectively. The various weld assessment techniques are then presented in section 3.4, namely, optical and electron microscopy, energy dispersive spectroscopy, hardness tests, tensile tests and formability tests.

3.2 ORIGIN AND DESCRIPTION OF THE MATERIALS

The four materials employed in the present study were:

(1) 0.9 mm AISI 1006 steel

This 0.06% low-carbon steel was supplied by BHP Sheet and Coil Products in the cold-rolled and spheroidised condition. The steel is ideal for bending, drawing, roll-forming, painting and welding. Its uses include office furniture and shelving. The steel has a guaranteed minimum yield strength of 160 MPa, a minimum tensile strength of 280 MPa, a minimum %elongation of 33% and a maximum hardness of 130 HV 20.

(2) 0.6 mm zinc-coated steel

This cold-rolled and annealed deep-drawing steel has undergone electrodeposition to produce a coating of zinc. The trade name of the zinc-coated steel is "Zincseal" and was supplied by BHP Sheet and Coil Products. The coating weight is 10 g m^{-2}. The base metal is low-carbon steel of content 0.08% C. The steel is suitable for bending, pressing, roll-forming and painting. However, the zinc coating can cause porosity during conventional welding. It has moderate drawing applications and is used in automotive panels. The corrosion resistance is similar to that of unpassivated galvanised coatings. The steel has a guaranteed minimum yield strength of 170 MPa, a minimum tensile strength of 300 MPa, a minimum %elongation of 36% and a maximum hardness of 190 HV 20.

(3) 0.85 mm zinc-aluminium coated steel

This hot-dipped zinc-aluminium coated structural steel has the trade name "Zincalume G550" and was supplied by BHP Sheet and Coil Products. The steel is passivated and has a spangled surface. The base metal is low-carbon steel of content 0.1% C. The weight of the coating is 150 g m^{-2}. It is suitable for roll-forming to a minimum internal radius of 2 mm, but is not suitable for bending, drawing or pressing. Conventional welding techniques result in some strength reduction near the weld. Its uses include roll-formed decking and walling. Zincalume has at least twice the corrosion life of passivated galvanised steel of the same thickness. The coated steel has a guaranteed minimum yield/tensile strength of 550 MPa, with limited ductility (2% min.) and a maximum hardness of 250 HV 20.

(4) 0.8 mm A5005 aluminium alloy

This aluminium alloy was supplied by Comalco and consists of 0.8% magnesium, with aluminium as the balance. The temper designation is H34. According to the Standards for Australian Aluminium Mill Products[123], the H3 designation means that the material has been strain-hardened and then stabilised by a low-temperature heat treatment to slightly lower its strength and increase ductility. The numeral 4 after the H3 designation implies a moderate or "half-hard" degree of strain-hardening.

This type of alloy displays good conventional welding characteristics. Consistent results are obtained after decorative anodising. It is a general-purpose alloy and is mainly used in the building industry. The alloy has a minimum yield strength of 140 MPa, a minimum tensile strength of 180 MPa, a minimum %elongation of 3% and a maximum hardness of 60 HV 5.

3.3 EXPERIMENTAL DESIGN

3.3.1 Experimental measurement of beam profiles

In order to understand the interaction of laser radiation with materials which are being welded, it is important to know the distribution of energy within the laser beam over a range of conditions. It is also necessary to provide input data for the numerical and analytical models of this process.

The experimental arrangement used for measuring the intensity profile of a single laser beam is shown in Figure 3.1. On emerging from the fibre-optic processing head, the laser beam focusses at 92 mm from the exit of the head, corresponding to the nominal focal length of the objective lens. The power density at the focus of this beam, under typical welding conditions, is about 3×10^9 W m^{-2}. The camera (Pulnix, model 745M) used to measure the energy distribution across the beam has a saturation intensity of approximately 3×10^{-3} W m^{-2}. In order to be able to measure the beam therefore, an attenuation of 10^{12} is necessary. To preserve the true beam profile, this attenuation must be linear with respect to the incident power density and free from distortion. Careful selection and placement of attenuating elements ensures that this criterion is met. As Figure 3.1 shows, this was achieved by having the beam first pass through a wedged plate, which reflects a nominal 4% at 45°. The remainder of the beam passes either through the wedge, or is reflected at larger angles off the back surface of the wedge away from the camera. The reflecting surfaces of this wedge are polished to a flatness of less than half the wavelength of the laser in order to minimise distortion of the beam. Further attenuation is achieved using neutral density filters. The attenuators suffer thermal shock damage if used without the wedge.

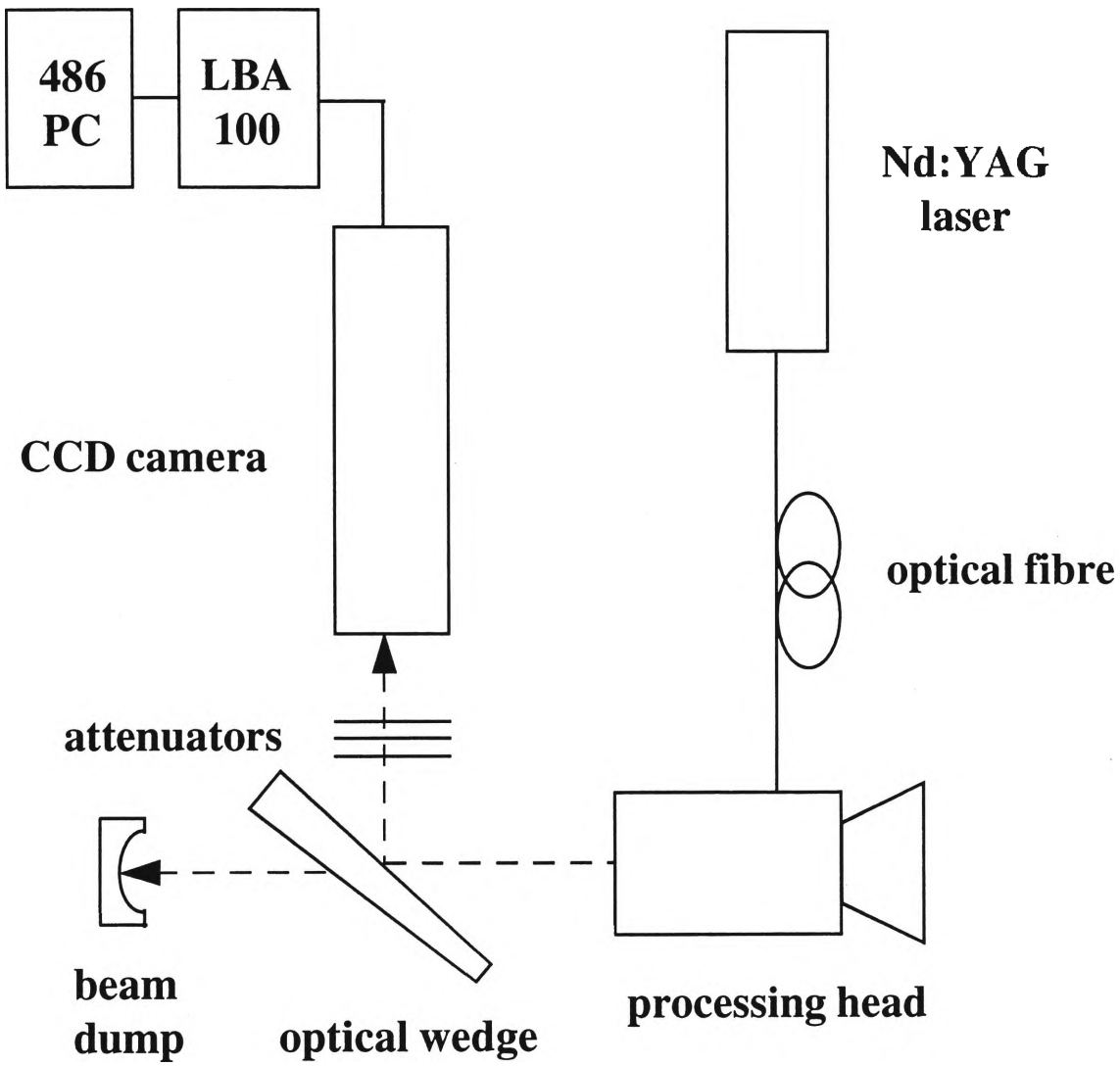

Figure 3.1 Experimental arrangement for beam profile measurements.

The output of the camera was then processed by a commercial beam analyser (Spiricon, model LBA-100) which displays a false-colour image of the intensity of the beam. The binary file data generated by the camera system was then analysed further by converting the files into ASCII format and employing a graphics software package (Origin, version 3.5). The data was used as the direct input for the numerical programs used to model single- and tandem-beam laser welding. As the single- and tandem-beam analytical programs both require Gaussian profiles, a select number of beam profiles were approximated by Gaussian distributions. This approximation technique could not be applied to non-Gaussian intensity distributions. This procedure is discussed in more detail in Chapter 5.

An example of a 3-D beam profile is shown in Figure 3.2. Although this profile is approximately conical in shape, other profiles were found to be top-hat or even donut-shaped, depending on whether the focal position of the laser beam was located above (+ve focus) or below (-ve focus) the surface of the camera. An example of a donut-shaped profile was presented in section 2.5.5. Intensity profiles along the centre-line of selected beam profiles are shown in Figure 3.3.

3.3.2 Modification of beam profiles

The experimental arrangement described here only measures the intensity profile in the plane normal to the direction of propagation of the laser beam. Laser welding with fibre optics is often performed at an angle of 10°-15° to prevent back-reflections from the workpiece damaging the delivery optics. This is particularly so when welding highly reflective materials such as aluminium and copper. Consequently, data from the beam analysing system must be modified to account for this angle, before it is used as input for the models. In the case of tandem fibre-optic laser welding, the second beam is at an angle of incidence even greater than the first. Furthermore, it is undesirable to process with two beams, one 15° to one side of normal incidence, the other 15° to the other side, as this may lead to back-reflections of one fibre-optic system destroying the other. Given the physical construction of the active element in the camera, it is very difficult to measure beam profiles at the angles which are necessary for tandem-beam processing.

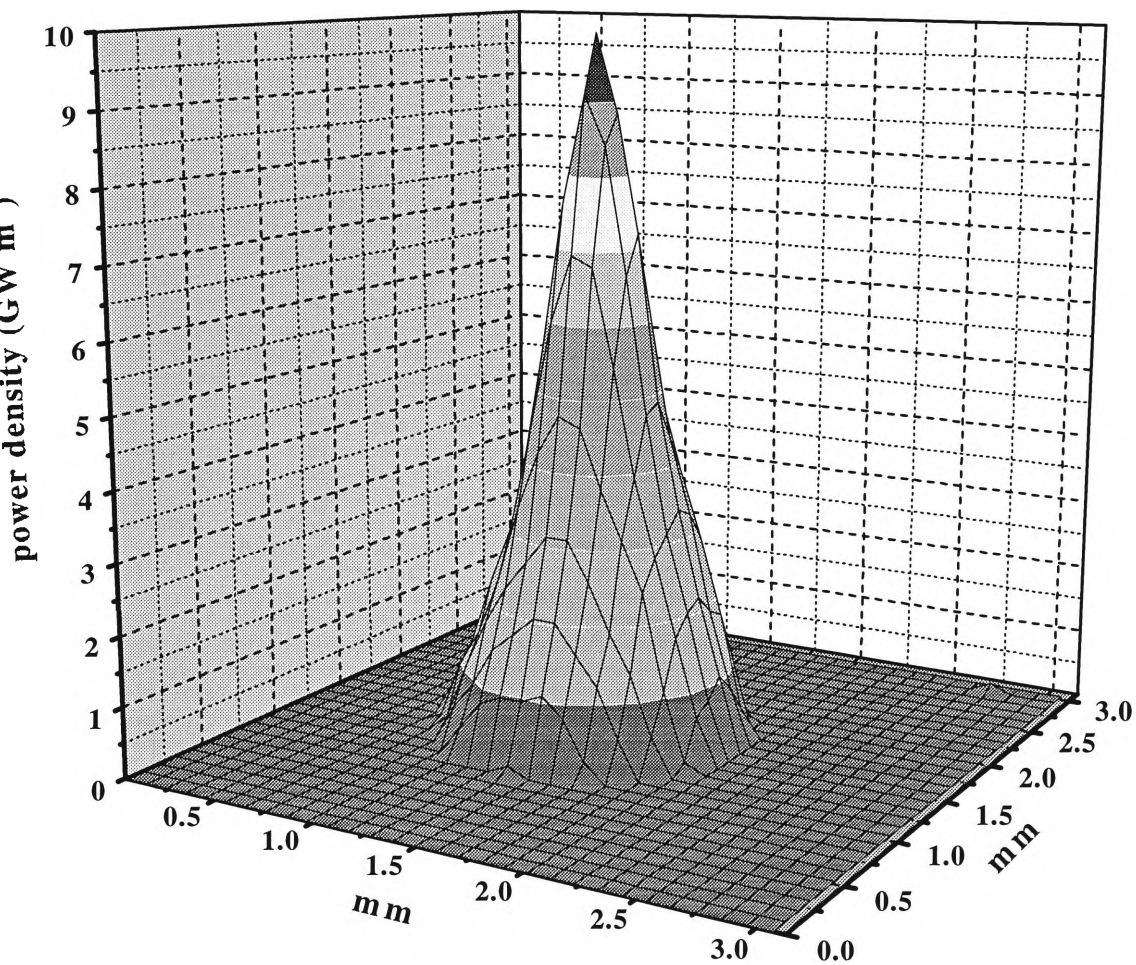

Figure 3.2 Intensity profile of Nd:YAG laser beam.
Laser conditions: 7 J, 3 ms, focus 0 mm.

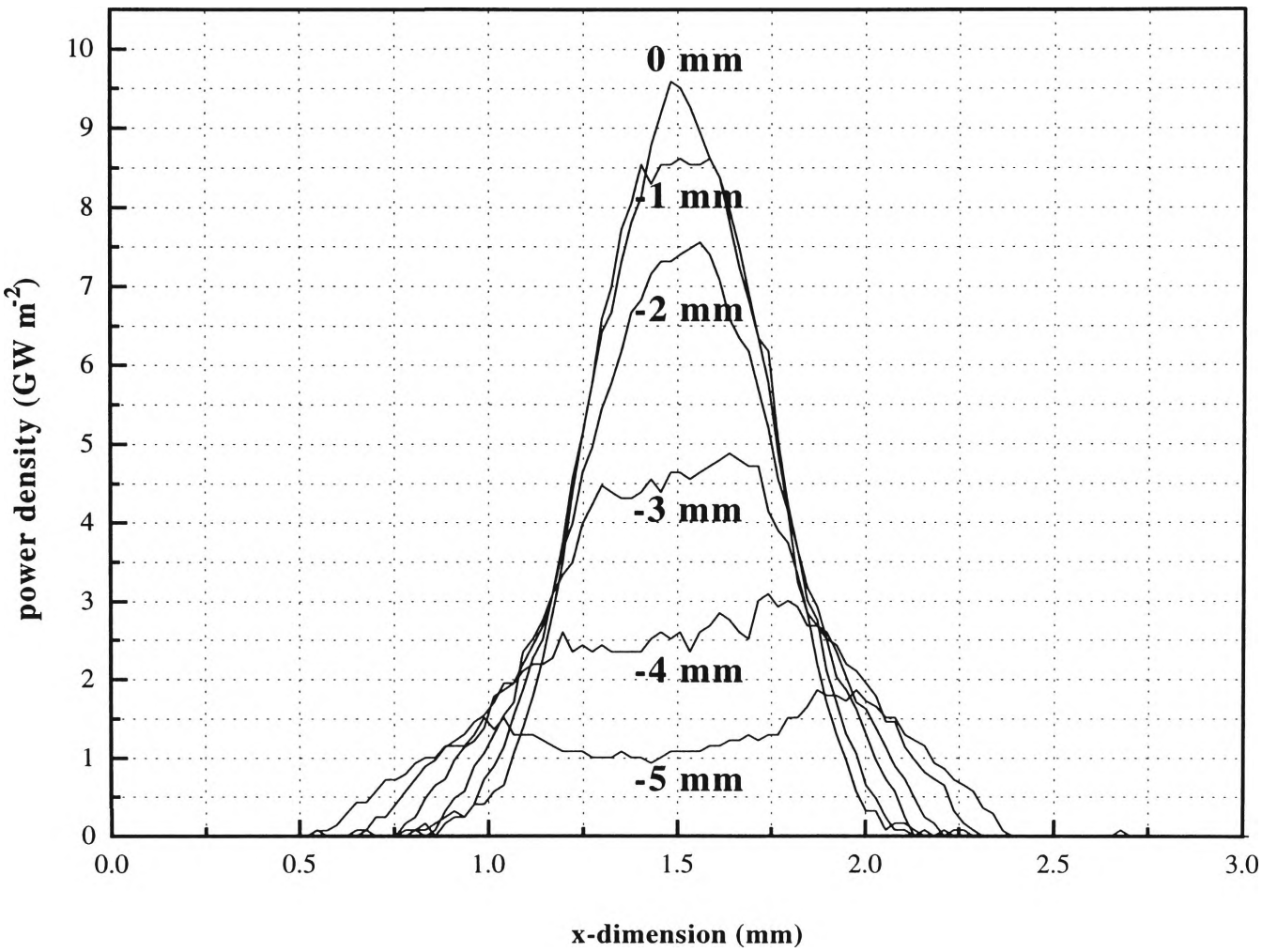

Figure 3.3 Centre-line intensity profiles as a function of focal position.
Laser conditions: 7 J, 3 ms.

Therefore, by manipulating beam profile data, a computer program was written to simulate various angles of irradiation.

The beam profile data was also used as the basis for other calculations. Tandem-beam profiles were simulated by displacing, overlapping and adding single-beam profiles, of different energies and focal positions, within the ANSYS program itself. The parametric design capabilities of the program were extended for this purpose.

3.3.3 Experimental design for comparison of models with experiment

In order to compare the results of various experiments with the numerical and analytical model predictions presented in Chapter 5, a sequence of experiments of increasing complexity was selected. These are described in sections 3.3.4 to 3.3.8 inclusive. In each case a series of spot welds or seam welds was produced. These welds were subsequently sectioned and examined. The weld dimensions and microstructures were analysed and compared with the calculations of the various models developed in the present study. The production of non-overlapping spot welds, in both single- and tandem-beam configurations, allowed the model predictions and experimental measurements to be compared for a weld produced by a single laser pulse. The much more complex case of overlapping spot welds, to form a seam weld, could then be considered with some confidence. Single- and tandem-beam welds on the materials described above served to highlight the influence of laser parameters and material properties on the laser welding process.

3.3.4. Single-beam non-overlapping spot welds

In the simplest case, non-overlapping spot welds were produced on 0.9 mm AISI 1006 steel. Laser pulses of duration 3 ms, energy 7 J and repetition rate 20 Hz were incident on the workpiece, moving fast enough (3000 mm/min) to ensure no overlap of these spot welds. Thus the effect of a single laser spot could be examined. The beam was incident on the surface of the material at an angle of 10° and a focal scan was made from -5 mm (focal point beneath the surface) to +5 mm (above the surface), in

increments of 1 mm.

As discussed in Chapter 4, keyholing was evident between the limits of -2 mm and +2 mm inclusive. Maximum penetration occurred when the laser beam was focussed at the surface of the workpiece (focus 0 mm). Although maximum penetration is often quoted to correspond to a focal position slightly below the surface[35], the results obtained in this experiment can be explained by the fact that the employed power densities were very close to the threshold limit for keyholing. An energy scan at focus 0 mm for energies of 3 J, 5 J, 9 J and 11 J was undertaken to provide further information for comparison with model predictions.

It should be noted that the adjustable parameters of pulse duration and repetition rate were kept constant throughout this experiment and all subsequent experiments. The results of preliminary experiments revealed that these parameters provided both appropriate peak power densities and spot weld overlaps for the welding performed in this work.

3.3.5 Single-beam overlapping spot welds

The experiment outlined in section 3.3.4 was extended to consider the case of overlapping spot welds. Laser pulses of energy 7 J, duration 3 ms, repetition rate 20 Hz and focus 0 mm were selected. Under these conditions, speeds of 700 mm/min and 350 mm/min ensured approximately 5% and 50% overlap, respectively. Using the latter speed, temperature-time predictions of various points on the top and bottom surfaces of the steel were compared with pyrometric measurements. The results of these thermal history comparisons, coupled with comparisons of weld bead dimensions, provided the necessary confidence to proceed to the more complex task of modelling two laser beams in tandem.

An energy scan at 350 mm/min was also performed to determine the energy required to weld the AISI 1006 steel in the butt configuration.

3.3.6 Tandem-beam non-overlapping spot welds

To ascertain the influence of a second beam in tandem with the main welding beam, a 50%-50% beam splitter was used to divide a laser beam of energy 14 J into two beams of equal energy (7 J, 7 J). The experimental arrangement is shown in Figure 3.4. The main beam (focus 0 mm) was incident on the workpiece at an angle of 10° after passing through the 5-m fibre-optic cable and main processing head, while a highly defocussed minor beam (focus -5 mm) was incident on the workpiece at an angle of 45° after passing through the 10-m fibre-optic cable and minor processing head. Although the angle of the main beam resulted in an approximately circular laser spot, the projection of the minor beam onto the surface resulted in an elliptical laser spot. Combining both beams in tandem resulted in a "composite" laser spot. The following inter-beam distances (expressed in mm) were examined:

- d = +0.2, +0.4, +0.6, +0.8, +1, +2, +3, +4, +5 (minor pre-heat beam)
- d = 0 (full overlap)
- d = -0.2, -0.4, -0.6, -0.8, -1, -2, -3, -4, -5 (minor post-heat beam)

A speed of 3000 mm/min was selected to ensure no overlap of "tandem" or "composite" spot welds. As a comparison, this experiment was repeated with the focal position of the second beam changed to 0 mm.

3.3.7 Tandem-beam overlapping spot welds

The above analysis was extended to consider the case of overlapping spot welds associated with tandem beams. With a speed of 350 mm/min, the following inter-beam distances (mm) were again examined:

- d = +0.2, +0.4, +0.6, +0.8, +1, +2, +3, +4, +5 (pre-heat)
- d = 0 (full overlap)
- d = -0.2, -0.4, -0.6, -0.8, -1, -2, -3, -4, -5 (post-heat)

Figure 3.4 Experimental arrangement for tandem fibre-optic laser welding showing both processing heads and fibre-optic cables.

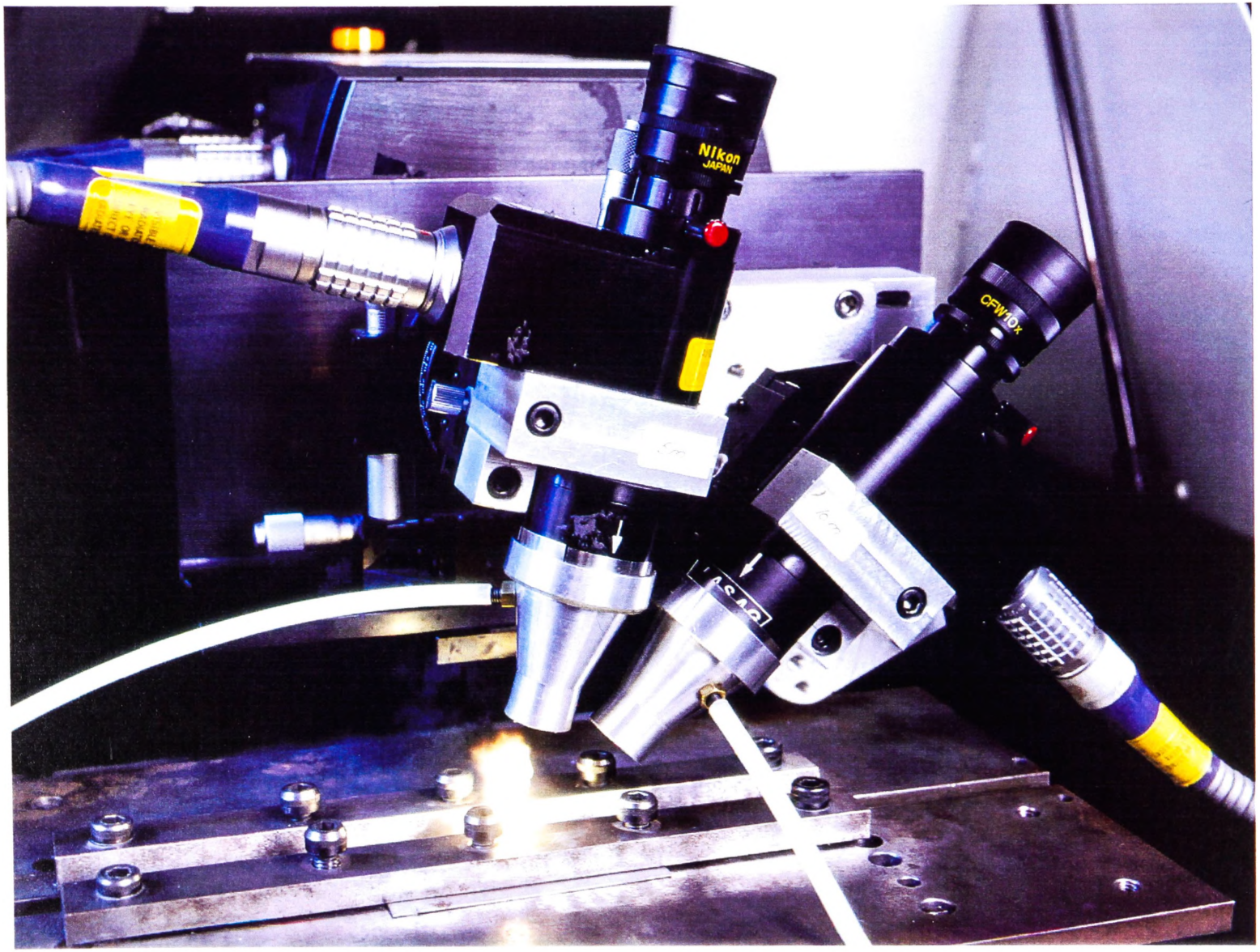
Nikon
JAPAN
CFW10x

The experiment was repeated with the focal position of the second beam changed to 0 mm. Optimum laser conditions were then determined to weld the AISI 1006 steel in the butt configuration.

To check the results of the numerical model of tandem-beam pulsed laser welding with the corresponding conduction-limited analytical model, it was necessary to select conditions which would produce conduction-limited welds. This was achieved by reducing the energy of each beam to 2 J. A speed of 350 mm/min was again selected, as well as inter-beam distances of -1 mm, 0 mm and +1 mm. Each beam was focussed at the surface to ensure a profile which could be closely approximated by a Gaussian distribution and therefore accommodated by the analytical model. The donut-shaped distribution at focus -5 mm does not allow this approximation to be made. As a further comparison, this experiment was repeated with the energy of each beam reduced to 1 J.

3.3.8 A5005 aluminium alloy

In order to test the numerical model on a different material with quite different properties, in this case A5005 aluminium alloy of thickness 0.8 mm, laser pulses of duration 3 ms, energy 20 J and repetition rate 20 Hz were incident on the workpiece, moving fast enough (3000 mm/min) to ensure no overlap of spot welds. Just as for the non-overlapping spot welds on AISI 1006 steel, a single beam was again incident on the surface of the material at an angle of 10° and a focal scan was made from -5 mm to +5 mm, in increments of 1 mm. The energy of 20 J was selected to produce a keyhole weld at focus 0 mm.

To provide experimental data for comparison with the conduction-limited analytical model, the energy was reduced until a conduction-limited weld at focus 0 mm was produced. The analytical model could not be employed for focal positions above or below the surface, as the shape of the beam profile did not warrant a Gaussian approximation.

3.3.9 Zincseal and Zincalume

To complete the study, it was necessary to determine optimum tandem welding conditions for the two coated steels. By varying the focal position of the pre-heat beam, a focal scan on each coated steel was performed as a guide in determining the focal position (and hence power density) required to remove the coating to at least the width of the subsequent weld bead with minimal melting of the base metal. The details of this experiment are discussed in section 3.4.2. Once this parameter was established, an inter-beam distance scan was undertaken to determine the optimum separation of the two beams. The following inter-beam distances (mm) were examined:

- d = +0.2, +0.4, +0.6, +0.8, +1, +2, +3, +4, +5 (pre-heat)
- d = 0 (full overlap)

The results of these tandem-beam trials were compared with the results of trials without the pre-heat beam. Using the knowledge obtained from this experiment, each coated steel was welded in the butt configuration using both single- and tandem-beam arrangements. These welds were then compared with single- and tandem-beam butt joints of the uncoated AISI 1006 steel.

3.4 TECHNIQUES

3.4.1 Optical and electron microscopy

All the AISI 1006 and coated steel specimens for metallographic analysis were mechanically ground using successively finer grades of SiC abrasive paper, followed by diamond paste polishing down to 1 μm. A final 0.06-μm colloidal silica polish was employed, followed by etching in 2.5% Nital. For non-overlapping spot welds, the depth and diameter of the FZ and weld zone (WZ = FZ + HAZ) in longitudinal sections were then measured using a Leitz optical microscope. For overlapping spot welds, only the depths of the FZ and WZ in longitudinal sections were measured. However, transverse sections were examined to provide the widths of the FZ and WZ for selected comparisons between experiment and theory. The different types of section are shown in

Figure 3.5. The microconstituents of the FZ and HAZ of each weld bead were determined by both optical microscopy and electron microscopy. A JSM 5400LV scanning electron microscope was used in the latter case.

A similar procedure was used for the A5005 aluminium alloy specimens. However, the low hardness of the alloy (60 HV 5) required the use of more resilient polishing cloths to avoid the embedding of diamond polishing particles within the specimens. An etchant consisting of 0.5 ml hydrofluoric acid (40% w/w) and 99.5 ml distilled water was used.

3.4.2 Energy dispersive spectroscopy

For both the Zincseal and Zincalume coated steels, energy dispersive spectroscopy in a scanning electron microscope (JSM 5400LV) was used to determine the amount of coating remaining on the surface of each coated steel after the traverse of just the pre-heat beam. In each case, an energy of 7 J and a speed of 350 mm/min were used for focal positions between 0 mm and -5 mm inclusive, in increments of 1 mm. This range of focal positions ensured a wide variation in the shape of the laser beam profile. In this manner, the effect of energy distribution on the removal of each coating was determined. This preliminary bead-on-plate study was used as a guide in determining the optimum focal position of the pre-heat beam for maximum coating removal prior to full-penetration butt welding.

3.4.3 Microhardness and microstructure

A Matsuzawa Seiki microhardness indentation system was used to determine the variation in hardness within the fusion zone and heat-affected zone of various weld beads produced in the present study. This was achieved by superimposing a 9x9 indentation grid pattern on a particular spot weld from a train of overlapping or non-overlapping bead-on-plate spot welds. Each spot weld was divided into zones and the hardness values within each of these zones were then averaged to provide an average hardness for

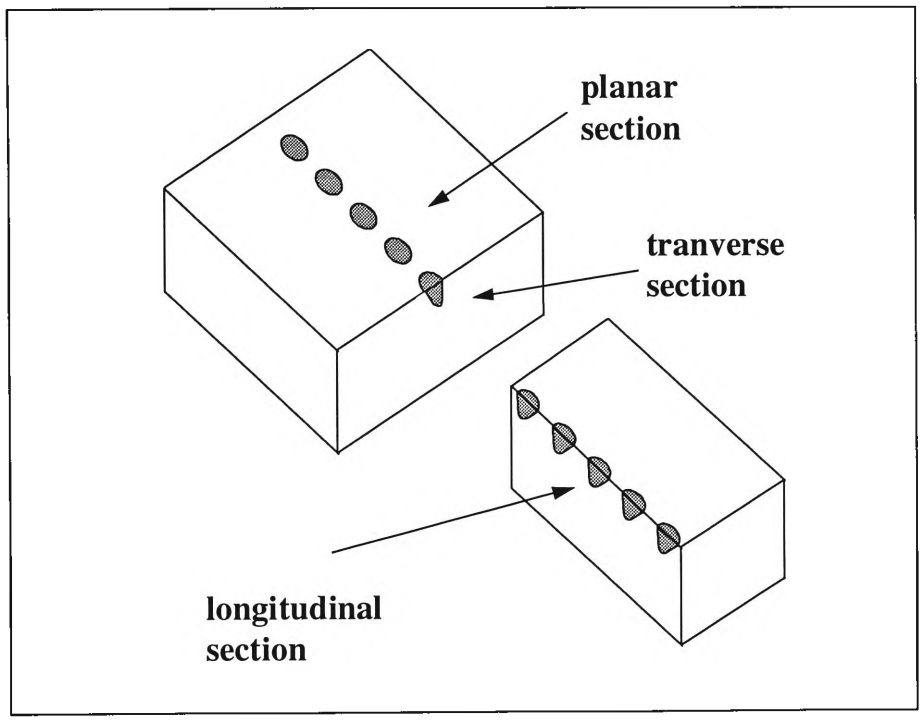

Figure 3.5 Longitudinal, transverse and planar sections used in the metallographic examination of weld beads. Non-overlapping weld beads are shown.

each zone. These average microhardness readings were checked with macrohardness readings of each zone and then correlated with the observed microconstituents.

3.4.4 Tensile tests

As pulsed laser welding produces a series of overlapping spot welds, the tensile test results can be complicated by a variation in the strength and ductility from point to point across the weld joint. Furthermore, if the strength of the weld metal exceeds that of the base metal, the specimen will fail outside the weld area. This indicates that the tensile strength of the weld metal exceeds that of the base metal. Quantitative comparisons of various welds are not possible when failures of this type occur.

In the present study, optimum single- and tandem-beam laser conditions were determined for welding AISI 1006 steel, Zincseal and Zincalume in the butt configuration. Tensile test specimens of gauge length 25 mm were then cut out by the laser according to the standards of the American Society for Testing of Materials[124]. In all cases, laser pulses of energy 1 J, duration 0.5 ms and repetition rate 100 Hz were used. The cutting speed was 500 mm/min. The specimens were then strained to fracture in an Instron 1341 tensile testing machine. The type of failure for each specimen was recorded, as well as the parameters of tensile strength and ductility. These values were determined from stress-strain graphs produced during the tests.

3.4.5 Formability tests

The formability of a material is the relative ease with which a material can be shaped. Several tests have been developed to evaluate the formability of a material. In the present study, the Erichsen test[125] was used to assess the formability of single- and tandem-beam butt joints of AISI 1006 steel, Zincseal and Zincalume. Each sample was clamped rigidly by means of two 25.4-mm dies and then stretched over a small hemispherical punch of diameter 20 mm. The formability or "stretchability" of the weld was then assessed by measuring the height to which the weld could be stretched before fracture occurred. This height or punch displacement was then compared with the punch

displacement of the base metal in terms of a %reduction in formability. The type of failure was also recorded.

In the Erichsen test, fracture occurs under conditions when the strain is approximately the same in the two perpendicular directions (equi-biaxial strain). However, in the uniaxial tension test described in section 3.4.4, fracture is associated with a combination of tensile strain and a small degree of contractual strain normal to the direction of the applied load. In practical press-forming operations, most fractures tend to occur under plane strain conditions, which lie somewhere between the conditions associated with the Erichsen and tensile tests. For this reason, the limiting dome height test, which requires a large-diameter hemispherical punch and steel strips of varying width, can be used to simulate more effectively the fracture conditions found in most parts. Each strip is marked with a grid of small circles, and the "width strain" at fracture is measured from the circle closest to the point of fracture. This test is, however, a complex and time-consuming test, and the results are critically dependent on the sheet thickness. The Erichsen and tensile tests were therefore selected to provide a very quick and simple means of assessing weld quality. When complemented with the hardness tests and microscopic techniques also perfomed in this study, these tests were deemed to be appropriate.

CHAPTER 4

MICROSTRUCTURAL CHARACTERISATION

4.1 INTRODUCTION

This chapter presents a characterisation of bead-on-plate laser welds observed on cold-rolled, spheroidised AISI 1006 steel. Both non-overlapping and overlapping spot weld arrangements associated with single- and tandem-beam radiation are considered. The dimensions of fusion zones and weld zones are provided in section 4.2, as well as hardness profiles of both zones. The analysis is repeated for selected single- and tandem-beam overlapping spot welds on each coated steel. The results of tensile and formability tests on full-penetration butt joints are then used to assess weld strength, ductility and formability.

In section 4.3, the microstructures observed in the weld metal of each bead-on-plate weld are explained in terms of rapid solidification theory. The heat-affected zone structure in the base plate is rationalised in terms of the rapid thermal cycling experienced. A microstructural comparison with conventional fusion welds is also made. Since microstructural development has a critical effect on the mechanical properties of welds, microstructural characterisation plays an integral role in not only an understanding of pulsed laser welding, but also in the selection of optimum welding conditions for the material of interest.

4.2 RESULTS

4.2.1 Single-beam non-overlapping spot welds

A montage of micrographs from focus -5 mm to +5 mm is presented in Figure 4.1, showing the cross-sections of single-pulse laser spot welds formed as the focal position of the laser beam was varied between -5 mm (below the surface) to +5 mm (above the surface). The energy used in each case was 7 J. From such micrographs the depth and diameter of the fusion zone (FZ) and weld zone (WZ = FZ + HAZ) have been measured. FZ and WZ depths have been plotted in Figure 4.2(a), while FZ and WZ diameters can be seen in Figure 4.2(b). It was found that the diameter of the spot weld was relatively insensitive to focal position, decreasing slightly in diameter as the focus shifted from beneath the surface of the steel sheet (-ve) to above the surface (+ve). FZ

Figure 4.1 Micrographs of the longitudinal sections of laser spot welds on AISI 1006 steel from focus +5 mm to focus -5 mm (x 25).
Conditions: 7 J, 3 ms, 20 Hz, 3000 mm/min.

-3

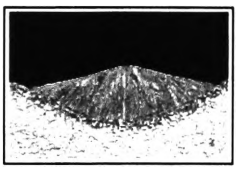

-4

-2

-5

-1

0

+5

+1

+4

+2

+3

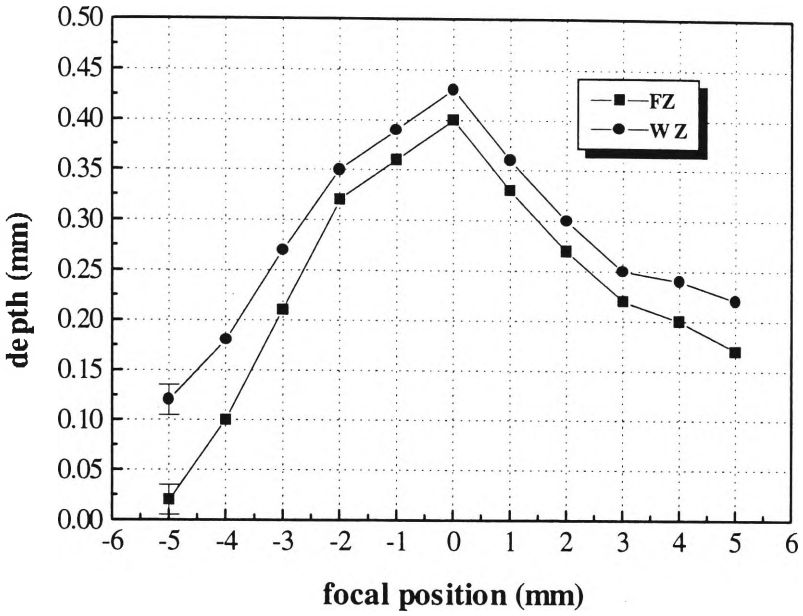

Figure 4.2(a) Longitudinal section data for FZ and WZ depth vs. focal position.
Conditions: 7 J, 3 ms, 20 Hz, 3000 mm/min.
Note that the WZ depth corresponds to the sum of the FZ and HAZ depths.

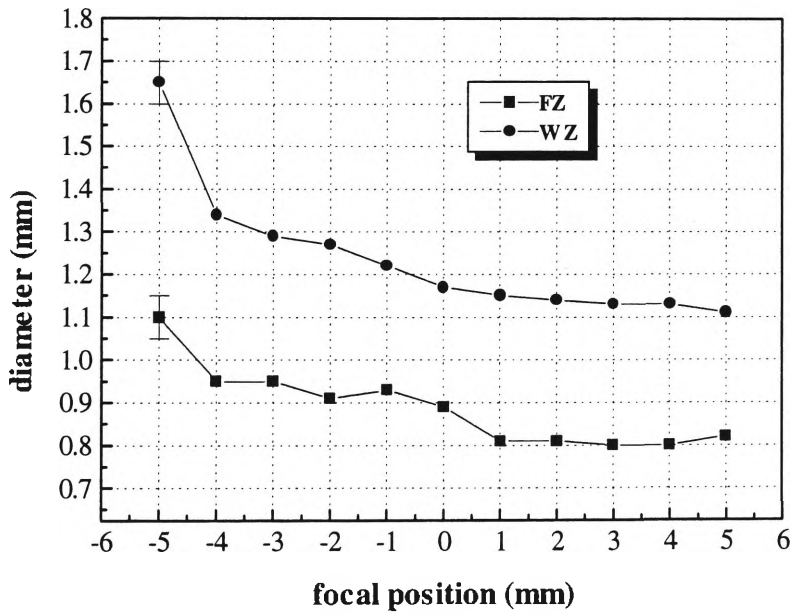

Figure 4.2(b) Planar section data for FZ and WZ diameter vs. focal position.
Conditions: 7 J, 3 ms, 20 Hz, 3000 mm/min.

and WZ depth were far more dependent on focus, with maximum penetration being obtained when the laser beam was focussed at the surface of the workpiece (focus 0 mm). Keyholing was evident between -2 mm and +2 mm. The asymmetrical appearance of the spot welds between these focal positions is a direct consequence of the beam incidence angle of 10°. Penetration was reduced sharply on shifting the focal position away from the surface.

As maximum penetration occurred when the laser beam was focussed at the surface of the material (focus 0 mm), magnified micrographs of both longitudinal and planar sections are shown in Figures 4.3(a) and 4.3(b), respectively. A longitudinal section of a representative FZ-HAZ interface is shown in Figure 4.3(c). The main microconstituents of the FZ are lath martensite (M_L) and bainitic ferrite, also known as ferrite with an aligned second phase (FS(A)). The HAZ consists of martensite or martensite-austenite islands in a ferrite matrix. The evolution of the observed microstructure is explained in detail in section 4.3.

A microhardness profile of the spot weld is shown in Figure 4.3(d). The high average hardness (349 HV 0.025) of the fusion zone is consistent with the observation of an almost completely martensitic structure. The macrohardness of a martensitic 0.06% C alloy is predicted to be about 360 HV 20[126]. The decreasing proportion of hard martensite or martensite-austenite islands on moving radially outward from the fusion boundary explains the lower average hardness in the HAZ. The decreasing volume fraction of martensite is complemented by an increase in the softer ferrite phase. A similar trend was observed for all other spot welds.

4.2.2 Single-beam overlapping spot welds

The longitudinal sections of the overlapping spot welds for speeds of 700 mm/min and 350 mm/min are shown in Figures 4.4(a) and 4.5(a), respectively. In the former case, spot weld overlap is approximately 5%, while 50% overlap is evident in the latter case. Nevertheless, the depths of the fusion zone and weld zone are approximately the same in each case, i.e. 0.48 mm and 0.52 mm. It should be noted that these

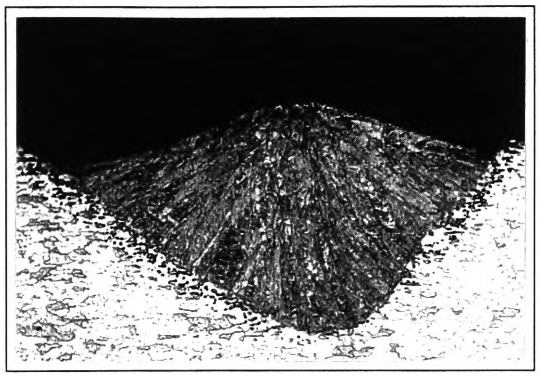

(a) Micrograph of the longitudinal section (x 60).

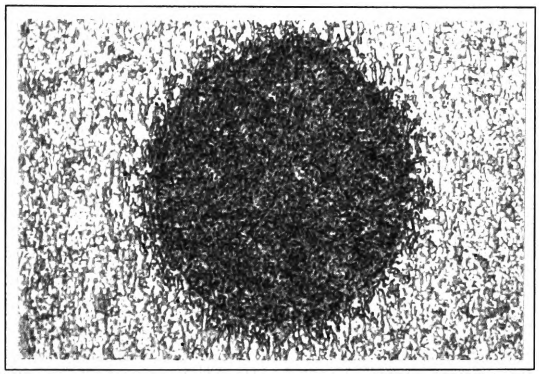

(b) Micrograph of the planar section (x 60).

(c) Micrograph of the HAZ (x 300).

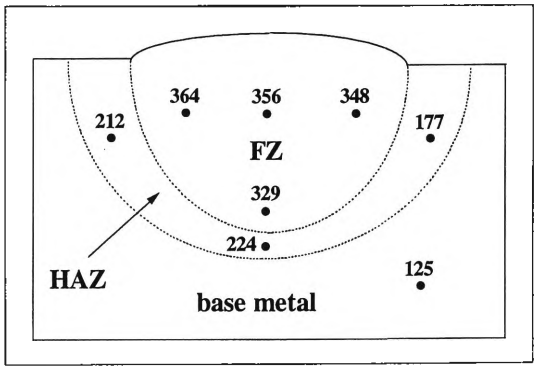

(d) Schematic representation of the microhardness profile.

Figure 4.3 Examination of a single laser spot weld.
Conditions: 7 J, focus 0 mm, 3 ms, 20 Hz, 3000 mm/min.

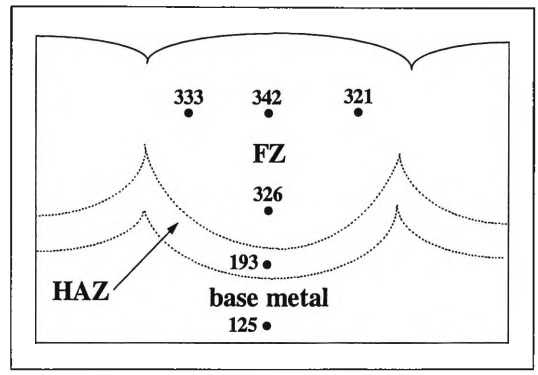

(a) (b)

Figure 4.4 (a) Micrograph (x 60) and (b) schematic hardness profile of the longitudinal section of a series of overlapping spot welds.
Conditions: 7 J, focus 0 mm, 3 ms, 20 Hz, 700 mm/min.

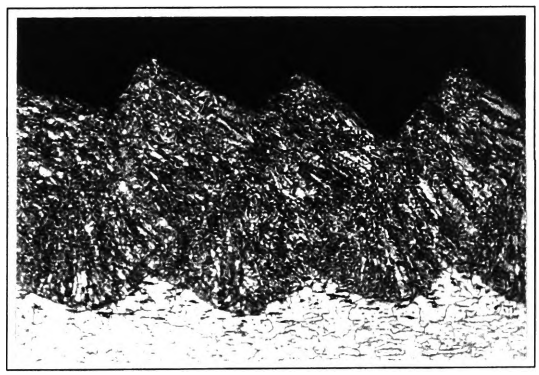

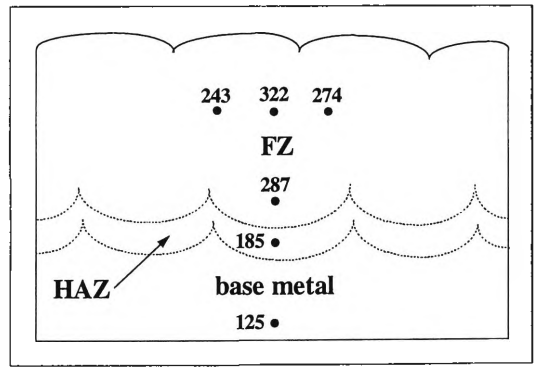

(a) (b)

Figure 4.5 (a) Micrograph (x 60) and (b) schematic hardness profile of the longitudinal section of a series of overlapping spot welds.
Conditions: 7 J, focus 0 mm, 3 ms, 20 Hz, 350 mm/min.

dimensions were obtained by measuring the distance between the bottom surface of the sheet and the respective boundaries. Since the surface has melted and subsequently resolidified into an undulating series of peaks and troughs, measurement from the top surface was not possible.

As illustrated in Figures 4.4(b) and 4.5(b), the average microhardness values in the FZ of the 700 mm/min and 350 mm/min welds were 331 and 282 HV 0.025 respectively, lower than the average of 349 found for the welding speed of 3000 mm/min. This result is consistent with the higher heat inputs corresponding to lower welding speeds and the lower cooling rates which result in lower proportions of martensite. In addition, the overlapping weld beads result in partial re-austenitisation of as-cast structure leading to narrow bands of a fine-grained, normalised ferrite structure on cooling.

4.2.3 Tandem-beam non-overlapping spot welds

A 50% beam splitter was introduced to divide a laser beam of energy 14 J into two separate beams of energy 7 J. The first or main beam was focussed at the surface, while the second or minor beam was focussed at -5 mm. A workpiece speed of 3000 mm/min produced non-overlapping, asymmetrical spot welds. A selection of micrographs for inter-beam distances of +1 mm, 0 mm and -1 mm is shown in Figure 4.6. A positive inter-beam distance indicates that the second, highly defocussed beam leads the main beam (pre-heating). Conversely, a negative distance implies that the second beam lags the main beam (post-heating).

When the second beam was also focussed at the surface, asymmetrical spot welds of quite different dimensions were produced. Representative micrographs for inter-beam distances of +1 mm, 0 mm and -1 mm are shown in Figure 4.7.

The maximum depth of the FZ and WZ as a function of inter-beam distance for both sets of conditions has been plotted in Figures 4.8 (second beam focus -5 mm) and 4.9 (second beam focus 0 mm). In each case, the average hardness of the FZ and HAZ

(a) d = +1 mm

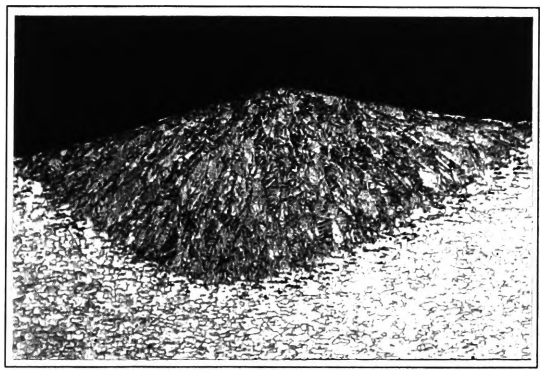

(b) d = 0 mm

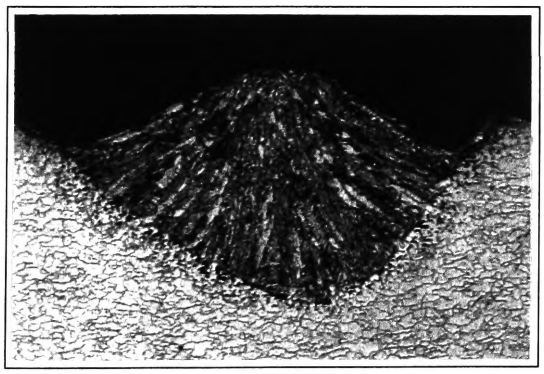

(c) d = -1 mm

Figure 4.6 Longitudinal sections of tandem-beam non-overlapping spot welds for inter-beam distances of (a) +1 mm, (b) 0 mm and (c) -1 mm (x 60). Conditions: beam 1 - focus 0 mm, 7 J; beam 2 - focus -5 mm, 7 J.

(a) d = +1 mm

(b) d = 0 mm

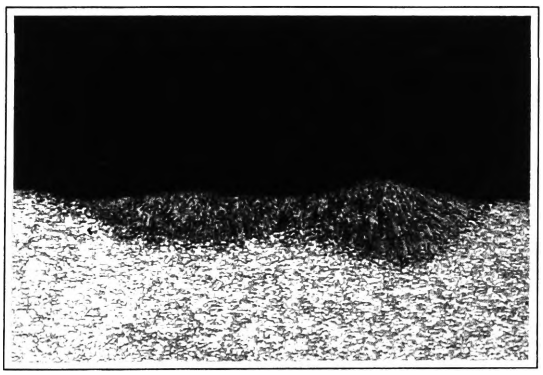

(c) d = -1 mm

Figure 4.7 Longitudinal sections of tandem-beam non-overlapping spot welds for inter-beam distances of (a) +1 mm, (b) 0 mm and (c) -1 mm (x 30). Conditions: beam 1 - focus 0 mm, 7 J; beam 2 - focus 0 mm, 7 J.

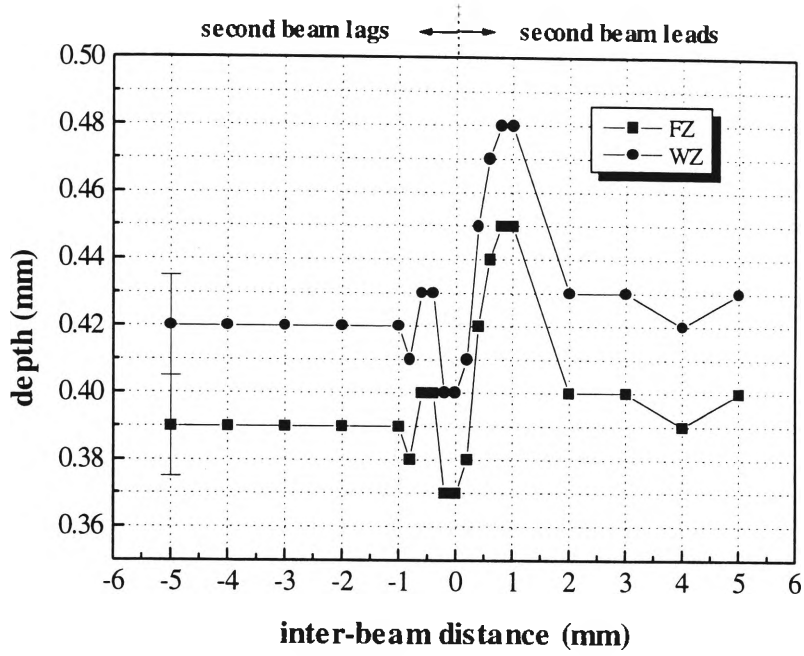

Figure 4.8 Longitudinal section data for FZ and WZ depth of tandem-beam non-overlapping spot welds.

Conditions: beam 1 - focus 0 mm, 7 J; beam 2 - focus -5 mm, 7 J.

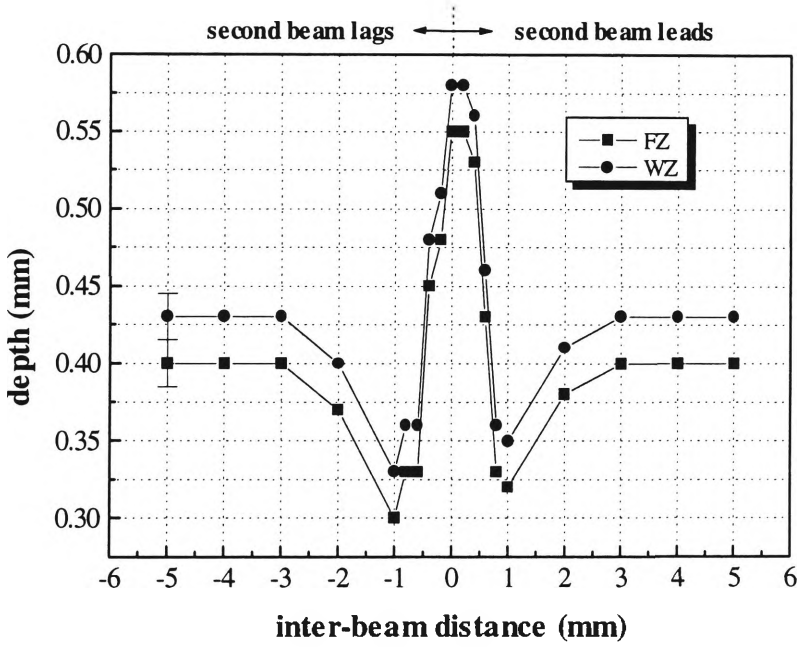

Figure 4.9 Longitudinal section data for FZ and WZ depth of tandem-beam non-overlapping spot welds.

Conditions: beam 1 - focus 0 mm, 7 J; beam 2 - focus 0 mm, 7 J.

was found to be very similar to the hardness profile associated with the single-beam spot weld shown in Figure 4.3(d). This indicates that the cooling rates for all of the tandem-beam spot welds were fast enough to produce fusion zones which are almost entirely martensitic. The narrow HAZ in each case again consists of martensite or martensite-austenite islands in a ferrite matrix.

Noticeably different, however, is the size and shape of the composite spot weld for each set of welding conditions. It must be remembered that the two overlapping spots are elliptical, as they are incident upon the surface of the workpiece at 10° and 45° for the main beam and the minor beam, respectively. Figures 4.8 and 4.9 indicate that when the two beams are not overlapping, the FZ depth is about 0.39 - 0.4 mm and the WZ depth is 0.42 - 0.43 mm. When both beams are focussed at the surface (Figure 4.9) and completely overlapped (inter-beam distance 0 mm), the depth of penetration increases markedly to 0.58 mm. The simple interpretation of the increase in penetration is that it is due to the increase in total power density at the surface of the material as a result of the superposition of the two beams. This indeed is supported by the predictions of the numerical model which accurately predicts this increase in penetration (see section 5.5.3). For inter-beam distances on either side of this, however, the depth of penetration is observed to drop below that which would be expected if there were no minor beam.

Other factors clearly have an influence on the depth of penetration, factors which have not been incorporated into the model. These may include the production and consequent role of plasma formed above the weld area, the formation of a plasma-filled keyhole within the material during the laser pulse, the angular dependence of Fresnel absorption, and the effects of surface tension and flow in the molten weld pool. For instance, a combination of these factors for inter-beam distances of $\pm$ 1 mm may lead to absorption of the energy of the pre- or post-beam at the walls of a forming keyhole, with different absorption characteristics, and a counter-flow of molten material away from the centre of the weld. This may lead to a reduction in penetration depth compared to the case of absorption of the laser beam energy symmetrically within the interaction volume.

The effect of this complication is also seen when the second beam is defocussed to -5 mm, where it exhibits an asymmetrical donut intensity profile. The maximum

penetration depth of 0.48 mm occurs at an inter-beam distance of +1 mm. This is a direct result of the superposition of the near-Gaussian, focussed beam profile with the donut-shaped profile with a peak-to-peak distance of 1.2 mm. There is a significant contribution from the broad, asymmetrical beam to the peak intensity of the focussed beam. This results in a higher maximum power density than when the focussed beams are separated by 1 mm. The maximum penetration of 0.48 mm is still lower than that observed for the two overlapping, focussed beams as the maximum power density is lower. The presence of the other "parasitic" effects may also be seen, albeit asymmetrically, in the complex dependency of penetration on inter-beam distance (Figure 4.8).

4.2.4 Tandem-beam overlapping spot welds

Reducing the speed to 350 mm/min ensured at least 75% overlap of the composite spot welds. Micrographs for d = +1 mm, 0 mm and -1 mm are shown in Figure 4.10. In each case, the second beam was focussed at -5 mm. Schematic representations of each hardness profile are also shown. Figure 4.11 shows the corresponding micrographs and hardness profiles when the second beam was focussed at the surface (focus 0 mm). At high laser power densities, significant turbulence and spatter occur in the fusion zone, often leading to entrapped porosity. This is evident for d = 0 mm (Figure 4.11(b)).

The FZ depth and WZ depth of all weld beads are shown in Figures 4.12 (second beam focus -5 mm) and 4.13 (second beam focus 0 mm). The much slower welding speed has resulted in a general increase in the depth of fusion zones and weld zones, as well as a large reduction in the proportion of martensite in the FZ. This is reflected in the much lower hardness values recorded in the FZ. In general, a "normalised" structure of bainitic ferrite is the primary microconstituent toward the top of the FZ, while a partially re-austenitised region appears toward the base of the FZ. The HAZ consists of martensite or martensite-austenite islands within a matrix of coarse ferrite grains. This zone is wider than the HAZ observed in all of the non-overlapping spot welds. A closer study of these microstructures is presented in section 4.3.

Figure 4.10 Micrographs (x 30) and schematic hardness profiles of the longitudinal sections of tandem-beam overlapping spot welds for inter-beam distances of (a) +1 mm, (b) 0 mm and (c) -1 mm.
Conditions: beam 1 - focus 0 mm, 7 J; beam 2 - focus -5 mm, 7 J.

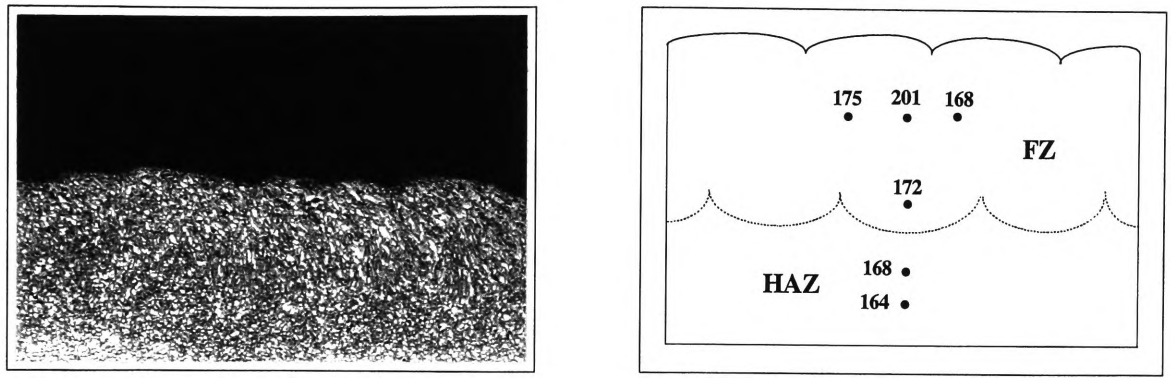

(a) d = +1 mm

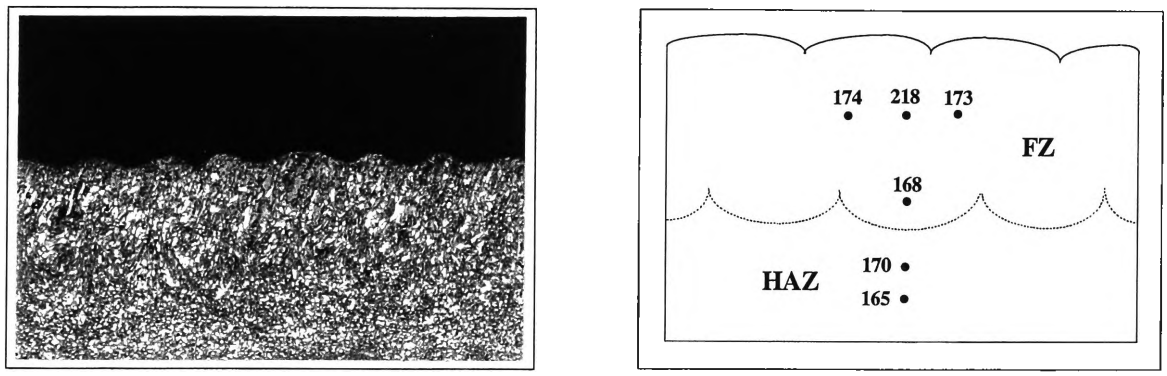

(b) d = 0 mm

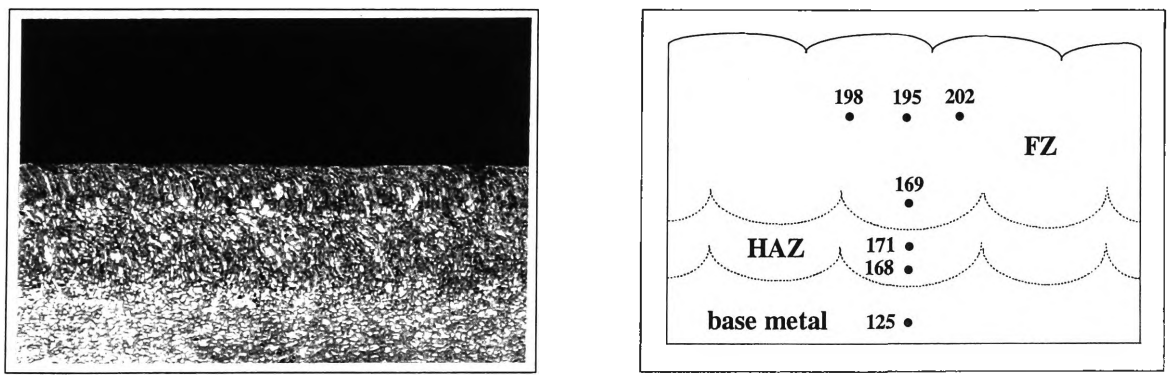

(c) d = -1 mm

Figure 4.11 Micrographs (x 30) and schematic hardness profiles of the longitudinal sections of tandem-beam overlapping spot welds for inter-beam distances of (a) +1 mm, (b) 0 mm and (c) -1 mm.
Conditions: beam 1 - focus 0 mm, 7 J; beam 2 - focus 0 mm, 7 J.

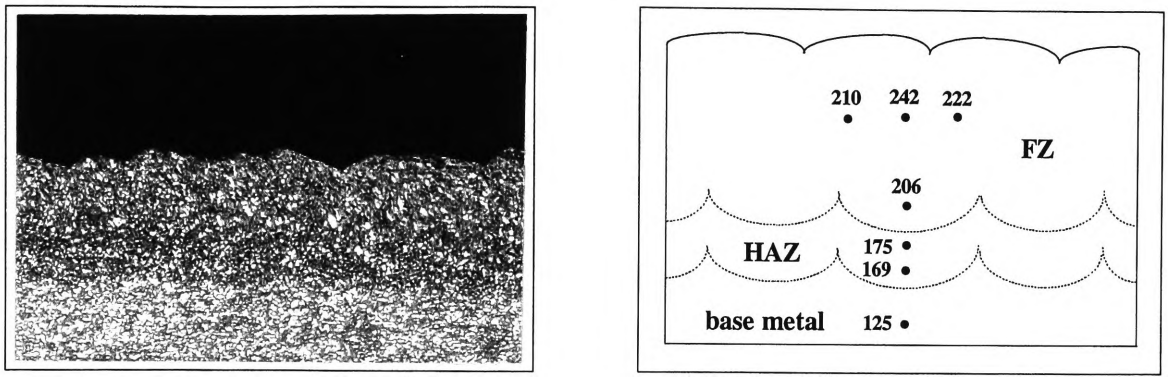

(a) d = +1 mm

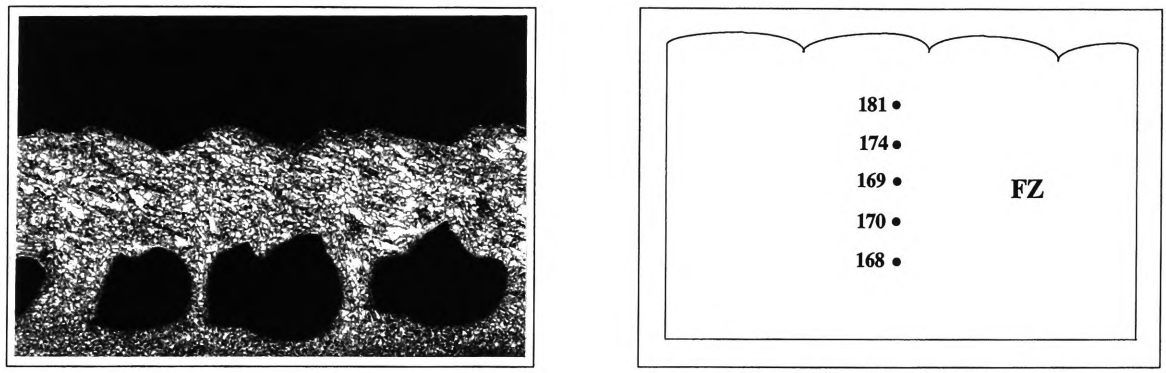

(b) d = 0 mm

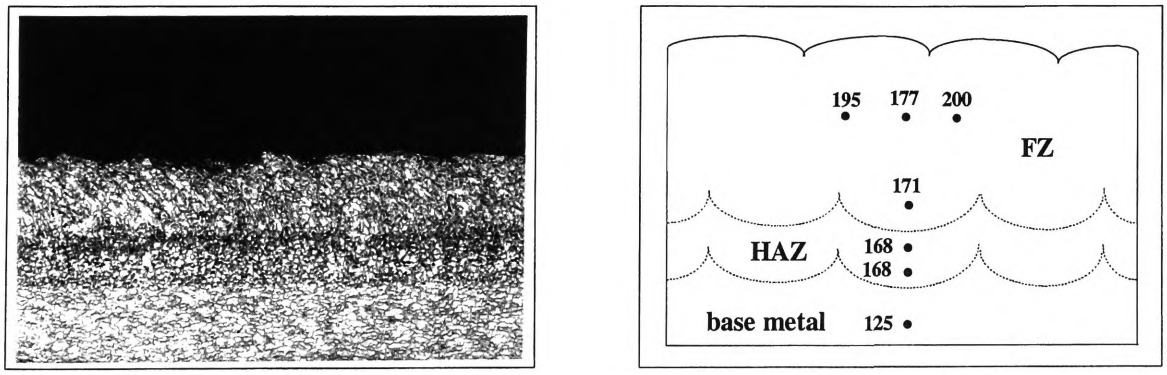

(c) d = -1 mm

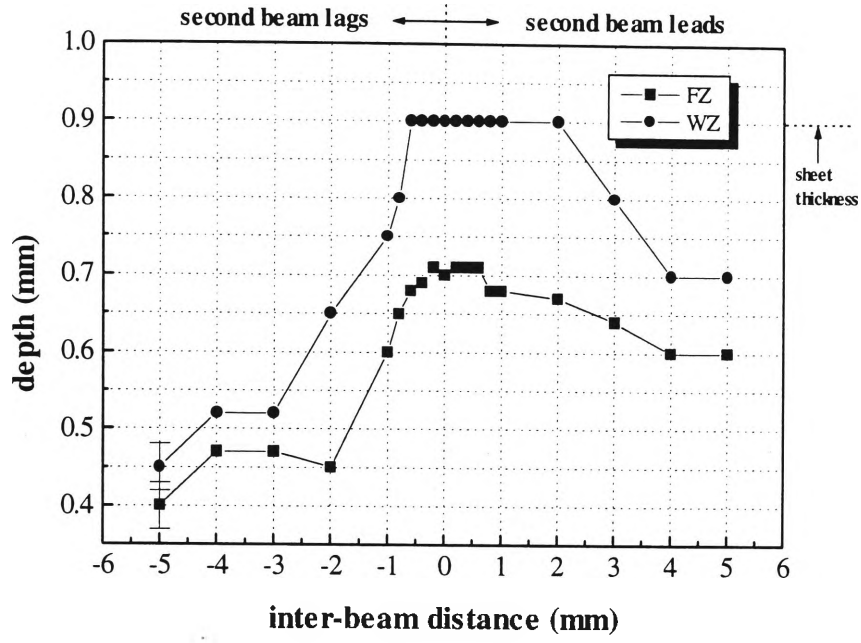

Figure 4.12 Longitudinal section data for FZ and WZ depth of tandem-beam overlapping spot welds.

Conditions: beam 1 - focus 0 mm, 7 J; beam 2 - focus -5 mm, 7 J.

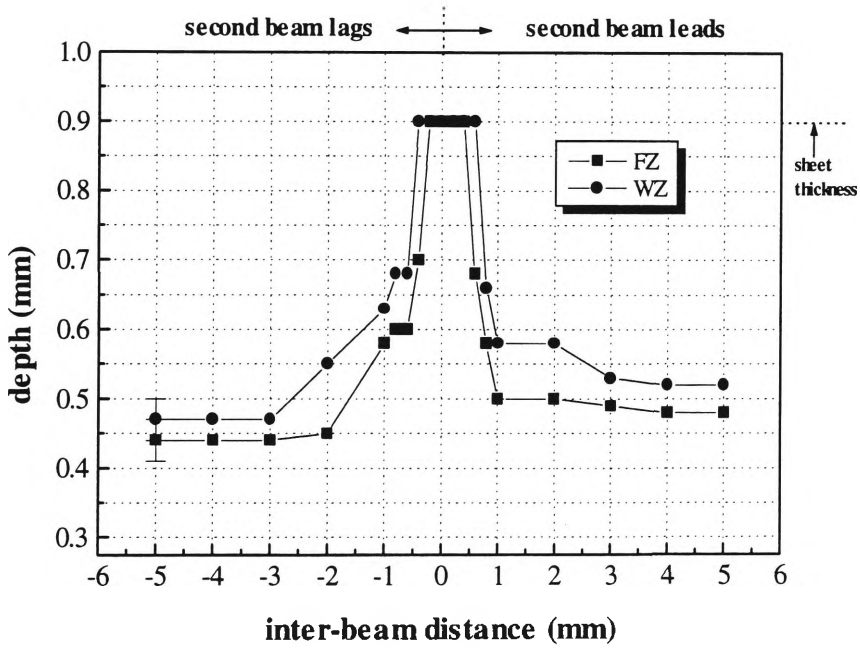

Figure 4.13 Longitudinal section data for FZ and WZ depth of tandem-beam overlapping spot welds.

Conditions: beam 1 - focus 0 mm, 7 J; beam 2 - focus 0 mm, 7 J.

4.2.5 Zincseal and Zincalume

The first stage in determining the optimum welding conditions for each coated steel involved the use of just the pre-heat beam to determine the power density and distribution which would remove the coating to at least the width of the subsequent weld bead with minimal melting of the base metal. This was achieved by using energy dispersive spectroscopy to record the elemental percent of zinc and aluminium remaining on the surface of each material as a function of focal position (and therefore power density). A pulse energy of 7 J and a speed of 350 mm/min were used.

In the case of the Zincseal coating, a graph of %Zn and %Al vs. focal position is shown in Figure 4.14. The same graph is presented in Figure 4.15 for the Zincalume coating. Although both graphs illustrate a general increase in coating removal on moving from focus -5 mm to 0 mm, the concomitant increase in power density results in an increase in the fusion depth of the base metal from approximately 20 μm to 400 μm for both coated steels. This leads to an increase in the degree of mixing of the coating with the base metal. On this basis a focal position of -5 mm was selected for the pre-heat beam. For Zincseal therefore, the pre-heat beam changes the composition of the surface layer from Zn-76.7%, Al-0.2%, Fe-23.1% to Zn-0.9%, Al-1.4%, Fe-97.7%. This indicates that a very large proportion of zinc is removed by the pre-heat beam. The presence of aluminium, which is normally added to the zinc bath to provide thinner and more flexible coatings by limiting the formation of intermetallic compounds of iron and zinc on the surface, appears not to have been removed to the same extent as the zinc. Transverse compositional analysis confirmed very little mixing of the coating with the base metal for Zincseal (< 0.3% zinc and < 0.5% aluminium in the fusion zone) using this focal position.

For Zincalume, the Zn-51.9%, Al-47.6%, Fe-0.5% composition of the surface layer is changed to Zn-7.5%, Al-30.0%, Fe-62.5%. Aluminium from the coating is mixed to some extent within the fusion zone (~8% aluminium, < 0.3% zinc) using a focus of -5 mm. The relatively low boiling point of zinc (906 °C) compared with that of aluminium (2520 °C) and iron (2860 °C) explains the ease with which the zinc is evaporated.

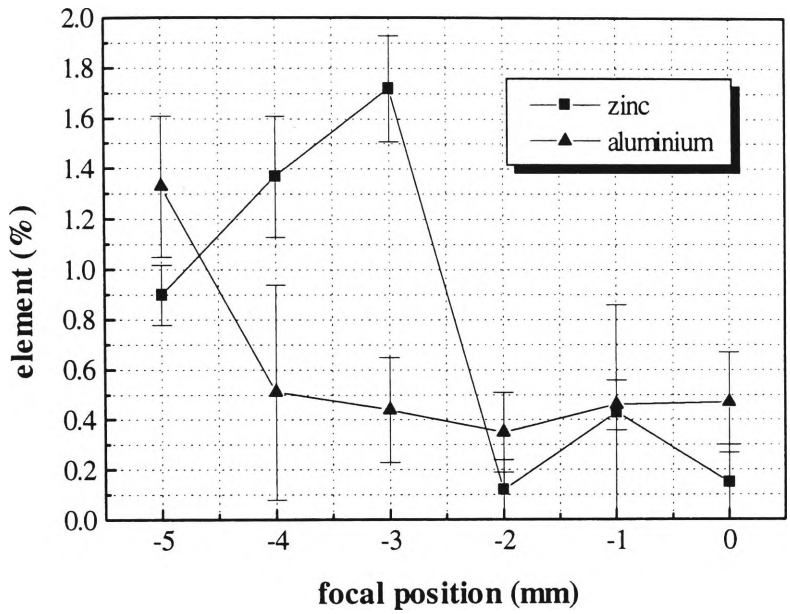

Figure 4.14 Graph of %Zn and %Al remaining on surface of Zincseal vs. focal position after the traverse of the pre-heat beam.
Coating composition: Zn-76.7%, Al-0.2%, Fe-23.1%.
Conditions: 7 J, 3 ms, 20 Hz, 350 mm/min.

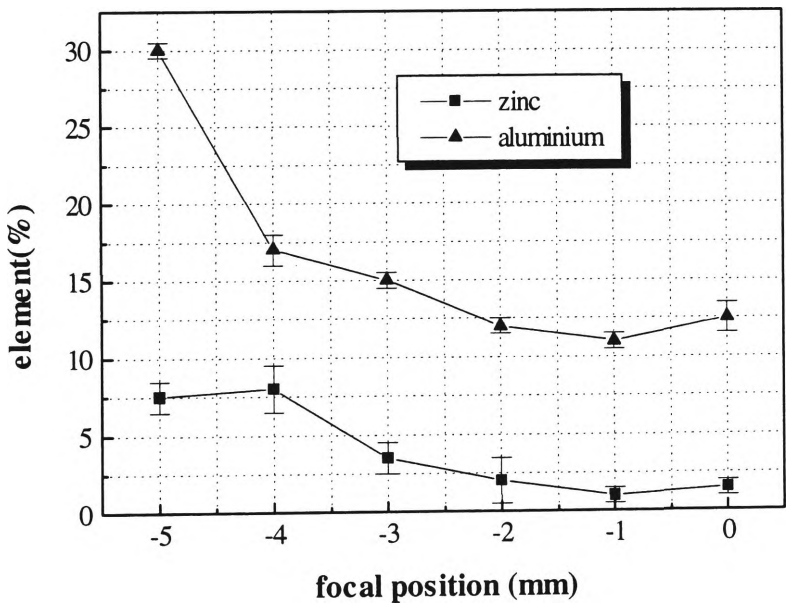

Figure 4.15 Graph of %Zn and %Al remaining on surface of Zincalume vs. focal position of pre-heat beam.
Coating composition: Zn-51.9%, Al-47.6%, Fe-0.5%.
Conditions: 7 J, 3 ms, 20 Hz, 350 mm/min.

After selecting the appropriate focal position of the pre-heat beam, an inter-beam distance scan between 0 and +3 mm in increments of 0.2 mm was performed to determine the optimum separation of the two beams, each of energy 7 J. The main beam was focussed at the surface of the workpiece to provide maximum energy density. Optical examination of the planar and longitudinal sections of each weld bead revealed that the weld quality for each coated steel was very good for separations of 0, 0.2 and 0.4 mm. For larger inter-beam distances, varying degrees of porosity and undercut were evident.

For this reason, an inter-beam distance of 0 mm was selected for welding each coated steel in the butt configuration. Owing to the donut-shaped profile of the second minor beam, this type of arrangement provides not only pre-heating of the workpiece, but also a large degree of post-heating. The effect of superimposing the donut-shaped beam profile of the minor beam onto the near-Gaussian profile of the main beam is illustrated in Figure 4.16.

Figure 4.17 shows a longitudinal section of tandem-beam overlapping spot welds on Zincseal for an inter-beam distance of 0 mm. A speed of 350 mm/min, a pulse duration of 3 ms and a repetition rate of 20 Hz were employed. In contrast, Figure 4.18 shows a micrograph of overlapping spot welds produced without the pre-heat beam. In both cases bainitic ferrite is observed in the FZ. Similar hardness values are apparent. The only observable difference is that the tandem-beam conditions have resulted in full penetration. For the single-beam weld, a HAZ consisting of dark-etching martensite or martensite-austenite islands within coarse grains of ferrite extends from the fusion zone boundary to the bottom surface of the plate.

Figures 4.19 and 4.20 show the corresponding bead-on-plate welds on Zincalume under the same laser conditions. In both cases, an aluminium-rich phase is present toward the surface. This arises from very little mixing of the coating within the weld pool during each short-duration pulse. Below this layer, the ferrite-stabilising elements of aluminium and zinc have produced columnar grains of ferrite within the lower section of the fusion zone. The lack of homogeneity within the weld pool has also resulted in some regions of bainitic ferrite and martensite within the FZ. These regions are more

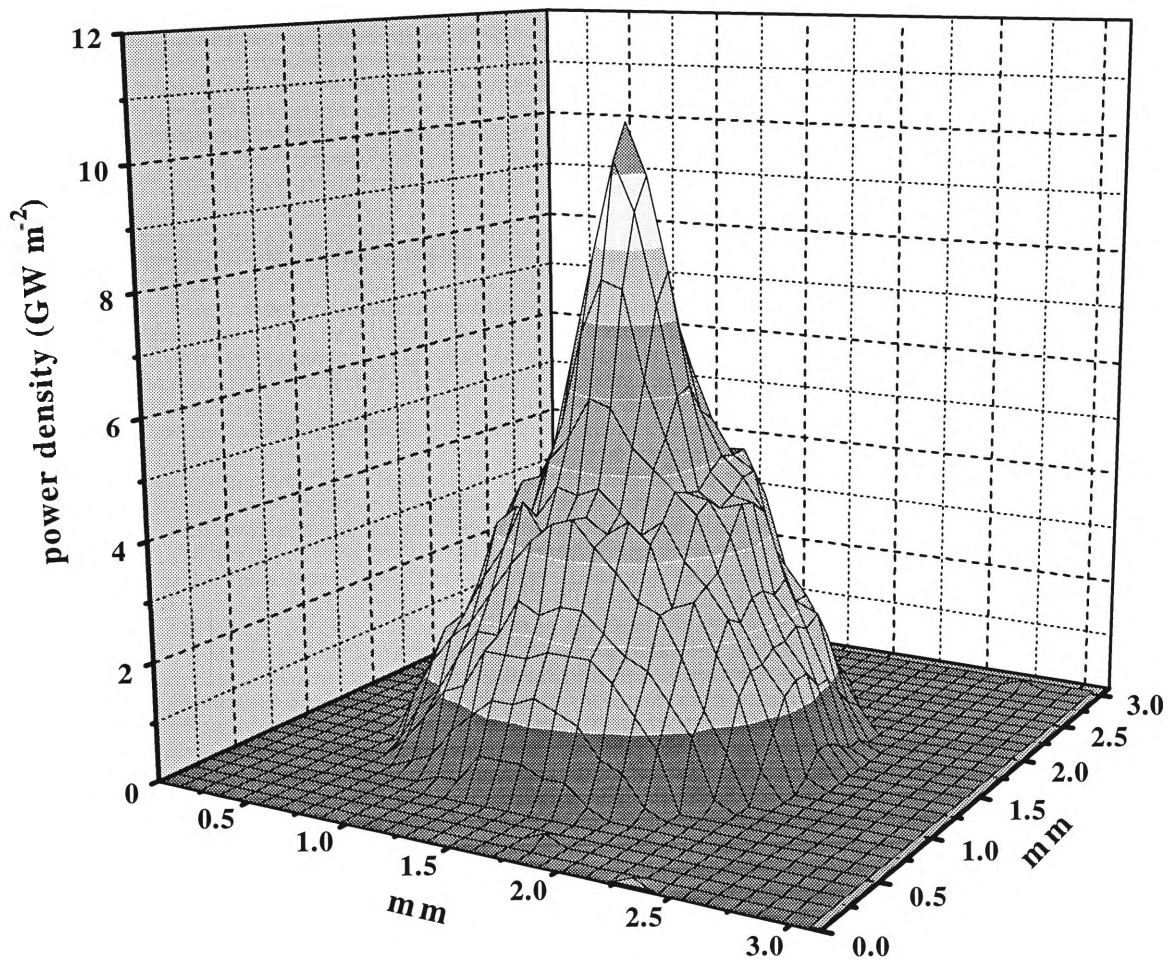

Figure 4.16 Composite intensity profile of tandem Nd:YAG laser beams.
Conditions:

pulse duration = 3 ms
beam 1 - focus 0 mm, 7 J (10 degrees)
beam 2 - focus -5 mm, 7 J (45 degrees)
inter-beam distance = 0 mm

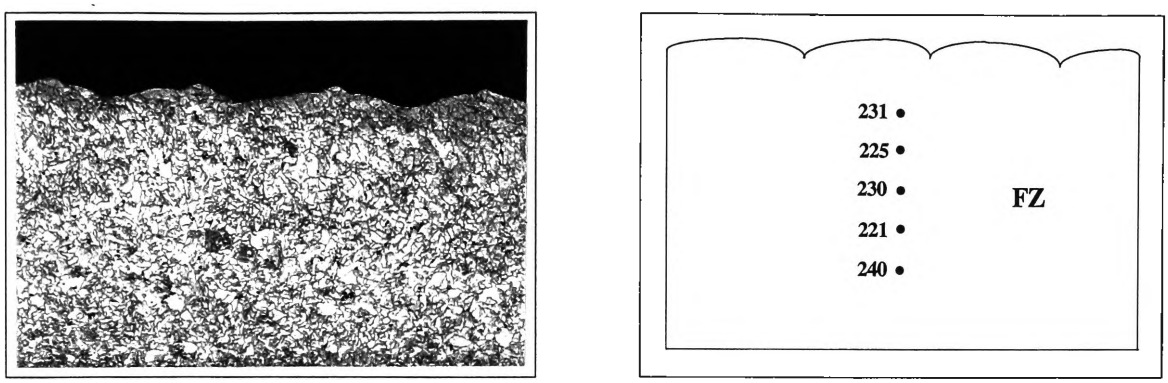

(a) (b)

Figure 4.17 (a) Micrograph (x 60) and (b) schematic hardness profile of a longitudinal section of a tandem-beam weld bead on Zincseal.
Conditions: beam 1 - focus 0, 7 J; beam 2 - focus -5, 7 J; d = 0, 350 mm/min.

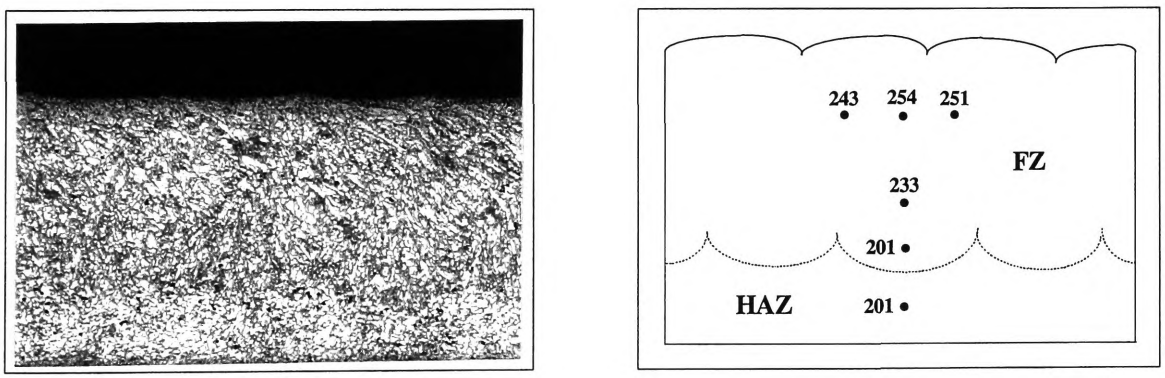

(a) (b)

Figure 4.18 (a) Micrograph (x 60) and (b) schematic hardness profile of a longitudinal section of a single-beam weld bead on Zincseal.
Conditions: 7 J, focus 0 mm, 350 mm/min.

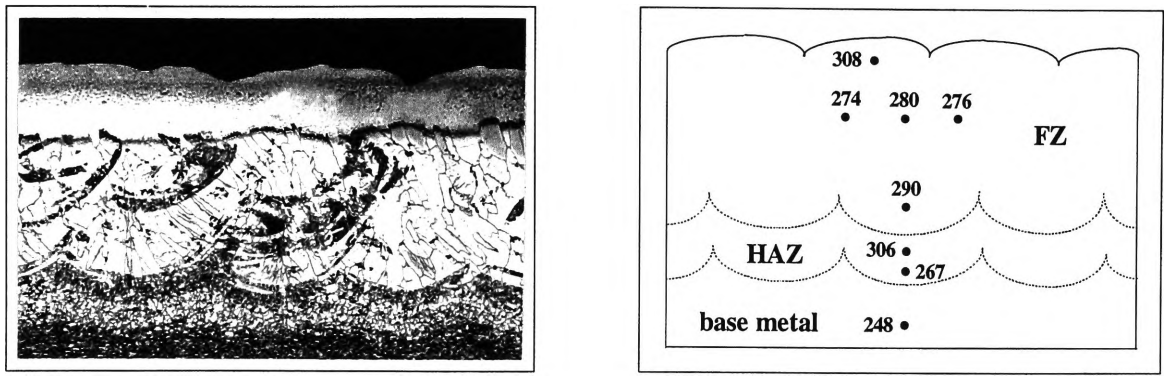

(a) (b)

Figure 4.19 (a) Micrograph (x 60) and (b) schematic hardness profile of a longitudinal section of a tandem-beam weld bead on Zincalume.
Conditions: beam 1 - focus 0, 7 J; beam 2 - focus -5, 7 J; d = 0, 350 mm/min.

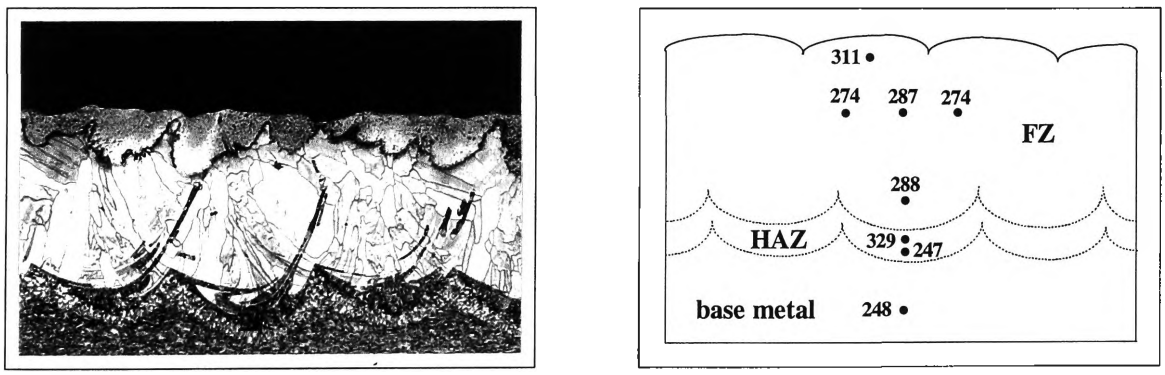

(a) (b)

Figure 4.20 (a) Micrograph (x 60) and (b) schematic hardness profile of a longitudinal section of a single-beam weld bead on Zincalume.
Conditions: 7 J, focus 0 mm, 350 mm/min.

apparent in the tandem-beam weld in which the proportions of aluminium and zinc have been reduced by the second beam. The boundary between the FZ and the HAZ is easily distinguished in each case. The HAZ consists of two subzones: the region next to the FZ boundary contains fine grains of bainitic ferrite and lath martensite, while the intercritical region consists of martensite or martensite-austenite islands within coarse ferrite grains. The higher heat input in the tandem case has resulted in a much wider HAZ for the tandem-beam weld. The cold-rolled and recovered base metal structure (0.1% C) has a much higher hardness (248 HV 0.025) than the spheroidised AISI 1006 steel (125 HV 0.025).

As a result of this preliminary bead-on-plate study, a beam spacing of 0 mm was selected for welding in the butt configuration. By replacing the 50% beam splitter used in the bead-on-plate trials with a 67% beam splitter, the proportion of energy in the main beam was increased. Full penetration for each material could therefore be achieved with minimal melting by the pre-heat beam. Figure 4.21 shows longitudinal sections of single-beam and tandem-beam butt joints for Zincseal, Zincalume and AISI 1006 steel.

4.2.6 Strength, ductility and formability

Tensile testing was used to measure the strength and ductility of both the unwelded and butt welded specimens of each material used in the experiments. The measured values of tensile strength, ductility (%elongation for a gauge length of 25 mm) and reduction in formability are shown in Table 4.1. The base metal strengths and ductilities of the uncoated AISI 1006 steel and Zincseal were similar. For both of these materials failure occurred outside the weld zone for both the single- and tandem-beam butt joints. This is indicated by the same strength and ductility for the unwelded, single- and tandem-welded specimens.

In the case of Zincalume, however, failure occurred within the weld zone for both the single- and tandem-beam specimens, with a strength reduction of approximately 8% in each case. Nevertheless, all of the test results suggest that both welding conditions have produced welds of good quality. Although these results do not demonstrate any

Figure 4.21 Micrographs of the longitudinal sections of the following butt joints:

(a) Zincseal (0.6 mm), single beam, focus 0 mm, 10 J

(b) Zincseal (0.6 mm), tandem beams:

beam 1 - focus 0 mm, 9.4 J

beam 2 - focus -5 mm, 4.6 J

(mag. x 65)

(c) Zincalume (0.85 mm), single beam, focus 0 mm, 13 J

(d) Zincalume (0.85 mm), tandem beams:

beam 1 - focus 0 mm, 12.7 J

beam 2 - focus -5 mm, 6.3 J

(mag. x 30)

(e) AISI 1006 steel (0.9 mm), single beam, focus 0 mm, 14 J

(f) AISI 1006 steel (0.9 mm), tandem beams:

beam 1 - focus 0 mm, 12.7 J

beam 2 - focus -5 mm, 6.3 J

(mag. x 30)

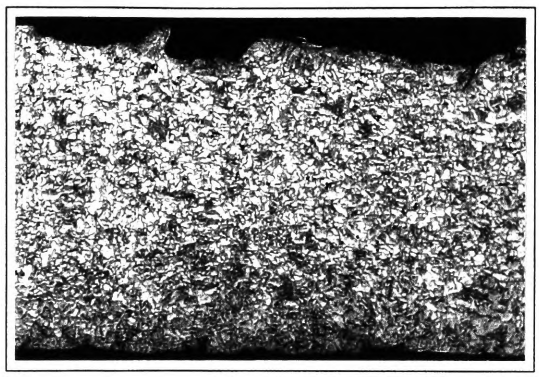

(a)

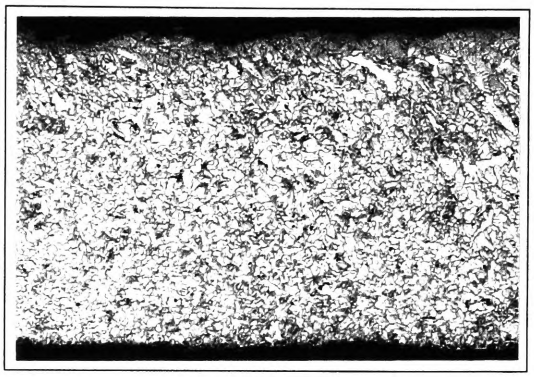

(b)

(c)

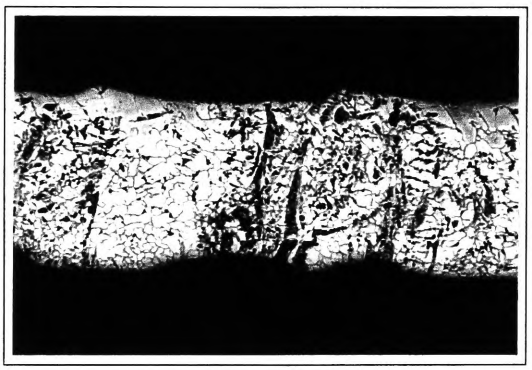

(d)

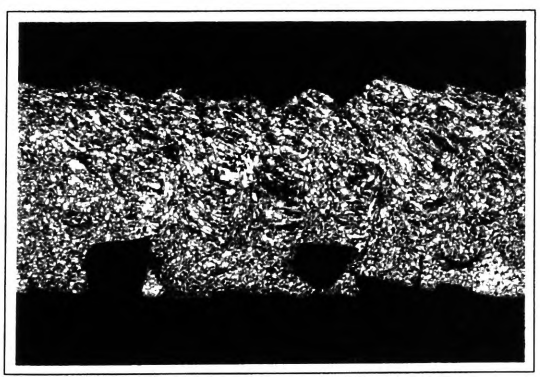

(e)

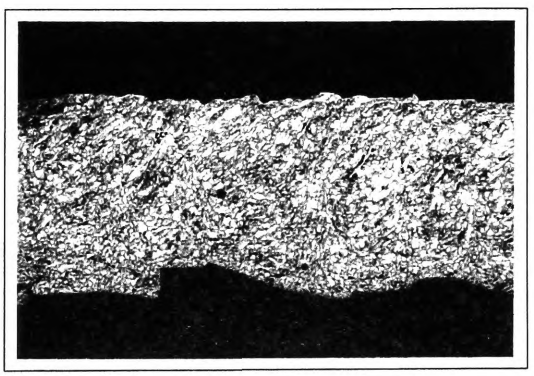

(f)

Material	Unwelded Material		Single-Beam Weld			Tandem-Beam Weld		
	Strength	Ductility	Strength	Ductility	Formability Reduction*	Strength	Ductility	Formability Reduction*
AISI 1006 steel (0.9 mm)	327 MPa	38%	327 MPa	38%	22%	327 MPa	38%	10%
Zincseal (0.6 mm)	353 MPa	41%	353 MPa	41%	22%	353 MPa	41%	14%
Zincalume (0.85 mm)	623 MPa	8%	574 MPa	2%	50%	576 MPa	2%	43%

* Formability reduction represents the %reduction in the Erichsen test dome height for the welded material compared to the unwelded material.

Table 4.1 Mechanical properties (± 5%) of unwelded, single-beam welded and tandem-beam welded AISI 1006 steel, Zincseal and Zincalume. Conditions: as shown in Figure 4.21.

obvious property advantages in employing the tandem-beam technique, the tandem-beam welding conditions selected in this study have produced welds with very smooth surfaces. This compares with the usual undulations in the surfaces of the single-beam welds, which are likely to reduce the fatigue life of the weld. There is even the appearance of pores in the single-beam steel butt joint (Figure 4.21(e)), which is indicative of too high a power density.

In contrast to the results of the tensile tests, all of the tandem-beam butt joints displayed better formability than the single-beam butt joints (Table 4.1). The figures for formability reduction were determined by comparing the dome heights of the unwelded material with those of the welded material. The reduction in the dome height due to the presence of the weld was expressed as a percentage of the "unwelded" dome height. For example, in the case of the AISI 1006 steel, the single-beam weld reduced the dome height by 22% compared with the unwelded material. The tandem-beam butt joint only reduced the dome height by 10% compared with the unwelded material, indicating an improved microstructure. For each of the AISI 1006 steel and Zincseal welds, failure occurred transverse to the weld centre-line. For both of these materials, a significant improvement in the formability of the weld was achieved by employing the tandem-beam technique.

In the case of Zincalume, however, the single-beam weld reduced the formability by 50% compared with the unwelded material. This is, presumably, due to the presence of a large proportion of aluminium in the weld. As discussed in section 4.2.5, tandem-beam welding reduces the residual amount of aluminium in the weld region, but only results in a marginal increase in the formability. The formability tests on Zincalume produced cracks parallel to the weld centre-line under both single- and tandem-beam welding conditions. These cracks appeared within the FZ of each weld.

All of the above results clearly demonstrate that the formabilities of the tandem-beam welds produced in this study are superior to those of the corresponding single-beam welds.

4.3 DISCUSSION

4.3.1 Fusion zone structure

In AISI 1006 steel (0.06% C), the low carbon content would normally be expected to result in solidification to δ-ferrite (Figure 4.22) by cellular growth at the liquid-solid interface where the temperature gradient is very large[127]. The columnar grains of δ-ferrite quickly transform to austenite grains which would also be expected to be columnar in shape and oriented along the prevailing thermal gradient. An alternative possibility is direct solidification to metastable austenite because of the rapid solidification rate expected in laser welding[128]. In either case, elongated austenite grains approximately normal to the fusion boundary are established at high temperatures soon after solidification is complete.

This liquid-solid transition is followed by several solid-state transformations before cooling to ambient temperature. In order to describe the various transformation products, it is necessary to classify the principal microconstituents observed in the as-deposited weld bead. Since the terminology for describing weld metal microstructures can vary considerably, this work has largely adopted the system proposed by the International Institute of Welding (IIW)[129]. Although this system applies to conventional fusion welds, it can be extended to describe the microstructures observed in laser welds.

During cooling of conventional fusion welds, the transformation of the austenite grains depends critically on the cooling rate. For a low-carbon low-alloy steel and typical arc welding heat inputs (0.5 - 2.0 kJ/mm) which correspond to cooling times between 800 °C and 500 °C ($\Delta t_{8/5}$) of about 5 - 30 s, the expected weld metal structure would be as follows: rims of grain boundary (allotriomorphic) ferrite with Widmanstätten side-plates and intragranular acicular and/or bainitic ferrite[130].

The first austenite-to-ferrite transformation product is grain boundary ferrite. As this reaction occurs at relatively high temperatures, generally above 700 °C, grain boundary ferrite formation is mainly diffusion-controlled. Nucleation and growth occur along the prior austenite grain boundaries producing equiaxed or elongated grains of

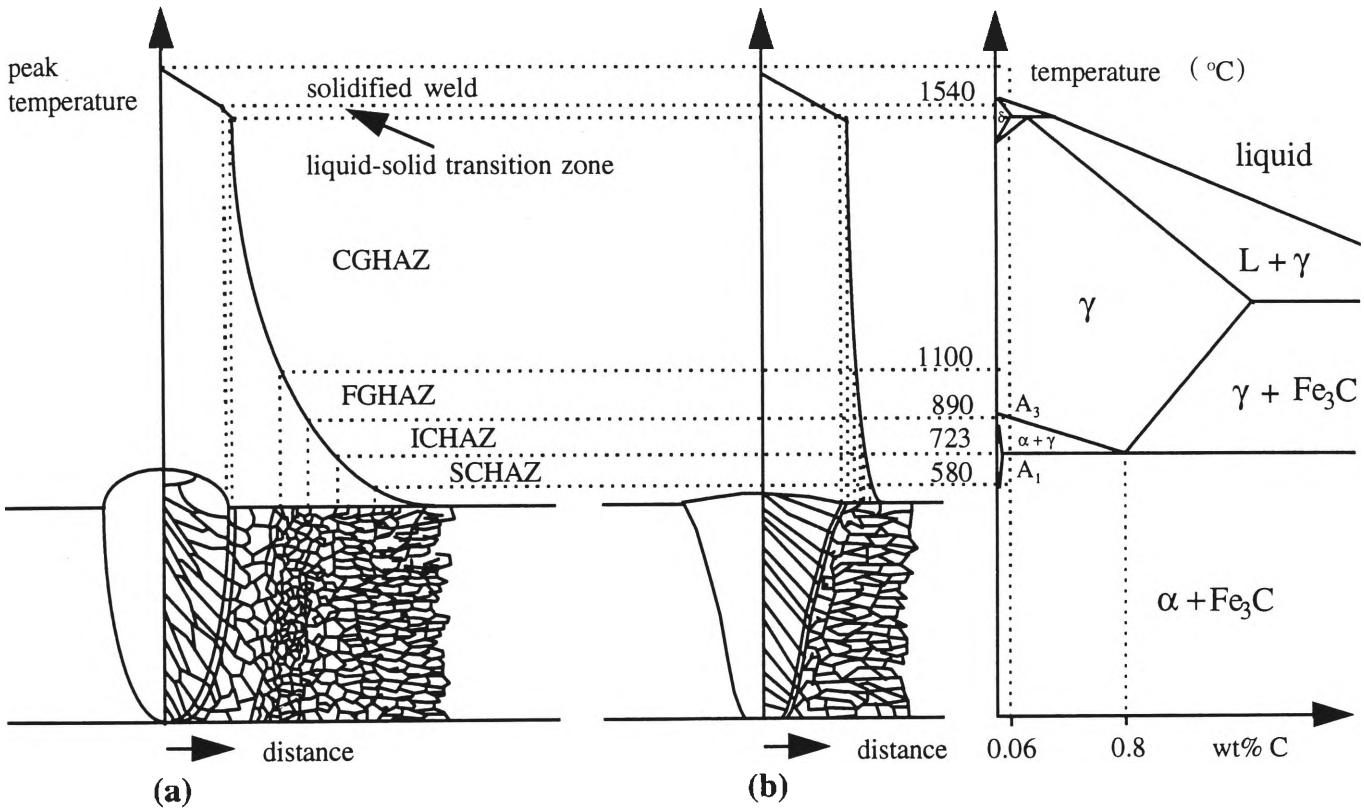

Figure 4.22 Schematic diagrams showing the room temperature structures of the weld metal and the heat-affected zone in a full-penetration butt joint produced by (a) conventional fusion welding, (b) laser beam welding of a low-carbon steel. The structures are related to the peak temperatures reached in the weld thermal cycle and to the Fe-Fe_3C phase diagram. Typical peak temperature-distance curves are shown for each case, together with the resulting subzones in the cooled weldment.

ferrite. At lower temperatures (650 - 700 °C) ferrite growth occurs by the development of semi-coherent interfaces by either displacive transformation or by the migration of incoherent ledges[131], resulting in plate-shaped units. These Widmanstätten plates typically develop as parallel side-plates extending from the allotriomorphic ferrite.

As the temperature of the conventional fusion weld bead drops below 600 °C, intragranular acicular ferrite (AF) may form. These small, multiple-variant ferrite plates have a basket-weave appearance and frequently nucleate at non-metallic inclusions trapped in the weld bead. Competitive formation of packets of bainite plates, usually nucleated at grain boundaries, can also occur.

During austenite decomposition, carbon diffuses from the ferrite to the remaining austenite phase. This carbon diffusion process may be partially suppressed by fast cooling or low transformation temperatures, resulting in the formation of carbon-supersaturated ferrite. The ferrite formed under these conditions is usually plate-shaped, with parallel plate units separated by islands of an aligned second phase. This aggregate is referred to as ferrite with an aligned second phase (FS(A)) by the IIW[129] and as bainitic ferrite, α_B^o, in other reports[130]. For AISI 1006 steel and other low-carbon steels, the aligned second phase is usually in the form of elongated islands of martensite and untransformed austenite. The thickness of the islands decreases and their alignment at ferrite lath and lath packet boundaries becomes more pronounced as the transformation temperature decreases.

For autogenous bead-on-plate (BOP) welds, such as the laser welds in the present work, acicular ferrite is not expected because of the absence of the oxide non-metallic inclusions which nucleate acicular ferrite in arc welds involving filler metals, fluxes or active gases.

In high heat input welds associated with slow cooling rates, the increased diffusion of carbon may allow the formation of the eutectoid mixture of ferrite and cementite lamellae (pearlite). Other types of ferrite-carbide aggregates may also be present.

For a very rapid cooling rate there is a large decrease in the temperature of the austenite-to-ferrite transformation. Consequently, carbon can be completely trapped in a supersaturated solid solution formed by martensitic transformation. The martensite is in the form of packets of body-centred cubic laths in low-carbon steels such as AISI 1006.

The final microstructure of the weld bead is determined by the chemical composition and processing conditions of the weld. Isothermal transformation (IT) diagrams and continuous cooling transformation (CCT) diagrams can be used to describe the resulting phases and microconstituents. An excellent description of CCT diagrams for steels has already been published by Harrison and Farrar[118]. However, the rapid cooling rates associated with laser welding (10^6 °C/s) preclude the use of these CCT diagrams and similar techniques used to describe "slower" cooling rates encountered in conventional fusion welds.

The fusion zone reaches a temperature greater than 1540 °C during welding. In the case of the laser welds presented in this study, the fusion zone typically contains curved columnar grains which have grown epitaxially from the solid/liquid interface in the direction opposite to heat removal. These grains grow toward the centre of the fusion zone and then upward. The transformation products in the FZ appear to be lath martensite (M_L) and/or fine bainitic ferrite (FS(A)) for all of the overlapping and non-overlapping spot welds on AISI 1006 steel. These structures are magnified in Figure 4.3(c). For the tandem-beam overlapping spot welds, an additional region is observed toward the base of the FZ. This results from one or more of the downstream thermal spikes being capable of heating local regions of the FZ into the intercritical region. This leads to partial re-austenitisation of the cast structure. Small patches of dark-etching structure are evident in these cases (Figure 4.23(a)).

In the case of the Zincseal and Zincalume welds, very little lath martensite is observed in the FZ. As zinc and aluminium both produce gamma loops in steel, there is a reduced temperature range over which austenite is stable. These ferrite stabilisers therefore account for the lack of transformation products. The presence of these elements leads to coarse, columnar grains within the FZ for Zincalume (Figure 4.23(b)).

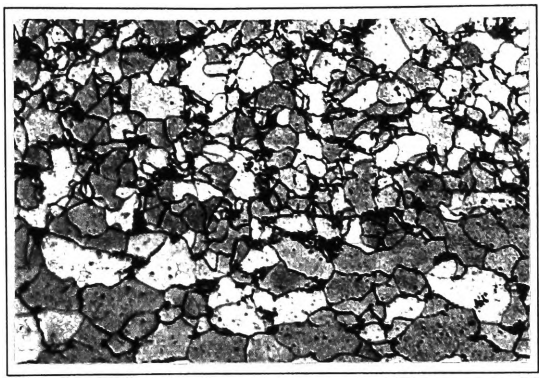

(a)

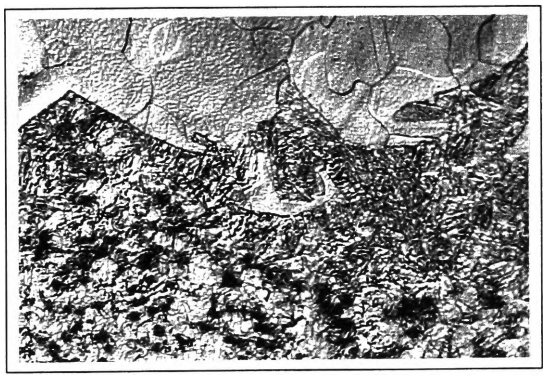

(b)

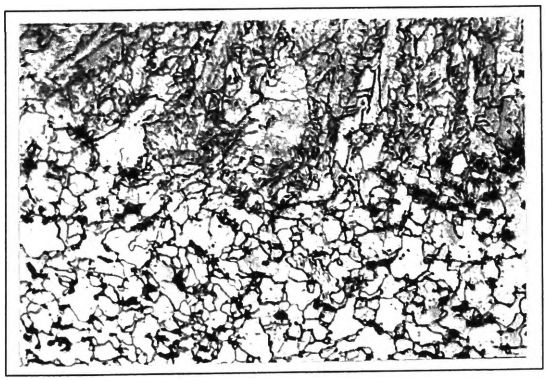

(c)

Figure 4.23 Longitudinal sections of the HAZ of tandem-beam overlapping spot welds on (a) AISI 1006 steel, (b) Zincalume and (c) Zincseal (x 300). Conditions: beam 1 - focus 0, 7 J; beam 2 - focus -5, 7 J; d = +1 mm, 350 mm/min.

Bainitic ferrite is evident in the FZ of the Zincseal welds (Figure 4.23(c)).

The presence of the low-temperature transformation products in the AISI 1006 steel welds indicates that the actual transformation temperature (Ar_3) is well below the equilibrium transformation temperature ($A_3 \approx 890$ °C) identified in Figure 4.22. Although undercooling is also to be expected for a conventional fusion weld, laser welding is associated with a much more rapid cooling rate and consequently the transformation temperature will be lower. Figure 4.22 does not take into account undercooling below the A_3 and A_1 temperatures, but since the undercooling is sensitive to cooling rate, the A_3 temperature is used for convenience in Figure 4.22 and the following discussion.

4.3.2 Heat-affected zone structure

Microstructural analysis of the HAZ of a conventional fusion weld reveals four distinct zones, namely, the coarse-grained zone (CGHAZ), fine-grained zone (FGHAZ), intercritical or partially transformed zone (ICHAZ) and subcritical or tempered zone (SCHAZ)[132]. A schematic diagram of the various zones is shown in Figure 4.22(a). As heat is conducted radially outward from the fusion zone, the base metal immediately adjacent to the fusion boundary is heated high into the austenitic temperature range. The dissolution of the cementite results in rapid grain growth of the austenite grains and the formation of the CGHAZ (1100 - 1540 °C). The maximum grain size and the extent of this grain growth increase as the cooling rate decreases. A typical CGHAZ structure for a low-carbon steel with the arc welding conditions defined in section 4.3.1 would consist of grain boundary ferrite, Widmanstätten side-plate ferrite and ferrite with an aligned second phase (FS(A)).

The next zone encountered on moving radially outward from the FZ is the FGHAZ (890 - 1100 °C). In this region the upper critical or A_3 temperature is exceeded, but the temperature range does not produce significant austenite grain coarsening. The restriction of austenite grain growth results in very fine austenite grains. Subsequent cooling produces a similar microstructure to the CGHAZ, except that the high surface

area of grain boundaries per unit volume (S_v) ensures that grain-boundary nucleated ferrite dominates at the expense of bainitic ferrite.

For peak temperatures between the A_1 and A_3 temperatures, only part of the structure is austenitised (ICHAZ). On cooling, the high-carbon austenite regions can transform to pearlite, bainite, martensite or combinations of these constituents. The untransformed ferrite matrix remains unchanged, except for grain coarsening and dislocation recovery. At temperatures just below the A_1 temperature (580 - 730 °C), coarsening of existing cementite particles and recovery of the dislocation substructure of ferrite can occur (SCHAZ).

In the case of the laser welds examined in this work, optical microscopy tends to show one subregion between the FZ and base metal (Figure 4.3(c)). This subregion is consistent with the partially-transformed or intercritical region (ICHAZ). Both the apparent absence of the other heat-affected subzones observed in conventional fusion welds and the compression of the HAZ indicate that heat has been very rapidly conducted away from the weld bead, as shown schematically in Figure 4.22(b). For the single spot welds on AISI 1006 steel, the width of the HAZ at the bottom of the spot weld ranges from 30 μm (focus 0 mm) to 100 μm (focus -5 mm), as shown in Figure 4.2(b). This difference is due to the variation of the energy density profile with focal position. A decrease in the workpiece speed at constant focus is likely to increase the HAZ width. This effect is confirmed by the micrographs in Figures 4.4(a) and 4.5(a), which show a root HAZ width of 40 μm for speeds of 700 mm/min and 350 mm/min, compared with 30 μm at 3000 mm/min. The laser beam was focussed at the surface in each case.

The overlapping spot welds shown in Figure 4.4(a) (700 mm/min) and Figure 4.5(a) (350 mm/min) have a structure consisting mainly of lath martensite and bainitic ferrite. The re-austenitised as-deposited material has transformed on cooling to plate-shaped ferritic products, thereby making it difficult to distinguish from the as-deposited structure. The increased HAZ and FZ widths for these overlapping spot welds are consistent with the effectively higher heat input due to the much slower welding speed.

These widths are larger for the tandem-beam overlapping spot welds in which the second beam increases the heat input per unit length even further. As a result, the cooling rate is reduced and the peak temperature-distance profile in Figure 4.22(b) becomes less steep.

Figure 4.3(c) indicates the apparent absence of the CGHAZ and FGHAZ despite their association with a temperature range of 1540 °C - 890 °C. This observation can be rationalised in terms of two factors. Firstly, the autogenous nature of the weld means that the fusion line is likely to be difficult to locate. The compositional differences between the weld and the base metal in normal arc welds frequently lead to a sharp definition of the fusion zone through the obvious structural differences. For example, inclusion-stimulated nucleation of acicular ferrite is normally confined to the weld metal and is not a structural feature of the CGHAZ of the base steel, except for the case of oxide-inoculated steels[133]. Likewise, there is no difficulty in locating the FZ boundary for the Zincalume welds shown in Figures 4.19 and 4.20. The presence of aluminium, and to a much smaller extent zinc, in the FZ of each weld has resulted in the growth of coarse ferritic grains from the FZ-HAZ interface. A distinguishing line separating the FZ from the CGHAZ, which consists of lath martensite and bainitic ferrite, is evident in these cases.

Secondly, the very fast cooling rates in the laser welds compress the distance range over which the base metal reaches peak temperatures in the range 1540 - 890 °C. Therefore, the CGHAZ and the FGHAZ are both narrow and difficult to distinguish from the weld zone. The weld metal structure develops by epitaxial growth from the delta ferrite grains in the CGHAZ adjacent to the fusion zone. Delta ferrite rapidly transforms to austenite which then undergoes solid-state transformation to ferritic products on cooling of the CGHAZ. A schematic peak temperature versus distance curve consistent with the production of the observed HAZ structure is shown in Figure 4.22(b).

The ICHAZ observed in the various laser welds results from the material in this region being heated between the A_1 and A_3 temperatures. This results in a two-phase solid solution of austenite and proeutectoid ferrite. On subsequent rapid cooling, the austenite transforms to martensite. Austenite can also be retained, particularly in steels

containing a high Mn content and other austenite stabilisers such as Ni and Cu[134]. Martensite or martensite-austenite (M-A) islands in a ferrite matrix are evident in this region (Figure 4.23). The elongation of the M-A islands parallel to the sheet rolling direction is consistent with the localised dissolution of groups of carbide particles aligned in the rolling direction. These high-carbon regions have a low austenite transformation temperature (Ar_3). They re-austenitise first on reheating, resulting in elongated carbon-rich austenite islands which transform to martensite on rapid cooling.

Although this microstructure was characteristic of a majority of the HAZs observed in this work, regions in the upper areas of some weld beads exhibited very small coarse-grained and fine-grained zones. The CGHAZ and FGHAZ contained similar microconstituents to those observed in the adjacent FZ, namely lath martensite and bainitic ferrite. These regions were very apparent in the Zincalume welds.

CHAPTER 5

NUMERICAL AND ANALYTICAL MODELS OF PULSED LASER WELDING

5.1 INTRODUCTION

The literature survey presented in Chapter 2 revealed that there have been several numerical and analytical models which have sought to elucidate the physical mechanisms involved in the continuous-wave laser welding process. However, there exist few models of pulsed laser welding. The main reason for this apparent scarcity lies in the complexity of the laser-material interaction process. This complexity implies that analytical modelling techniques are almost impossible. The numerical model is therefore the preferred option, although the analysis requires a very large number of small time steps, much smaller than those needed for the continuous analysis.

Simplifying assumptions are often made in numerical modelling in order to reduce computer modelling time. In laser welding, the most significant heat transfer mechanisms are heat input from the laser beam and heat loss due to conduction from the weld pool. Convection in the weld pool is often approximated by using an artificially high value of the thermal conductivity, with anisotropic conductivities used in some cases. Alternatively, the highly non-linear approach is to simultaneously solve the continuum equations for conservation of mass, energy and momentum. This method, however, requires an accurate knowledge of the temperature dependence of material properties such as density, thermal conductivity, specific heat, surface tension and viscosity. Since the availability of data at high temperatures is limited, so-called "effective" material properties are often used.

The approach here was to utilise the efficient parametric design capabilities and solution procedures of the finite element code ANSYS on a SGI Challenge L Series workstation. Owing to the complexity of the pulsed laser welding process, this program was customised in order to solve just the energy balance equation with appropriate initial and boundary conditions. Only the bead-on-plate welding configuration was considered. The method employed uses realistic temperature-dependent variables, experimentally measured laser beam intensity distributions as described in section 3.3.2, and requires only one "calibration" factor to match model predictions with experiment for a wide range of conditions. As discussed in section 2.5.3, pulsed laser welding involves very rapid melting and solidification (rather than a "permanent" weld pool), convective

dissipation of heat in the weld pool is likely to be minimal and may be neglected.

Physical and mathematical descriptions of the numerical models of single- and tandem-beam pulsed laser welding are presented in section 5.2. Each model was assessed by comparing model predictions with experimental results. AISI 1006 steel was used for this purpose. In order to test the capabilities of the model on a different material, A5005 aluminium was chosen to perform comparisons between experiment and theory for a select set of conditions, namely, non-overlapping single spot welds.

Furthermore, in order to check the solution procedures incorporated into the numerical models, it was necessary to develop simple and quick analytical models of both single- and tandem-beam pulsed laser welding. However, owing to the difficulty in analytically modelling the formation, growth and collapse of a series of plasma-filled keyholes, only the laser conditions which resulted in conduction-limited welds could be considered. Nevertheless, these analytical models provide a very powerful means of establishing the accuracy of the numerical approach employed in this study.

The analytical models for the temperature rise due to laser welding with one or two beams are presented in section 5.3. Weld pool convective flow, as well as convection and radiation to surroundings, are neglected. A full derivation of both models is presented in Appendix B. Each model was developed by first considering Rosenthal's instantaneous point source solution. The instantaneous Gaussian source solution was then established by realising that the Gaussian source consists of an infinite number of point sources, each contributing to the temperature rise at some point P(x,y,z) in the plate. Integration with respect to the surface of the plate permitted the summation of all point source contributions. By incorporating a velocity term and then integrating with respect to time, the model was extended to simulate a moving, continuous heat source. The case of single-beam pulsed laser welding was then established by selecting appropriate limits of integration. Vishnu *et al.*[91] have employed a similar method for gas-tungsten arc welding. Finally, by summing the contributions from two separate heat sources, the temperature rise due to tandem laser welding was obtained.

5.2 NUMERICAL MODELS

5.2.1 Physical description

A moving, pulsed laser beam with an experimentally determined energy distribution strikes the surface of a finite three-dimensional AISI 1006 steel plate. The power density is sufficient to form a series of non-overlapping or overlapping bead-on-plate laser welds. The dimensions of the plate and heat source are shown in Figure 5.1(a). When a second beam is present in tandem with the first beam, the beams are separated by a distance d, as shown in Figure 5.1(b).

The numerical modelling of heat transfer during the welding of materials by laser radiation is complicated because of the rapid changes in the temperature and phase of the workpiece, the largely unknown interactions which occur between the incoming laser beam and the laser-produced plasma, and the difficulty of accurate determination of the temperature dependence of materials at high temperatures. The major contributions to this area of research were described in Chapter 2. The present work examined many different techniques, including the discrete addition and subtraction of nodal points to simulate the movement of the workpiece, the implicit inclusion of latent heat by means of the material property enthalpy, the deactivation of elements to model the removal of material, and the application of internal "body force" loads to model the absorption of radiation within the plasma. The procedure found to give consistent results with experimental data is described in (3) below.

The following assumptions were made in the formulation of both the single- and tandem-beam finite element models:

(1) The first laser beam is stationary and incident at an angle θ on the centre-line of the workpiece. When a second beam is present, this beam is stationary at an angle ϕ such that $\phi > \theta$ (Figure 5.1(b)). The projection of these approximately circular laser beams on to a plane surface at an angle results in elliptical processing beams, with the major axes in the direction of welding. Angled irradiation increases the cross-sectional area of the beam and therefore decreases the power density.

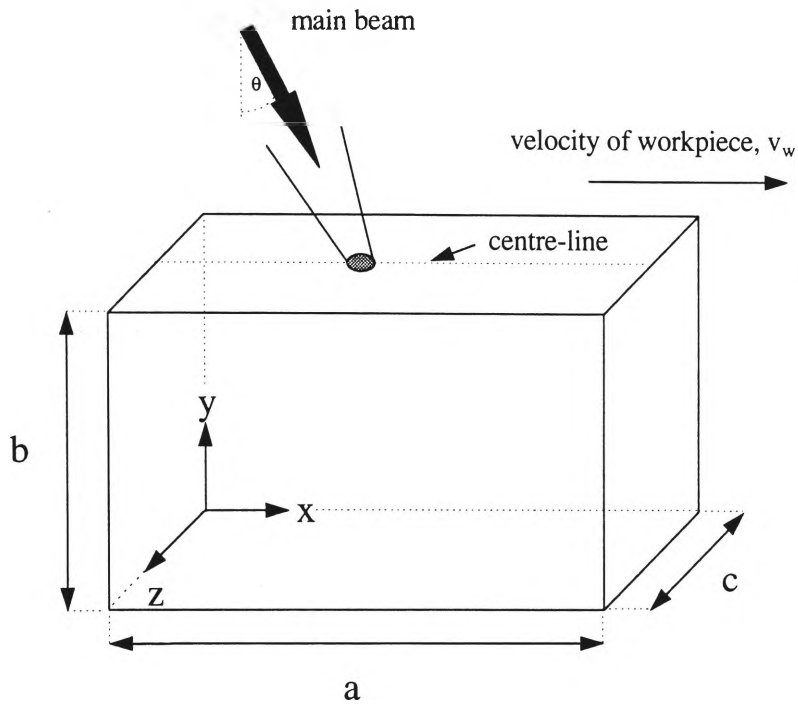

(a)

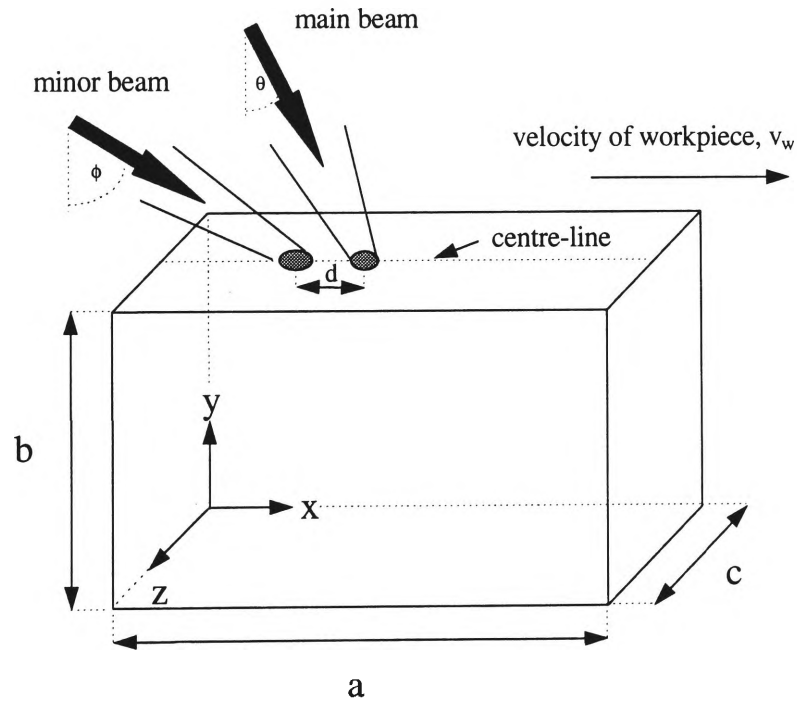

(b)

Figure 5.1 Finite plate heated by (a) one beam and (b) two laser beams in tandem. The minor beam is shown as pre-heating the workpiece.

(2) The workpiece is initially at 20 °C and moves in the positive x-direction with a constant velocity, v_w.

(3) A proportion of the incident radiation is reflected and the rest is absorbed by the workpiece, as determined by the "effective absorptivity". This parameter was determined by matching model outcomes with experimental data. It was found to be typically 30% ± 5% for AISI 1006 steel and 12% ± 2% for A5005 aluminium alloy (see section 5.6.2). When the temperature of the material exceeds the boiling point, a certain amount of radiation is assumed to be absorbed by the vapour and/or plasma, while the rest is transmitted through the plasma with an absorption rate determined by Beer-Lambert's law. The proportion reaching the walls of the keyhole is fully absorbed by the material. The proportions of radiation absorbed within the plasma by an Inverse Bremsstrahlung mechanism and transmitted through the plasma were determined to be 70% and 30%, respectively. Again these figures were determined by comparison with experimental results: for a plasma absorption higher than 70%, vaporisation was not maintained and the keyhole collapsed; for lower absorptivities, boiling was too rapid and the resulting weld pool was too deep and too wide. The 30% of transmitted radiation was attenuated according to Beer-Lambert's law:

$$P = P' \exp(-\alpha L), \qquad (5.1)$$

where α is the absorption coefficient (m^{-1}) and is considered to be independent of position within the keyhole. For low-carbon steel, Mazumder and Steen[81] suggest an absorption coefficient of 800 m^{-1}. P is the beam power reaching a depth L, and P' is the incident power. For A5005 aluminium alloy, it is assumed that there is negligible attenuation of the laser beam. Even for a fully ionised Al plasma at 10 000 K, the total intensity absorbed by the plasma does not exceed 2%[135]. Although the assumed proportions of radiation absorbed at the walls of the keyhole represent a very simple approximation to a very complex interaction process involving multiple reflections and re-absorption, this approximation appears to work very well.

(4) When the temperature of a node exceeds the boiling point, it remains in the mesh at a fictitiously high temperature to simulate the presence of a plasma-filled keyhole. This approach is similar to the one adopted by Mazumder and Steen.

(5) All thermophysical properties for AISI 1006 steel are considered to be dependent on temperature. These properties are shown in Table 5.1: thermal conductivity, specific heat and emissivity according to Brown and Song[136], and density according to Kim[137]. Owing to the lack of high-temperature data for A5005 aluminium alloy, the thermophysical properties of the alloy are considered to be constant (Table 5.2)[138].

(6) For AISI 1006 steel, the latent heat of fusion is simulated by an artificial increase in the liquid specific heat according to Brown and Song. For A5005 alloy, the latent heat of fusion is not considered.

(7) As pulsed laser welding involves very rapid melting and solidification, convective dissipation of heat within the weld pool is not as significant as it is in other processes where a liquid pool is permanent. Convective flow of heat is therefore neglected.

5.2.2 Mathematical description

The spatial and temporal temperature distribution T(x,y,z,t) satisfies the following differential equation for three-dimensional heat conduction in a domain D:

$$\frac{\partial}{\partial x}\left(k_x \frac{\partial T}{\partial x}\right) + \frac{\partial}{\partial y}\left(k_y \frac{\partial T}{\partial y}\right) + \frac{\partial}{\partial z}\left(k_z \frac{\partial T}{\partial z}\right) + q = \rho c \left(\frac{\partial T}{\partial t} - v_w \frac{\partial T}{\partial x}\right). \tag{5.2}$$

Equation 5.2 represents the basis of both the numerical and analytical models of the pulsed laser welding process. For this reason, it has been derived in Appendix A.

Temperature (deg. C)	Thermal Conductivity ($W\ m^{-1}\ K^{-1}$)	Specific Heat ($J\ kg^{-1}\ K^{-1}$)	Emissivity	Density ($kg\ m^{-3}$)
0	51.9	450	0.2	7872
75	51.3	486	0.35	7852
100	51.1	494	0.4	7845
175	49.5	519	0.44	7824
200	49	526	0.45	7816
225	48.3	532	0.46	7809
275	46.8	557	0.47	7763
300	46.1	566	0.48	7740
325	45.3	574	0.48	7717
375	43.6	599	0.5	7727
400	42.7	615	0.51	7733
475	40.2	662	0.53	7720
500	39.4	684	0.54	7711
575	36.6	749	0.55	7680
600	35.6	773	0.56	7669
675	32.8	846	0.57	7636
700	31.8	1139	0.57	7625
730	30.1	1384	0.58	7612
750	28.9	1191	0.58	7602
775	27.5	950	0.58	7590
800	26	931	0.58	7578
1000	27.2	779	0.59	7552
1500	29.7	400	0.6	7268
1540	29.7	400	0.6	7218
1590	29.7	847	0.6	7055
1840	29.7	847	0.6	6757
1890	29.7	400	0.6	6715
2860	29.7	400	0.62	5902

Table 5.1 Thermophysical properties of AISI 1006 steel used in the finite element models. These properties are linearly interpolated for the intermediate temperatures.

Temperature (deg. C)	Thermal Conductivity ($W\ m^{-1}\ K^{-1}$)	Specific Heat ($J\ kg^{-1}\ K^{-1}$)	Density ($kg\ m^{-3}$)
20	201	962	2685

Table 5.2 Thermophysical properties of A5005 aluminium alloy used in the finite element models.

Each symbol is defined as follows:

(x,y,z) = coordinate system attached to the heat source(s),

q = power generated per unit volume in the domain D ($W\ m^{-3}$),

k_x, k_y, k_z = thermal conductivity in the x, y and z directions ($W\ m^{-1}\ K^{-1}$),

c = specific heat capacity ($J\ kg^{-1}\ K^{-1}$),

ρ = density ($kg\ m^{-3}$),

t = time (s),

v_w = velocity of workpiece ($m\ s^{-1}$).

The initial condition is:

$$T(x,y,z,0) = T_0, \text{ for } (x,y,z) \in D. \tag{5.3}$$

The essential (or Dirichlet) boundary condition is:

$$T(0,y,z,t) = T_0, \tag{5.4}$$

on the boundary S_1 for $(y,z) \in S_1$ and $t > 0$.

This condition prescribes nodal temperatures at the flow inlet. S_1 represents the inlet surface.

The natural (or Neumann) boundary conditions can be defined by:

$$k_n \frac{\partial T}{\partial n} - q_b + h(T - T_0) + \sigma_{SB} \varepsilon (T^4 - T_0^4) = 0, \tag{5.5}$$

on the boundary S_2 for $(x,y,z) \in S_2$ and $t > 0$.

S_2 represents those surfaces which are subject to radiation, convection and imposed heat fluxes. A special case of the imposed heat flux is the adiabatic condition, which represents insulated or symmetry surfaces. The symbols are defined as follows:

k_n = thermal conductivity normal to S_2 (W m^{-1} K^{-1}),

h = heat transfer coefficient for convection (W m^{-2} K^{-1}),

σ_{SB} = Stefan-Boltzmann constant for radiation (5.67 x 10^{-8} W m^{-2} K^{-4}),

ε = emissivity,

T_0 = ambient temperature = 293 K; and

$$q_b = \delta q_e, \tag{5.6}$$

where:

q_e = experimentally determined heat flux normal to S_2 (W m^{-2}),

δ = 1 (for pulse on),

δ = 0 (for pulse off).

The inclusion of temperature-dependent thermophysical properties and a radiation term in the above boundary condition makes this type of analysis highly non-linear. Since the incorporation of radiation effects was found to increase solution times by as much as three times, Vinokurov's empirical relationship for welding hot-rolled steel plates was used for AISI 1006 steel[139]:

$$h = 2.4 \times 10^{-3} \varepsilon T^{1.61}. \tag{5.7}$$

Equation 5.7 combines the effects of radiation and convection into a "lumped" heat transfer coefficient. The associated loss in accuracy is estimated to be less than 5% for the conditions selected in this study. For the single A5005 spot welds modelled in the present study, convection and radiation effects were not considered.

5.2.3 Finite element analysis

The finite element code ANSYS (Revision 5.2) provides a convenient way of numerically modelling pulsed laser welding. A system with an infinite number of unknowns (the response at every location in the system) can be transformed into one that

has a finite number of unknowns related to each other by elements of finite size. These elements connect at their nodes to form a mesh which simulates the geometrical form required. Elements are usually in the form of beams, plates, shells or three-dimensional bricks. Appropriate thermal loads are then applied. These loads can be in the form of discrete point loads at nodes, line loads along beams or plate edges, or surface loads on plate or brick element faces.

An example of the mesh employed for the single laser beam conditions employed in this study is shown in Figure 5.2. The mesh was linearly graded from fine to coarse according to the expected reduction in temperature gradient on moving away from the heat source. As all the measured laser beam profiles were symmetric or near-symmetric about the weld centre-line, only half of each beam profile was considered. The symmetry boundary is shown in Figure 5.2. The fine section of the mesh was increased in size to accommodate the presence of two heat sources. An error estimation technique based on the discontinuity of the heat flux between elements was employed to achieve a calculation accuracy of $\pm 5\%$. As a result, the meshes selected in this study provided an optimum balance between solution time and accuracy. Furthermore, the cost-effective choice of three-dimensional brick elements provided the simplest means of applying experimentally determined beam profiles.

After applying initial and boundary conditions, a transient thermal analysis was performed for each set of conditions. This required an integration of the heat conduction equation with respect to time. In the finite element formulation, this equation can be written for each element as:

$$[C(T)]\{\dot{T}\} + [K(T)]\{T\} + \{V\} = \{Q(T)\}, \tag{5.8}$$

where:

$[K]$ = conductivity matrix,

$[C]$ = specific heat (or capacitance) matrix,

$\{T\}$ = nodal temperatures,

$\{\dot{T}\}$ = time derivative of $\{T\}$,

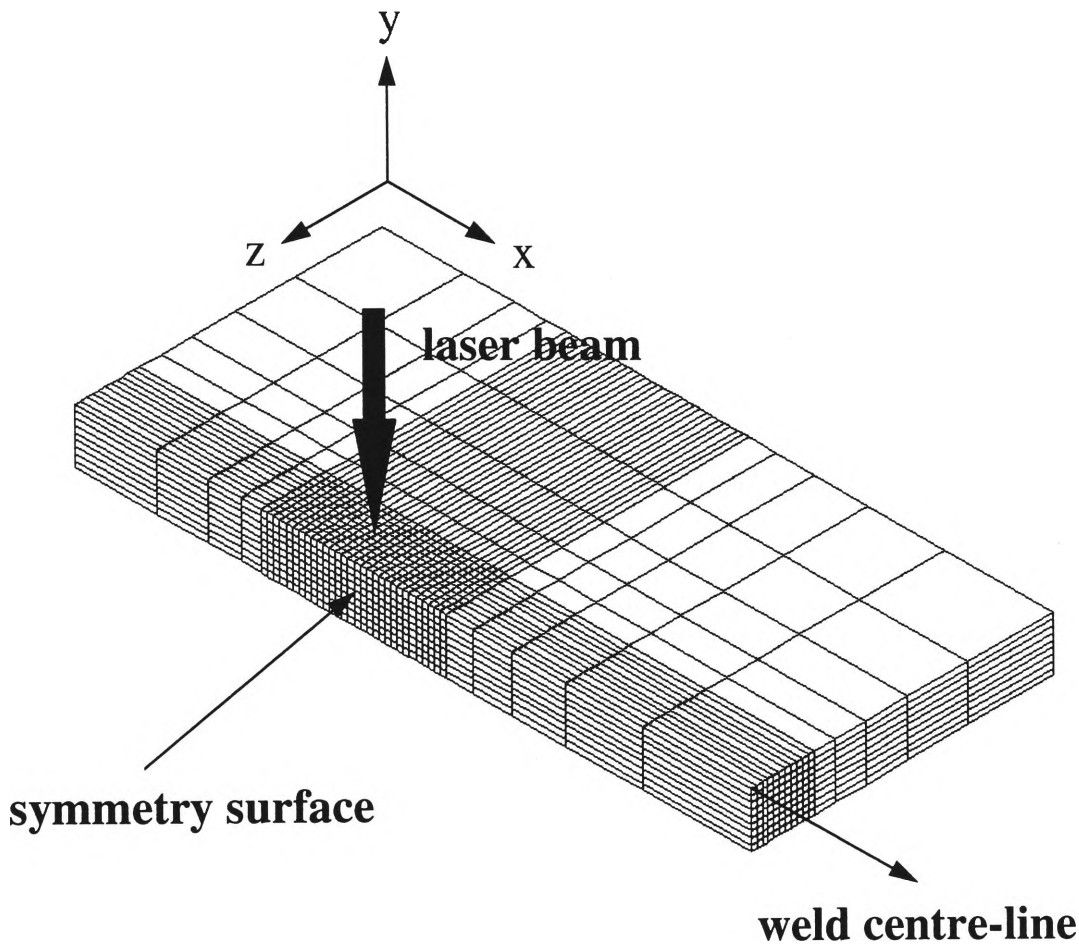

Figure 5.2 11 mm x 0.9 mm x 5 mm finite element mesh consisting of 5 616 eight-noded elements. Each element in the fine section of the mesh has a volume of 0.1 mm x 0.1 mm x 0.1 mm.

$\{V\}$ = velocity vector for the moving workpiece,

$\{Q\}$ = nodal heat flow vector.

Standard variational techniques were then applied in order to solve these system equations. This was accomplished through the Crank-Nicholson/Euler theta integration method, in which the equations were solved at discrete time points within the transient[140]. The automatic time-stepping feature of the ANSYS program was employed to automatically increase or decrease the difference between time points, commonly termed integration time step, based upon response conditions.

The first iteration in the solution procedure solved the system equations at an assumed starting temperature of 20 °C, and subsequent iterations used temperatures from previous iterations to calculate the thermal conductivity and specific heat matrices. The iterative process continued until a converged solution for each set of conditions was achieved; that is, when user-defined convergence criteria were met. Convergence checking was based on the out-of-balance heat flow vector and the temperature increment from one iteration to the next.

The solution data was in the form of nodal temperatures. This data was used in the post-processing phase to produce displays of temperature contours (isotherms). Other post-processing options were also available to extract more specific information, such as the thermal gradient and thermal flux at nodes and element centroids.

It should be emphasised that the ANSYS program was customised to treat the very complex issue of a very rapidly pulsing heat source. The parametric design capabilities of the program were extended for this purpose. An innovative technique was also implemented to store and transfer the large amounts of data produced by the model. Without these modifications the problem would not have been solved as easily. This is the first time that anyone has performed this type of analysis with reasonable success.

5.3 ANALYTICAL MODELS

5.3.1 Single-beam welding

Consider a semi-infinite plate which is being heated by a pulsed Gaussian heat source moving in the positive x-direction with a velocity v. Let the heat source have a peak power $\dot{q}$ and a beam distribution parameter σ. At time t = 0, the centre of the heat source is at (0,0,0). The temperature rise at a point P(x,y,z) in the plate can be described by:

$$\Delta T = \frac{\dot{q}}{2\pi k\sqrt{\pi\alpha t_0}} \exp\left(-\frac{v\xi}{2\alpha} - \frac{v^2 t_0}{4\alpha}\right) \sum_{n=1}^{n_{tot}} \int_{a_n}^{b_n} \frac{d\eta}{1+\eta^2} \exp\left(-\frac{M}{\eta^2+1} - \frac{N}{\eta^2} - P\eta^2\right) \tag{5.9}$$

Definitions of the symbols in Equation 5.9 can be found in Appendix B. The expressions for the integral limits a_n and b_n in terms of pulse number (n), pulse duration (t_p) and repetition rate (f) are:

$t \le (n-1)/f$:	$a_n = 0$ $b_n = 0$
$(n-1)/f < t \le t_p + (n-1)/f$:	$a_n = 0$ $b_n = \sqrt{\frac{t-(n-1)/f}{t_0}}$
$t > t_p + (n-1)/f$:	$a_n = \sqrt{\frac{t-t_p-(n-1)/f}{t_0}}$ $b_n = \sqrt{\frac{t-(n-1)/f}{t_0}}$

A Fortran program was written to perform the numerical integration in Equation 5.9 between the above limits.

5.3.2 Tandem-beam welding

Consider two moving, pulsed Gaussian heat sources which are separated by a distance d. Let the first heat source have a peak power $\dot{q}_1$ and a beam distribution parameter σ_1. At time t = 0, the centre of the first heat source is at (0,0,0). Let the second heat source have a peak power $\dot{q}_2$ and a beam distribution parameter σ_2. At time t = 0, the centre of the second heat source is at (d,0,0). Both heat sources are synchronised and move in the positive x-direction with a velocity v. The temperature rise at a point P(x,y,z) can be given by:

$$\Delta T = \sum_{m=1}^{2} \frac{\dot{q}_m}{2\pi k\sqrt{\pi\alpha t_m}} \exp\left(-\frac{v\xi_m}{2\alpha} - \frac{v^2 t_m}{4\alpha}\right) \sum_{n=1}^{n_{tot}} \int_{a_{nm}}^{b_{nm}} \frac{d\eta_m}{1+\eta_m^2} \exp\left(-\frac{M_m}{\eta_m^2+1} - \frac{N_m}{\eta_m^2} - P_m\eta_m^2\right) \tag{5.10}$$

Definitions of all symbols are provided in Appendix B. The Fortran program for single-beam laser welding was extended to perform the numerical integration in Equation 5.10.

5.4 COMPARISON BETWEEN EXPERIMENT AND THEORY

The results of the ANSYS program can be displayed in many ways. Since the program is capable of calculating the temperature at any nodal point in the material as a function of time, different modes of presentation of the results need to be selected in order to assess the ability of the model to predict experimentally measurable quantities. This comparison of experiment with theory, and the consequent modification of the various parameters which represent physical processes in the model, may allow the estimation of the relative importance and role of the complex physical interactions which govern pulsed laser welding.

As outlined in section 3.3, the numerical models of single- and tandem-beam pulsed laser welding were employed to simulate various welding conditions. A summary of these conditions is presented in Table 5.3.

Arrangement	Speed (mm/min)	Main Beam Energy and Focal Position	Minor Beam Energy and Focal Position	Inter-Beam Distance (mm)
(a) Single-beam non-overlapping spot welds on AISI 1006 steel	3000	7 J, -5 to +5 mm (1 mm incs)		
	3000	3 J - 11 J (2 J incs), 0 mm		
(b) Single-beam overlapping spot welds on AISI 1006 steel	700	7 J, focus 0 mm		
	350	7 J, focus 0 mm		
(c) Tandem-beam non-overlapping spot welds on AISI 1006 steel	3000	7 J, 0 mm	7 J, -5 mm	-1 to +1 (0.2 mm incs)
	3000	7 J, 0 mm	7 J, 0 mm	-1 to +1 (0.2 mm incs)
(d) Tandem-beam overlapping spot welds on AISI 1006 steel	350	7 J, 0 mm	7 J, -5 mm	-1, 0, +1
	350	2 J, 0 mm	2 J, 0 mm	-1, 0, +1
	350	1 J, 0 mm	1 J, 0 mm	-1, 0, +1
(e) Single-beam non-overlapping spot welds on A5005 alloy	3000	20 J, -5 to +5 mm (1 mm incs)		
	3000	18 J, 0 mm and -1 mm		

Table 5.3 Summary of numerical modelling conditions.

A pulse duration of 3 ms and a repetition rate of 20 Hz were used in all cases.

In order to provide a quick check of the numerical models of single- and tandem beam pulsed laser welding, the analytical models presented in section 5.3 were employed for a select set of conditions. Both AISI 1006 steel and A5005 aluminium alloy were chosen for this analysis. The selected conditions are shown in Table 5.4. As the intensity distribution of the laser beam is strongly dependent on the focal position of the beam relative to the surface of the workpiece, it was necessary to select a focal position which provided a profile closely resembling a Gaussian distribution. Focussing the laser beam at the surface of the workpiece satisfied this criterion. The beam profile was obtained by means of a Spiricon laser beam analyser (see section 3.3.1) and then approximated by a Gaussian distribution.

5.5 RESULTS

5.5.1 Single-beam non-overlapping spot welds

The model was run for both the duration of a single laser pulse and the subsequent cooling period. From this data the positions of the 1540 °C and 730 °C isotherms were determined. Given the highly non-equilibrium conditions associated with pulsed laser welding, these contours approximately represent the fusion zone (FZ) and weld zone (WZ) boundaries, respectively. The temperature of each nodal point within the solid was calculated as a function of time. For each set of conditions, the maximum depth and diameter of the 1540 °C and 730 °C temperature contours were measured.

A micrograph of the cross-section of one of the actual spot welds (focus 0 mm) is shown in Figure 4.3(a). From such a micrograph the depth and diameter of the FZ and WZ were measured. Just as this laser spot weld was physically sectioned, a section through the centre-line of the model can be taken. ANSYS model predictions of the FZ and WZ boundaries were superimposed on this micrograph, as shown in Figure 5.3. The asymmetry of the weld bead is due to the angle of the beam. The FZ and WZ isotherms shown in this figure represent the positions which have been heated to maximum temperatures of 1540 °C and 730 °C, respectively. Owing to the unusual donut shape of the "-5" spot weld, a micrograph of the longitudinal section of this spot weld is shown in

Arrangement	Speed (mm/min)	Main Beam Energy and Focal Position	Minor Beam Energy and Focal Position	Inter-Beam Distance (mm)
(a) Tandem-beam overlapping spot welds on AISI 1006 steel	350	2 J, 0 mm	2 J, 0 mm	-1, 0, +1
	350	1 J, 0 mm	1 J, 0 mm	-1, 0, +1
(b) Single-beam non-overlapping spot welds on A5005 alloy	3000	18 J, 0 mm		

Table 5.4 Summary of analytical modelling conditions.

A pulse duration of 3 ms and a repetition rate of 20 Hz were used in all cases.

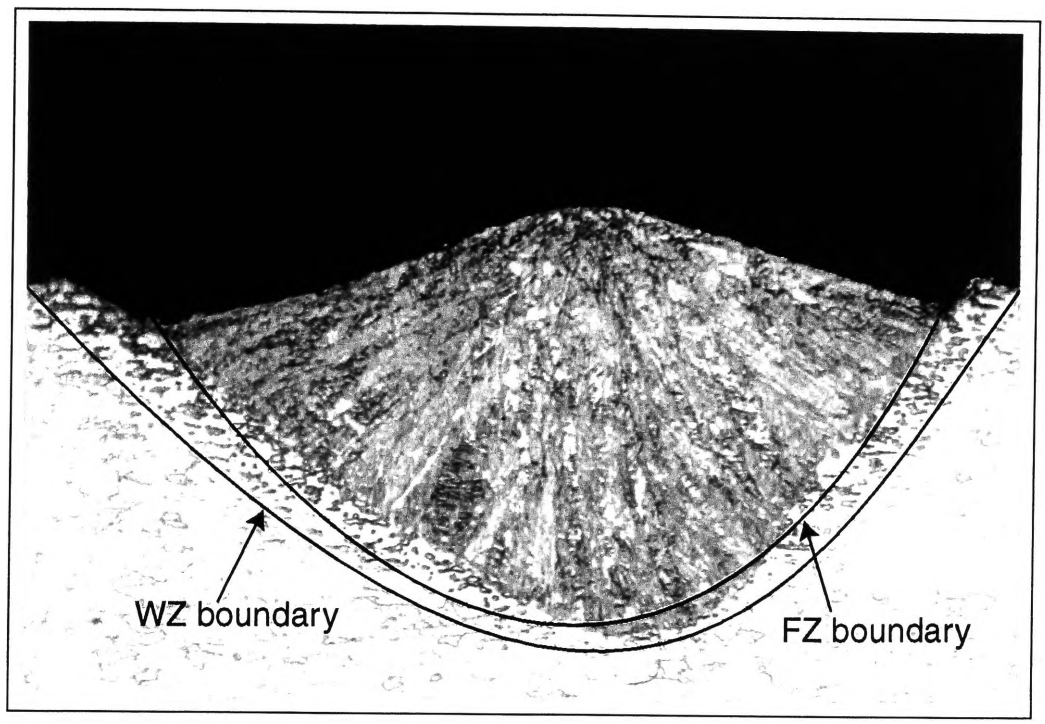

Figure 5.3 Micrograph of the longitudinal section of a single laser spot weld on AISI 1006 steel showing ANSYS model predictions of the FZ and WZ boundaries (x 120).

Conditions: 7 J, focus 0 mm, 3 ms, 20 Hz, 3000 mm/min.

Figure 5.4, as well as ANSYS model predictions of the FZ and WZ boundaries. A back-scattered electron image of the planar view is also provided, along with corresponding predictions of the size and shape of the fusion zone.

All FZ and WZ dimensions associated with the single spot focal scan from -5 mm to +5 mm have been plotted in Figures 5.5(a) and 5.5(b), and may be compared directly with the experimental measurements of the FZ and WZ dimensions, respectively. Figures 5.6(a) and 5.6(b) show the dimensions associated with the single spot energy scan from 3 J to 11 J. The corresponding experimental measurements are also shown.

In general, the agreement between experiment and theory is within 5-10% for all of the indicated weld bead dimensions. This good agreement between experimentally determined weld dimensions and the numerical model calculations was achieved by adjusting only one parameter, the effective absorptivity of the beam. A full discussion of the results presented here appears in section 5.6.

5.5.2 Single-beam overlapping spot welds

The finite element model was run to simulate welding speeds of 700 mm/min and 350 mm/min. For each speed, the model was run until quasi-steady state was reached (30 pulses). In the former case, the depths of the FZ and WZ were calculated to be 0.45 mm and 0.5 mm, respectively. This compares with measured depths of 0.48 mm and 0.52 mm. For the 350 mm/min welding speed, a slight increase in the calculated depth of each zone was observed (0.46 mm and 0.51 mm), although the measured depths were the same as those for the faster welding speed. As discussed in section 4.3.2, this similarity can be attributed to the difficulty in locating the FZ boundary, which results in a measurement error of approximately $\pm 5\%$. An error of $\pm 1\%$ is also associated with each of the laser parameters. Nevertheless, the agreement between experiment and theory is good. Model predictions of FZ and WZ boundaries for the welding speed of 350 mm/min have been superimposed on the micrograph shown in Figure 5.7. To illustrate the difference in the thermal history of the workpiece for each speed, a graph of the calculated temperature vs. time at a point on the centre-line of a weld 0.5 mm below

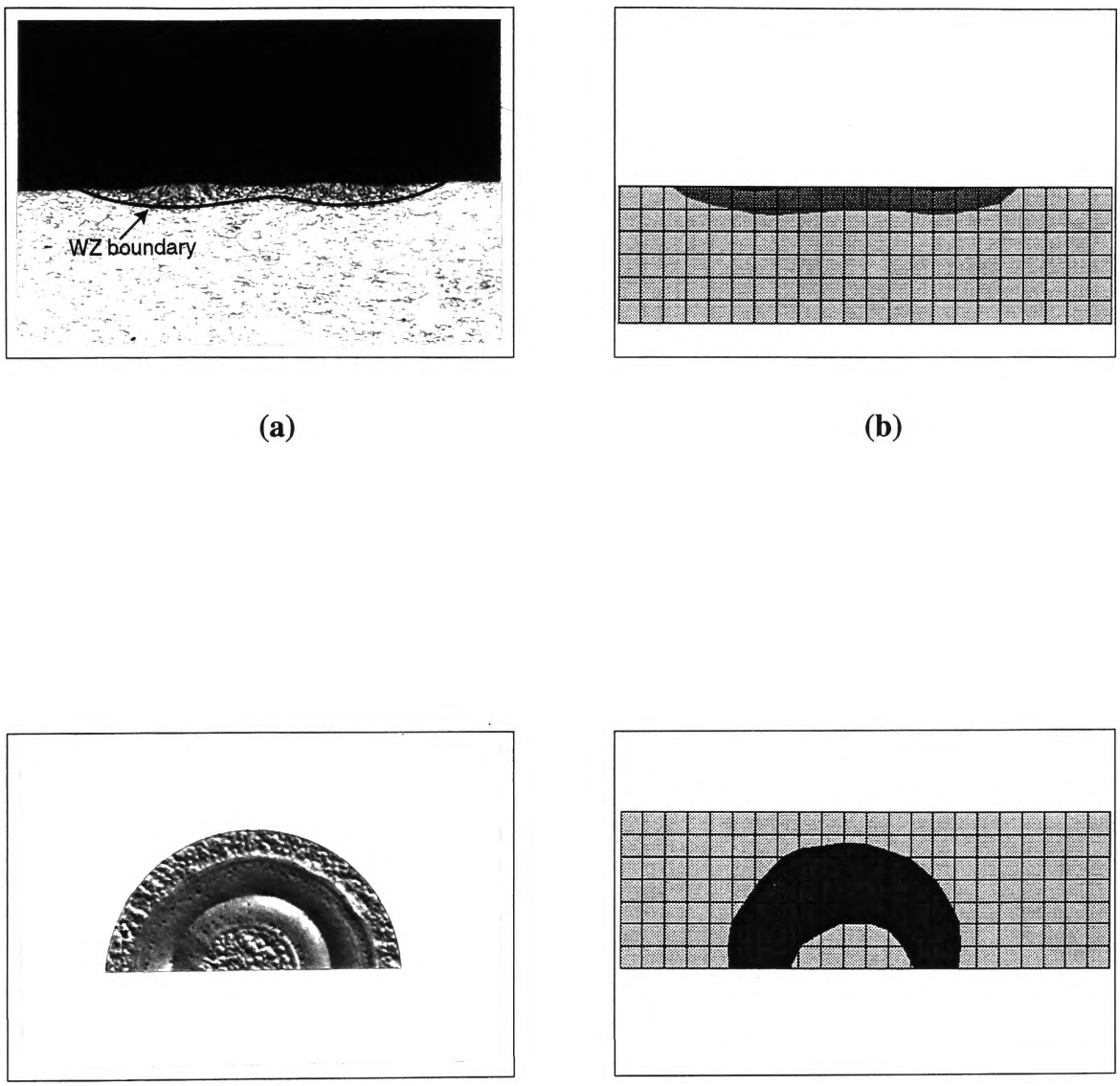

Figure 5.4 **(a)** Micrograph of the longitudinal section of a single laser spot weld showing the WZ boundary (x 30). Conditions: 7 J, focus -5 mm, 3 ms, 20 Hz, 3000 mm/min. **(b)** Longitudinal view of ANSYS model predictions of the FZ and WZ for the conditions in (a). **(c)** Back-scattered electron image of the planar section of half a laser spot weld showing the FZ for the conditions in (a). **(d)** Planar view of ANSYS model prediction of the FZ for the conditions in (a).

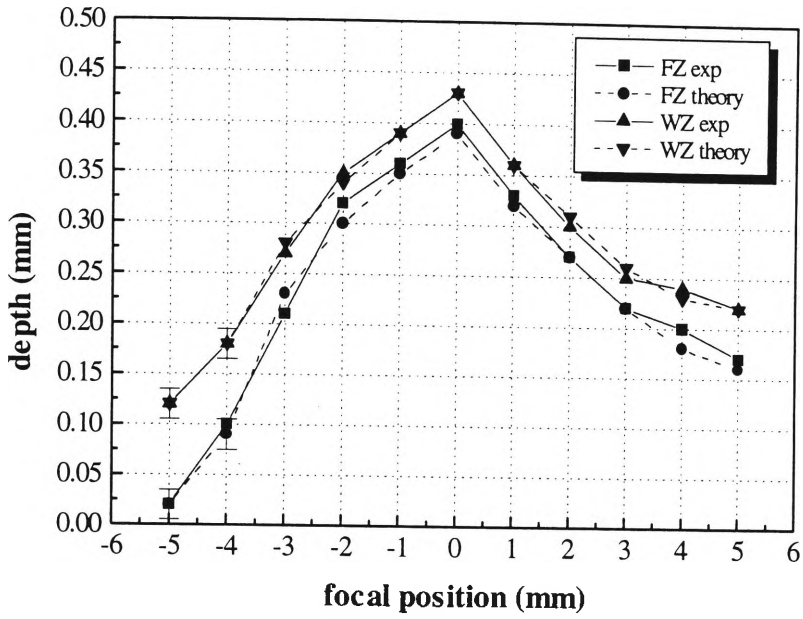

Figure 5.5(a) Measured FZ and WZ depths compared with model predictions.

Conditions: 7 J, 3 ms, 20 Hz, 3000 mm/min.

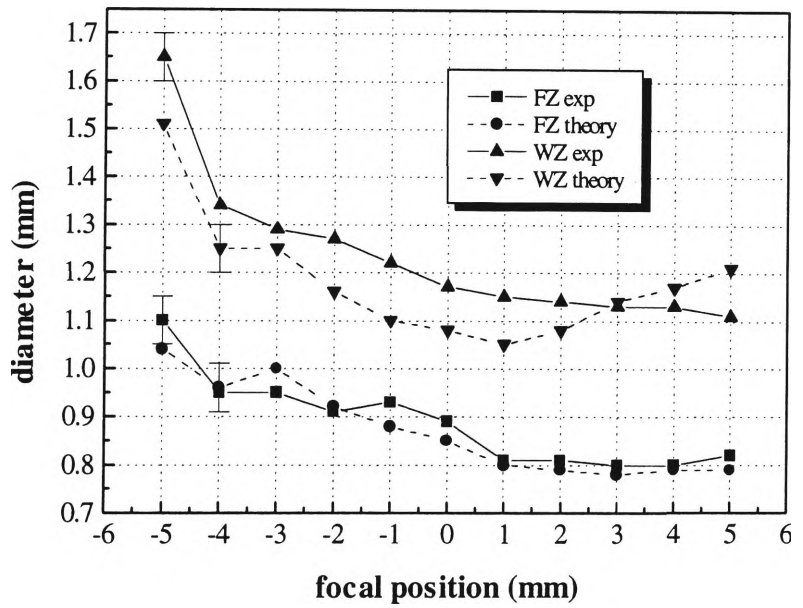

Figure 5.5(b) Measured FZ and WZ diameters compared with model predictions.

Conditions: 7 J, 3 ms, 20 Hz, 3000 mm/min.

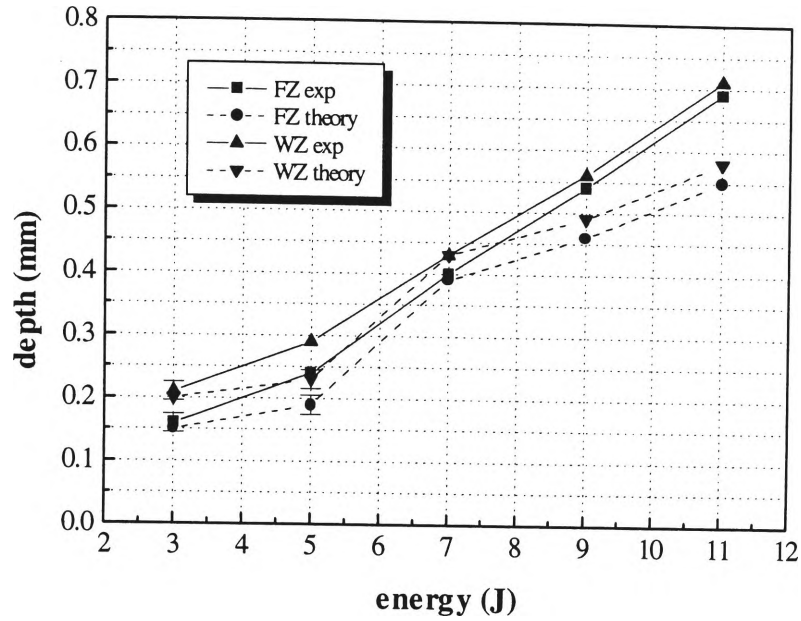

Figure 5.6(a) Measured FZ and WZ depths compared with model predictions.

Conditions: focus 0 mm, 3 ms, 20 Hz, 3000 mm/min.

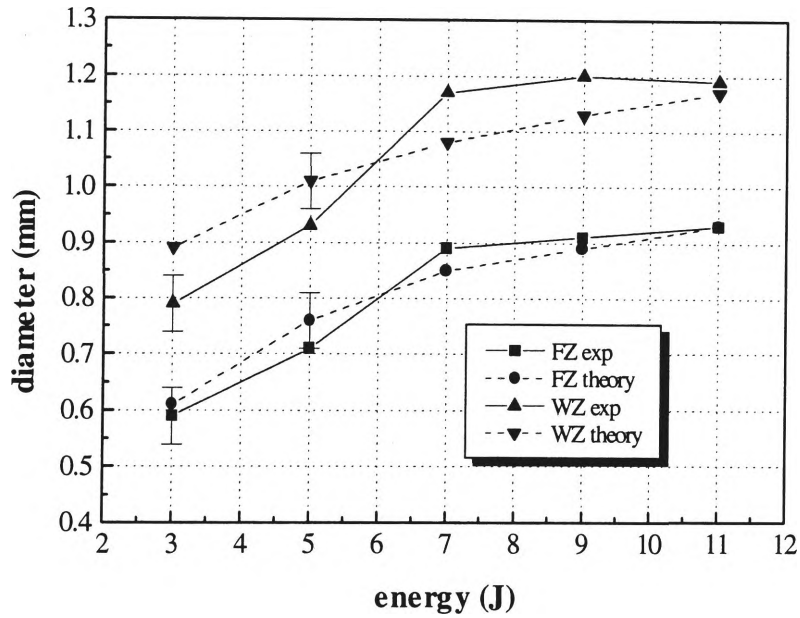

Figure 5.6(b) Measured FZ and WZ diameters compared with model predictions.

Conditions: focus 0 mm, 3 ms, 20 Hz, 3000 mm/min.

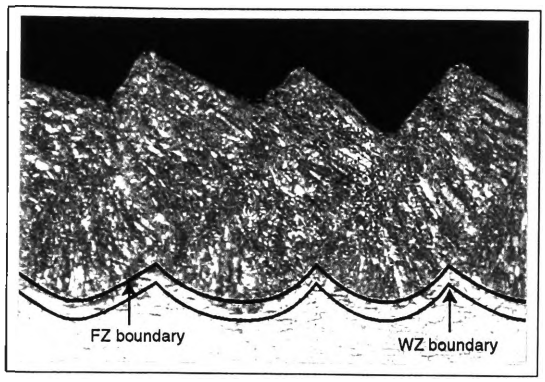

Figure 5.7 Micrograph of the longitudinal section of a series of overlapping spot welds showing ANSYS model predictions of the FZ and WZ boundaries (x 60).

Conditions: 7 J, focus 0 mm, 3 ms, 20 Hz, 350 mm/min.

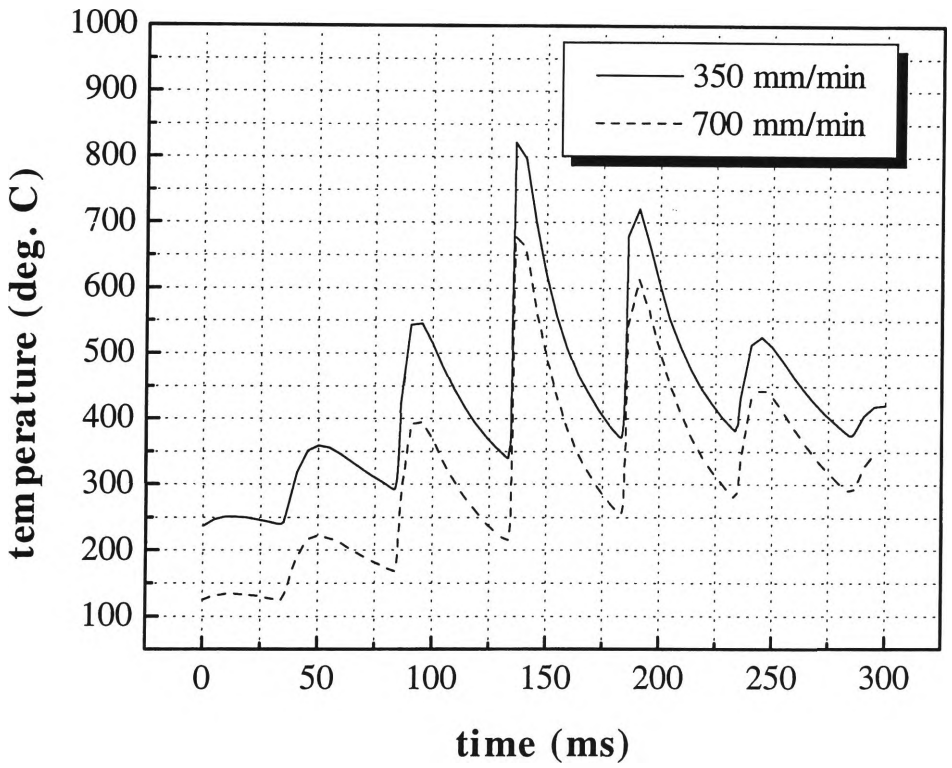

Figure 5.8 Graph of calculated temperature vs. time for a point on the centre-line of a weld 0.5 mm below the workpiece surface for welding speeds of 350 mm/min and 700 mm/min.

Conditions: 7 J, focus 0 mm, 3 ms, 20 Hz.

the workpiece surface for each speed has been shown in Figure 5.8. By reducing the speed from 700 mm/min to 350 mm/min, the peak temperature is seen to increase by about 150 °C.

To check the results of the model, temperature predictions were compared with the pyrometric measurements of Scott[122]. The results of measurements taken on the weld centre-line for the upper and lower surfaces are shown in Figures 5.9(a) and 5.9(b), respectively. Also shown in the figures are the predictions of the numerical model for the surface temperatures. The general form of the thermal history is that of a series of "spikes" in temperature corresponding to the repetition rate of the laser, followed by an almost exponential decrease in the temperature between each pulse.

Associated with each welding pulse is a small, bright plume of metal vapour and plasma which extends 10-15 mm above the surface of the workpiece, and expands from the diameter of the spot weld to a diameter of about 5 mm over this distance, depending on the welding conditions. This very bright plume precludes the pyrometric measurement of temperatures perpendicular to the workpiece surface. The measurements of Scott were therefore made at an angle of 30°, resulting in less plume radiation and not too large an increase in measurement spot size (0.2 mm^2 to 0.23 mm^2). The influence of the plume on the measurement of temperature was checked by setting the angle of detection to almost 90° and skimming the surface of the workpiece to ensure that only light from the plume was detected. This experiment revealed that the bright plasma lasted only for the length of the laser pulse, and that the detection system recovered within 0.4 ms of the end of the pulse.

It can be seen from Figures 5.9(a) and 5.9(b) that the agreement between experiment and theory is reasonable near the centre-line. This result is consistent with the fact that the model predicts the FZ and WZ dimensions with considerable accuracy. It should be emphasised that there has been no fitting of the theoretical predictions to experiment for the top surface. However, for the bottom surface, the temperature predictions of the model were multiplied by 0.81 to achieve the agreement shown in Figure 5.9(b). The possibility that the basic constituents of the numerical model may be

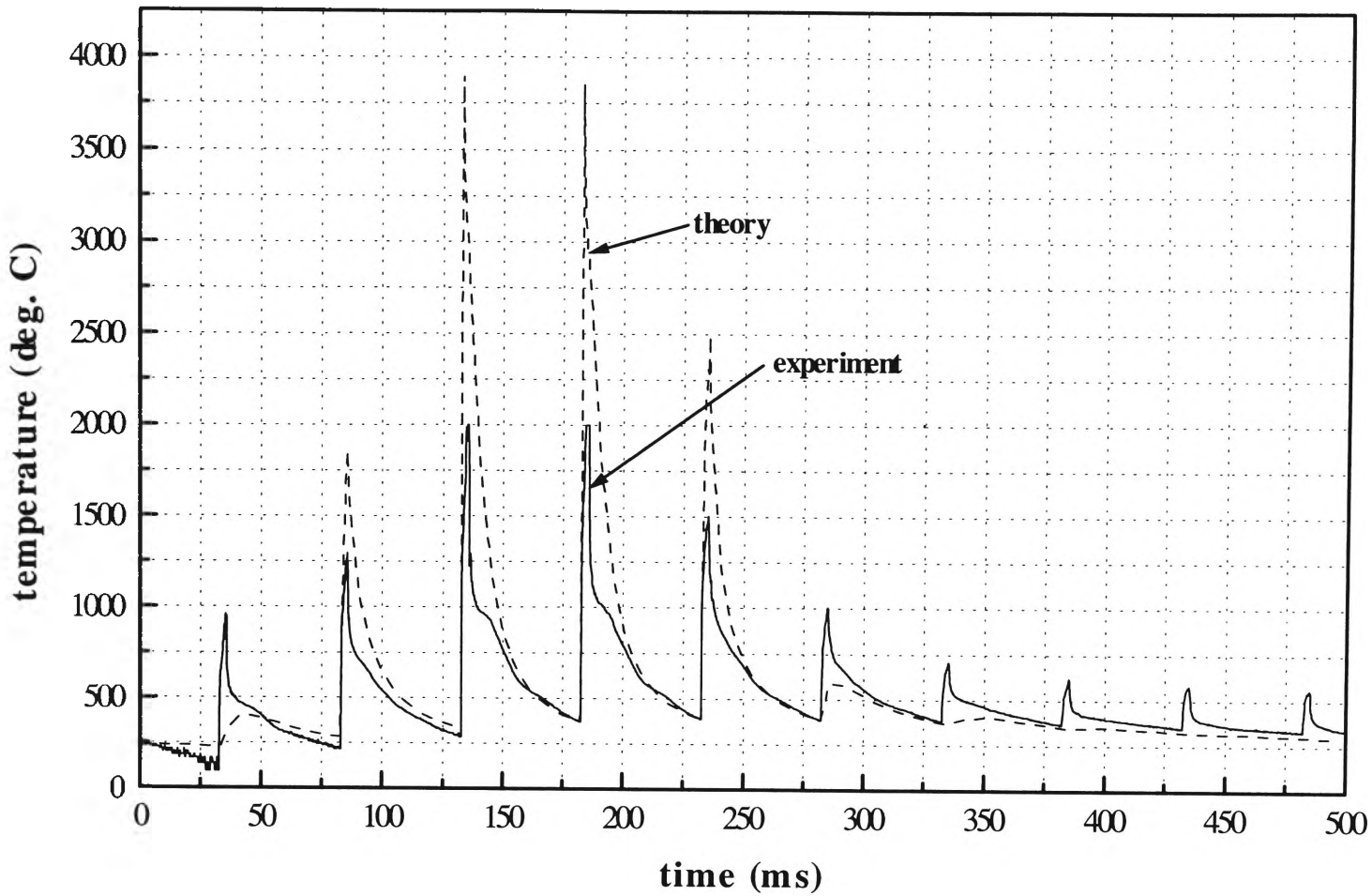

Figure 5.9(a) Comparison of model predictions and pyrometric measurements for a point on the top surface of a 0.9 mm AISI 1006 steel plate. Weld centre-line temperatures are shown. Conditions: 7 J, focus 0 mm, 3 ms, 20 Hz, 350 mm/min.

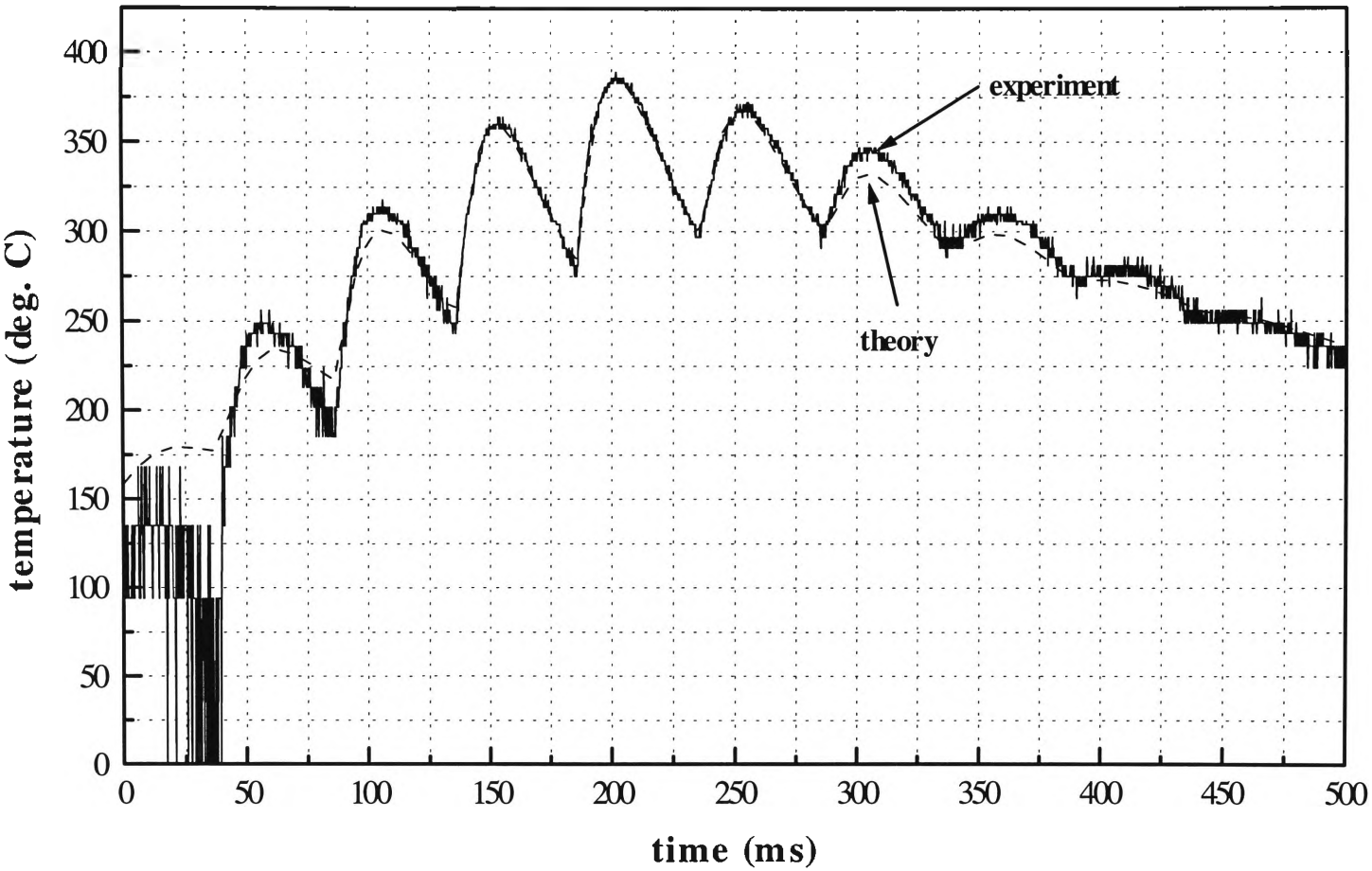

Figure 5.9(b) Comparison of adjusted model predictions (see section 5.5.2) and pyrometric measurements for a point on the bottom surface of a 0.9 mm AISI 1006 steel plate. Weld centre-line temperatures are shown. Conditions: 7 J, focus 0 mm, 3 ms, 20 Hz, 350 mm/min.

wrong was therefore explored. The quantities that most affect the cooling rate of the material are thermal conductivity and specific heat. When each of these quantities was varied by approximately two orders of magnitude, a much closer agreement between experiment and theory was established for both top and bottom surfaces. However, this wide variation in the thermophysical properties of the material is unlikely. Rather drastic tests such as these, as well as single pulse tests, analytical checks and other numerical checks have indicated that it is unlikely that the basic constituents of the model are incorrect.

The observed discrepancy is more likely to be attributed to the assumption that the emissivity of the steel remains constant during the heating and cooling of the material, an assumption made implicitly by the optical pyrometer. A constant emissivity is clearly not possible as the material will undergo significant changes in phase, temperature, surface topography and oxidation state during pulsed laser welding. A highly oxidised surface may have an emissivity near 100%, whereas a clean, smooth steel surface only 30%. For this reason, relatively small changes in surface properties tend to lead to large changes in the "measured" temperatures. For example, a blackbody of temperature 800 °C (emissivity 100%) would be measured to have a temperature of nearly 1100 °C if the emissivity of the pyrometer were set at 30%.

5.5.3 Tandem-beam non-overlapping spot welds

The finite element model was run to simulate a welding speed of 3000 mm/min. This speed was fast enough to ensure no overlap of composite spot welds. Thus the effect of a composite laser spot could be examined. The maximum depth of the FZ and WZ as a function of inter-beam distance for both sets of conditions selected in the study are shown in Figures 5.10 and 5.11. These values are directly compared with the actual spot weld dimensions. Although the observed disparities between theory and experiment are as large as 30%, the results are not surprising. As discussed in section 4.2.3, the role of the plasma during keyhole welding is a very complex one. Accurate predictions of weld zone size and shape require an intimate understanding of the absorption mechanisms within the keyhole. This pertinent aspect is discussed further in section 5.6.

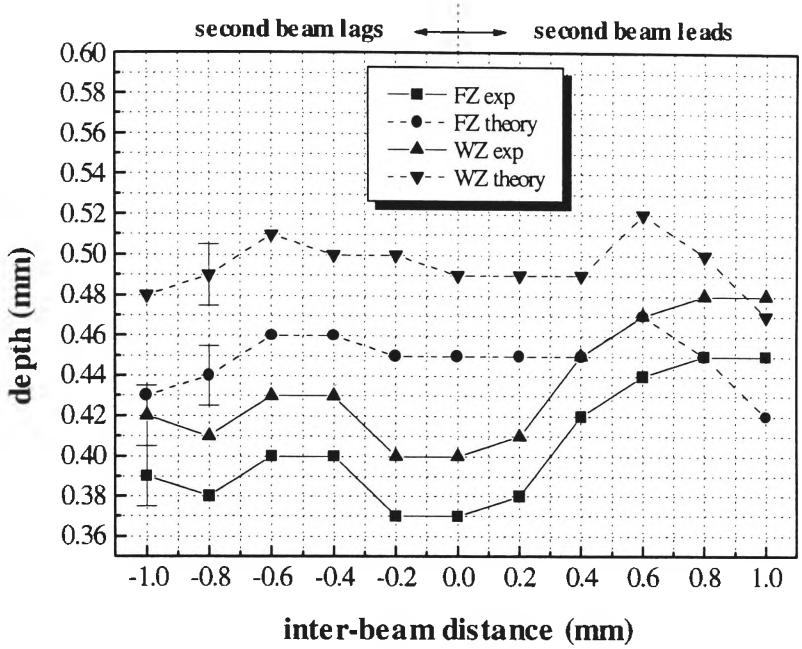

Figure 5.10 Measured FZ and WZ depths compared with model predictions.

Conditions: beam 1 - focus 0 mm, 7 J; beam 2 - focus -5 mm, 7 J.

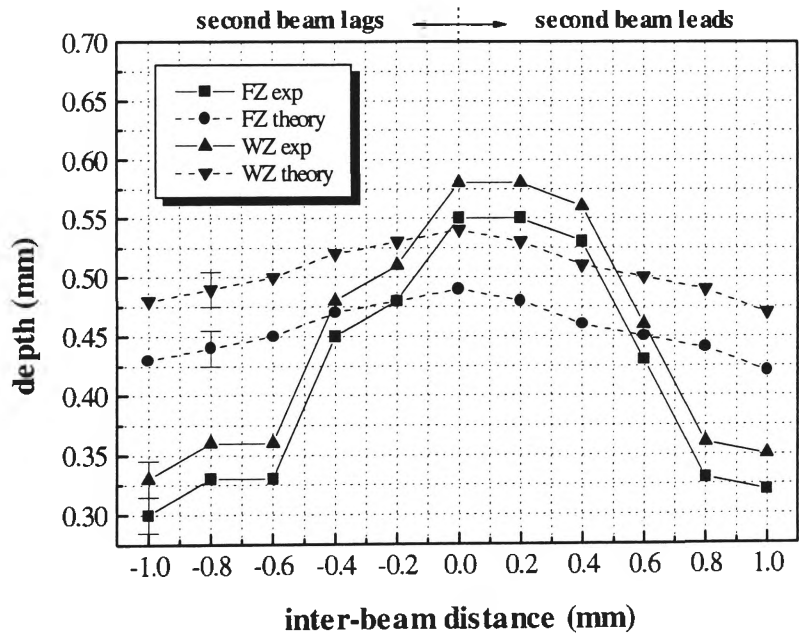

Figure 5.11 Measured FZ and WZ depths compared with model predictions.

Conditions: beam 1 - focus 0 mm, 7 J; beam 2 - focus 0 mm, 7 J.

5.5.4 Tandem-beam overlapping spot welds

The dimensions of the quasi-steady state FZ and WZ dimensions for the selected tandem laser beam conditions are presented in Table 5.5. The corresponding numerical and analytical model predictions are also shown. For a select set of welding conditions, an isometric view of the numerical model prediction of the maximum temperature reached by the workpiece is shown in Figure 5.12. From such a diagram the maximum depths of the FZ and WZ have been measured.

For the analytical model, the thermophysical properties of AISI 1006 steel were integrated with respect to temperature in order to provide mean values for density (7075 kg m^{-3}), specific heat (594 J kg^{-1} K^{-1}) and thermal conductivity (33 W m^{-1} K^{-1}). Furthermore, the experimentally measured beam profile at focus 0 mm was approximated by a Gaussian distribution with r_e = 300 μm. As the incidence angles of the main and minor beams were 10° and 45°, respectively, each elliptical laser spot was approximated by a circle described on the major axis of each ellipse (auxiliary circle). This method of employing auxiliary circles resulted in calculated temperatures which were less than what would be expected if ellipses were employed. These temperatures were estimated to be no more than 2% lower for the main beam and 10% lower for the minor beam. Given these approximations, the analytical model provides very similar estimates for both FZ and WZ depth. This validates the solution procedure incorporated in the numerical model of tandem laser welding.

5.5.5 A5005 aluminium alloy

A montage of macrographs is presented in Figure 5.13, showing the cross-sections of single-pulse laser spot welds formed as the focal position of the laser beam was varied between -5 mm (below the surface) to +5 mm (above the surface). The energy used in each case was 20 J. The very rapid cooling rates associated with the selected welding conditions have resulted in solidification cracking within the FZ of some spot welds. The depth and diameter of the FZ associated with each spot weld have been plotted in Figures 5.14(a) and 5.14(b), respectively. Predicted spot weld dimensions are also shown. The difficulty in distinguishing the heat-affected zone using optical

Main Beam Energy and Focal Position	Minor Beam Energy and Focal Position	Inter-Beam Distance (mm)	Experiment	Numerical Model	Analytical Model
7 J, 0 mm	7 J, -5 mm	-1	0.6, 0.75	0.52, 0.7	N/A
		0	0.7, 0.9	0.59, 0.85	N/A
		+1	0.68, 0.9	0.6, 0.9	N/A
2 J, 0 mm	2 J, 0 mm	-1	0.12, 0.18	0.14, 0.22	0.13, 0.22
		0	0.24, 0.29	0.26, 0.31	0.26, 0.32
		+1	0.12, 0.18	0.14, 0.22	0.13, 0.22
1 J, 0 mm	1 J, 0 mm	-1	0.06, 0.1	0.04, 0.11	0.04, 0.11
		0	0.1, 0.15	0.1, 0.16	0.09, 0.15
		+1	0.06, 0.1	0.04, 0.11	0.04, 0.11

Table 5.5 Comparison of experimental, numerical and analytical FZ and WZ depths.

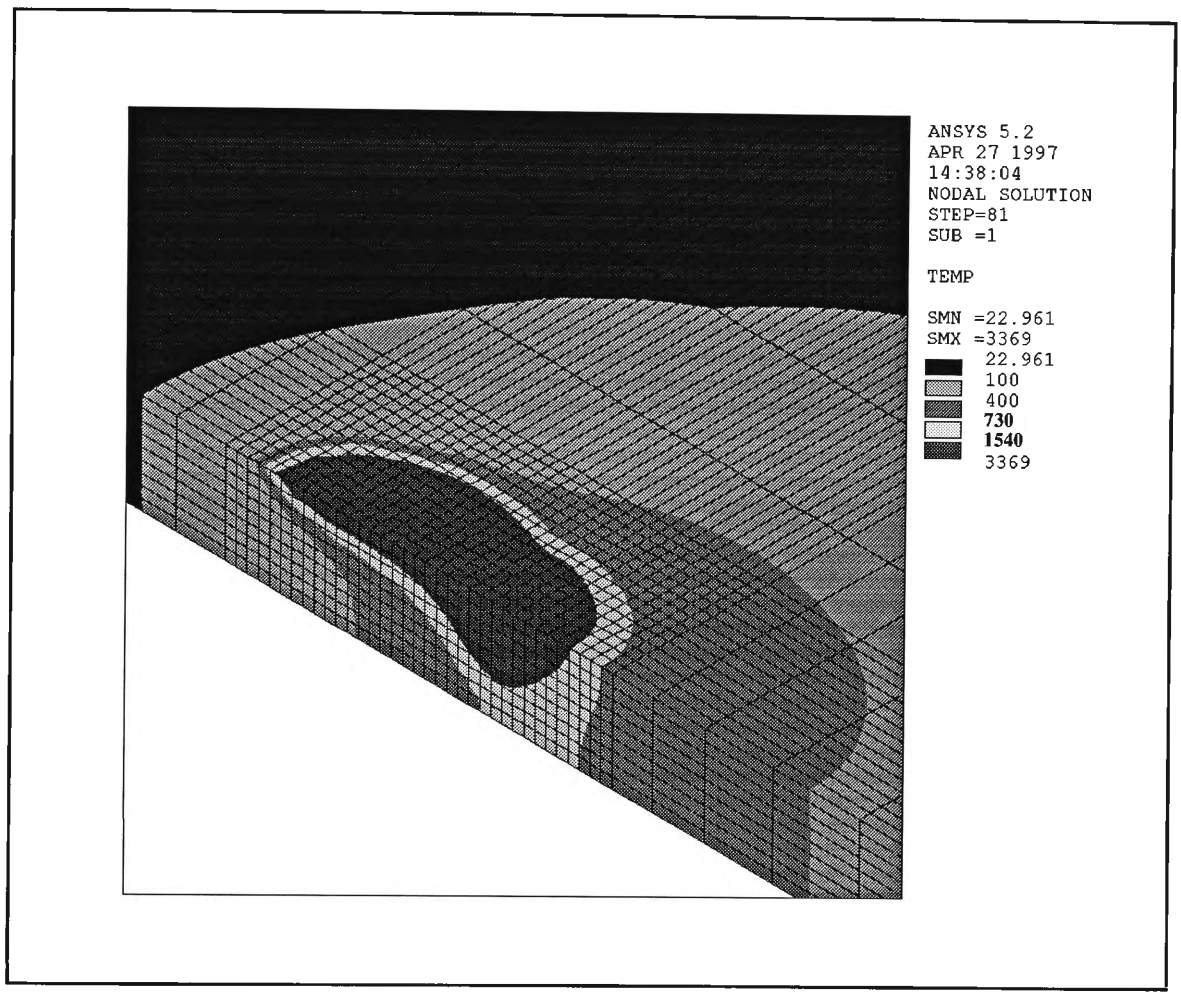

Figure 5.12 Isometric view of the ANSYS model prediction of the maximum temperature reached by the workpiece. Each element in the fine section of the mesh has dimensions of 0.1 mm x 0.1 mm x 0.1 mm. Conditions: main beam - focus 0 mm, 7 J; pre-heat beam - focus -5 mm, 7 J; inter-beam distance = +1 mm; 3 ms, 20 Hz, 350 mm/min. Note: FZ depth = 0.6 mm, WZ depth = 0.9 mm (plate thickness).

Figure 5.13 Macrographs of the longitudinal sections of laser spot welds on A5005 alloy from focus +5 mm to focus -5 mm (x 15).
Conditions: 20 J, 3 ms, 20 Hz, 3000 mm/min.

-3

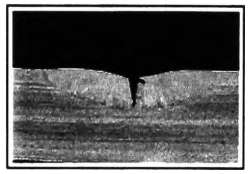

-4

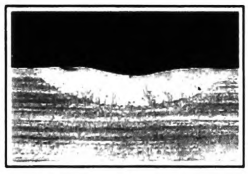

-2

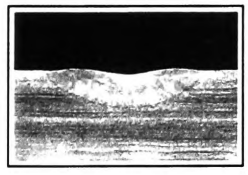

-5

-1

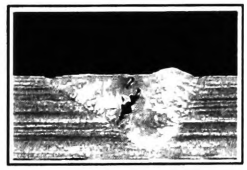

0

+5

+1

+4

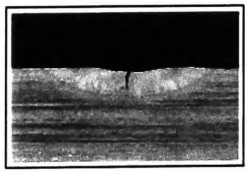

+2

+3

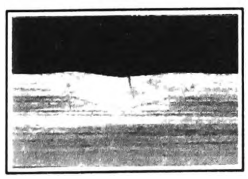

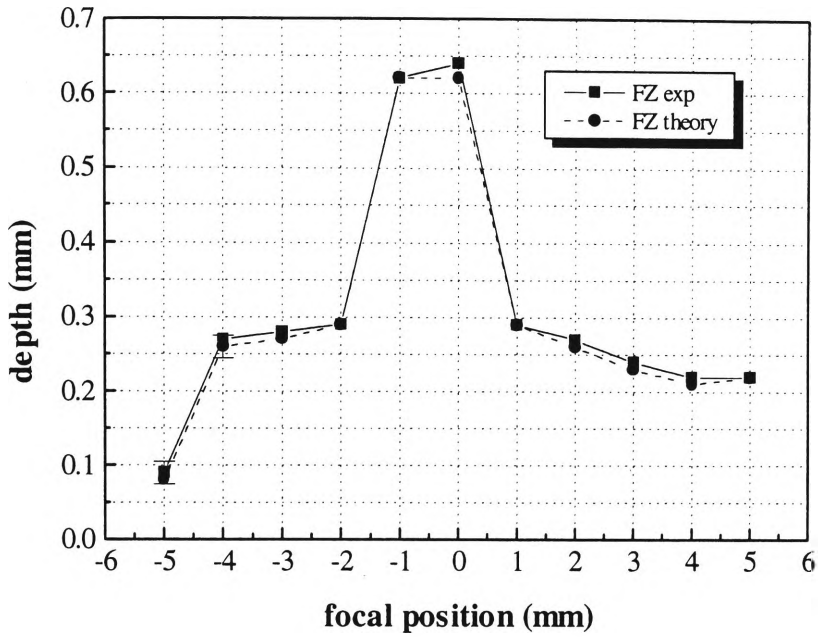

Figure 5.14(a) Measured FZ and WZ depths compared with model predictions.
Conditions: 20 J, 3 ms, 20 Hz, 3000 mm/min, A5005 alloy.

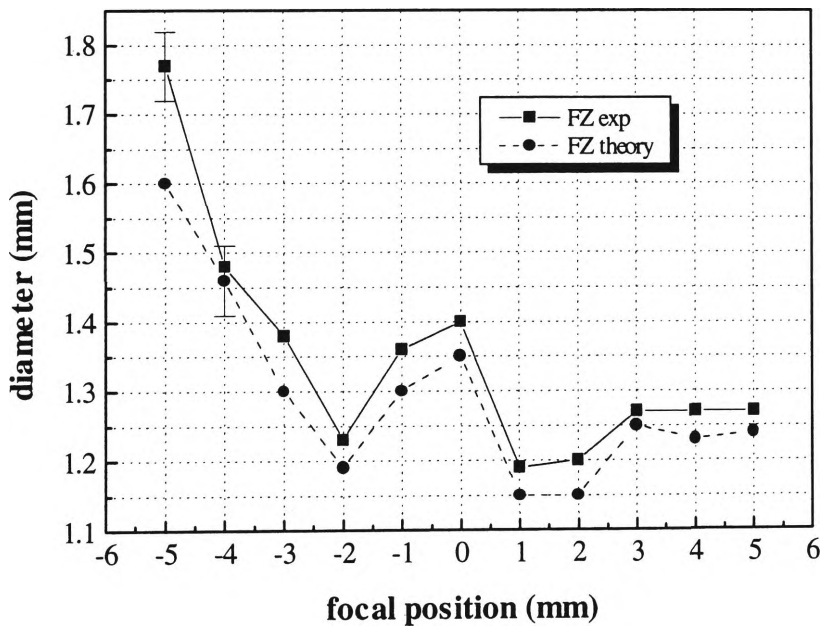

Figure 5.14(b) Measured FZ and WZ diameters compared with model predictions.
Conditions: 20 J, 3 ms, 20 Hz, 3000 mm/min, A5005 alloy.

microscopy precluded the measurement of WZ dimensions.

Just as for the AISI 1006 steel spot welds, it was found that the diameter of the spot weld was relatively insensitive to focal position, with a general decrease in diameter as the focus shifted from beneath the surface of the alloy to above the surface. FZ depth was a much stronger function of focal position, with maximum penetration again being obtained when the laser beam was focussed at the surface of the workpiece (focus 0 mm). Indeed, the spot welds at focus 0 mm and -1 mm clearly indicate the initiation and rapid growth of a keyhole during the laser pulse. This rapid increase in the depth of the keyhole, which is associated with a very high fraction of radiation being absorbed at the walls of the keyhole, was not apparent for the steel welds presented in this study.

A reduction in the energy of the laser pulse from 20 J to 18 J was sufficient to produce conduction-limited welds at both focal positions, with depths of 0.29 mm in each case. This compares with depths of 0.64 mm (focus 0 mm) and 0.62 mm (focus -1 mm) at the higher energy. This transition is also reflected in the numerical predictions with a reduction in the depth of penetration from 0.62 mm to 0.37 mm (focus -1 mm) and 0.62 mm to 0.38 mm (focus 0 mm). The latter result, where a keyhole is clearly not present, is verified by the conduction-limited analytical model, which predicts a FZ depth of 0.35 mm when the laser beam is focussed at the surface.

5.6 DISCUSSION

5.6.1 Spot weld dimensions

Previous work has shown that the best penetration associated with pulsed laser spot welds is achieved when the focal point is located 2-3 mm below the surface of the workpiece[141]. This value was based on the assumption that the minimum weld pool diameter corresponds to the focal point of the laser beam being at the surface of the workpiece. This assumption was found to be misleading, particularly in the case of non-Gaussian beam profiles. In this study, an improved method of determining the focal point of the laser beam was employed. A Spiricon laser beam analyser (LBA-100) was

used to determine the optical focus of the laser beam as described in section 3.3.1. Using this analyser it was possible to measure the power distributed over the cross-section of the laser beam (beam profile) as a function of distance from the focussing lens. The position which gave the maximum power density was deemed the focal position for the purpose of this study. The laser beam profile either side of this position was found to vary from a near-Gaussian profile (at positive focal positions) to donut-shaped profiles (at negative focal positions). The most accurate way of correlating spot welds with beam profiles was to compare these donut-shaped beam profiles with the donut-shaped melt zones. As outlined in section 5.5, by performing a focal scan on both AISI 1006 steel and A5005 aluminium alloy to produce a series of individual spot welds, it was possible to match the diameter of the "annular" or donut-shaped beam profiles with the diameter of the annular spot welds. From an optical point of view therefore, it was found that under these laser conditions the point of maximum penetration actually occurred at 0 mm, i.e. when the beam was focussed at the surface of the workpiece. This method of determining the focus is corroborated by the finite element model. The predicted weld pool shapes are in excellent agreement with the experimental welds. These correlations are very poor if the previous method of determining the focal position is used.

The results in Figures 5.5(b) and 5.14(b) verify this method of determining focus. It can be seen that the minimum melt diameter (FZ) is in fact at around +2 or +3 mm. The focal position at which the maximum power density is obtained does not yield the smallest diameter spot weld due to the different intensity distributions at different focal positions.

5.6.2 Effective absorptivity and energy distribution

The incorporation of accurate thermophysical properties to be used as input to the above models of single-beam and tandem-beam pulsed laser welding is a difficult task, since a metal heated beyond its boiling point in less than 3 ms undergoes rapid changes. This task is more perilous when the temperature dependence of some important material properties is unknown. The absorptivity of the laser radiation is one

such parameter.

The absorptivity of the 1.06-μm laser radiation by the workpiece is a complex function of a number of variables such as the nature of the surface, the level of oxidation, surface temperature, beam power density, beam angle of incidence, focal position of the laser beam relative to the workpiece surface, different amounts of absorption across the beam itself, and the amount of plasma present. Since their precise roles have not been determined, either experimentally or theoretically, an effective absorptivity for each focal position was incorporated into the present analysis. This parameter incorporates, in an approximate way, all of these complex effects. The modification of energy input by convective movement is also included in this factor.

The variation of effective absorptivity with focal position for both AISI 1006 steel and A5005 aluminium alloy is shown in Table 5.6. An effective absorptivity for each focal position was selected to achieve a match within 5% between theory and experiment for just one set of results, in this case the maximum depth of the 730 °C isotherm below the surface (WZ depth) for the single-beam non-overlapping spot welds shown in Figures 4.1 and 5.13. When these values are used under these welding conditions, agreement within 10% between theory and experiment for FZ depth, FZ diameter and WZ diameter is achieved (Figures 5.5 and 5.14). These effective absorptivities were then used for all of the other welds modelled in the present study. The selected absorptivities compare well with previous estimates of the absorptivity of low-carbon steels[89] and aluminium alloys[142] to radiation of wavelength 1.06 μm. In general, the results suggest that this approach has been justified, although selected tandem-beam predictions differ from experimental measurements by as much 30%.

It should be emphasised that the selection of an effective absorptivity for each focal position represents the only "calibration" factor in the model. Realistic temperature-dependent variables were used for all other thermophysical properties. The inclusion of experimentally determined beam profiles represents another important feature of the model. As the energy distribution at the surface of the workpiece is a strong function of both focal position and beam incidence angle, incorporation of these

Focal Position (mm)	Absorptivity (%) of AISI 1006 Steel	Absorptivity (%) of A5005 Alloy
-5	35	14
-4	33	11
-3	33	12
-2	33	11
-1	37	13
0	30	13
+1	28	12
+2	28	12
+3	30	12
+4	25	11
+5	25	10

Table 5.6 Focal position vs. absorptivity to produce a close comparison between theory and experiment for the conditions shown in Figures 5.5 and 5.14.

	Model Prediction		Experiment
	Measured Profile	Top-Hat Profile	
FZ depth	0.39 mm	0.46 mm	0.4 mm
FZ diameter	0.85 mm	0.68 mm	0.89 mm
WZ depth	0.43 mm	0.5 mm	0.43 mm
WZ diameter	1.08 mm	0.87 mm	1.17 mm

Table 5.7 Comparison of WZ and FZ dimensions for both an experimentally measured beam profile and an artificially generated top-hat profile.
Conditions: 7 J, 3 ms, 20 Hz, 3000 mm/min.

measured beam profiles is essential for accurate temperature calculations and weld pool shapes.

To demonstrate the sensitivity of the model to intensity distribution, the model was run using the laser beam profile at focus 0 mm (Figure 3.2) and then an artificially generated top-hat profile of the same full width at half maximum (FWHM) and the same total energy as the measured profile. A comparison of the predicted depths and diameters of the FZ and WZ is shown in Table 5.7. This clearly indicates that unless the correct intensity profile is used as input for the model, large discrepancies between model predictions and experimental results will occur. The results of numerical and analytical models of the laser welding process which assume line, Gaussian or top-hat profiles of intensity distribution must therefore be treated with caution. All the calculations in the present numerical study have used experimentally measured energy distributions.

5.6.3 Thermal history

Model predictions of temperature vs. time provide a valuable insight into the formation of a laser weld. Figure 5.15 is a graph of temperature vs. time for a point on the centre-line of a weld 0.5 mm below the workpiece surface during tandem-beam welding. Inter-beam distances of +1 mm, 0 mm and -1 mm are considered. These thermal histories may be compared directly with the corresponding single-beam thermal history shown in Figure 5.8. They are quite different in that the peak temperature reached during tandem-beam welding for all inter-beam distances is about 2-3 times the temperature associated with single-beam welding. More significantly, the tandem-beam model indicates that for each inter-beam distance, the point on the weld centre-line is heated well into the austenite phase field during two successive pulses. The subsequent pulse only partially re-austenitises the material. On cooling below 800 °C, a significant amount of time is spent within the temperature range 500 °C - 800 °C: approximately 260 ms for d = +1 mm, 305 ms for d = 0 mm, and 405 ms for d = -1 mm. During single-beam welding, however, the point of interest is only just heated above 800 °C and therefore partially austenitised. In addition, the inter-pulse cooling rates of the steel are

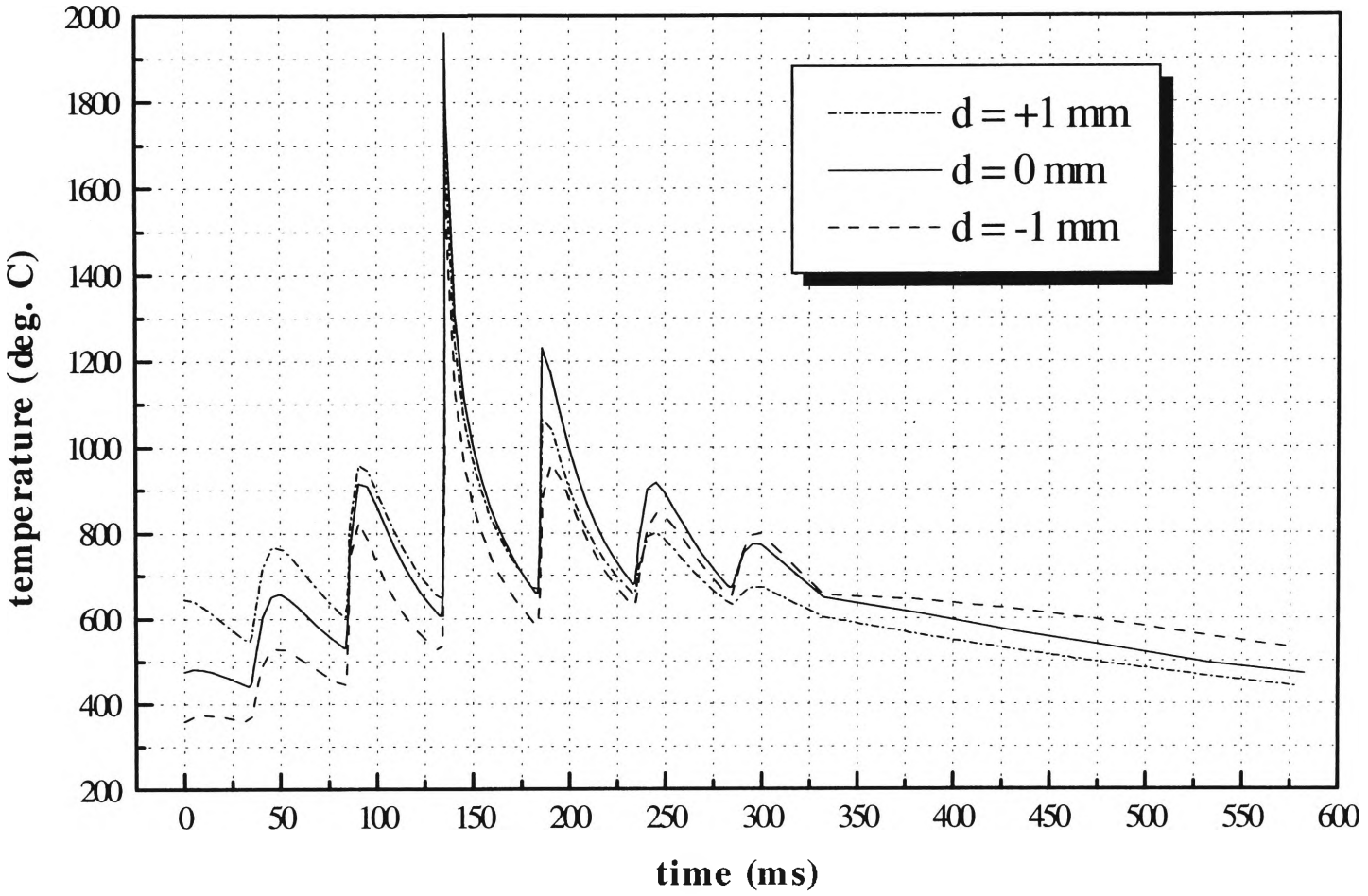

Figure 5.15 Graph of calculated temperature vs. time for a point on the centre-line of a weld 0.5 mm below the workpiece surface during tandem-beam welding. Inter-beam distances of +1 mm, 0 mm and -1 mm are shown. Conditions: beam 1 - focus 0 mm, 7 J; beam 2 - focus -5 mm, 7 J; 3 ms, 20 Hz, 350 mm/min.

significantly higher for the single-beam weld. This can be seen by comparing the slopes of the curves at fixed temperatures.

The much longer "effective" $t_{8/5}$ times for the tandem cases are evident in the micrographs of the longitudinal sections of the single and tandem laser welds presented in this study. The single-beam weld shows a distinctly cast structure with columnar grains containing about 90% lath martensite and only 10% bainitic ferrite, indicating a rapid cooling rate and a short $t_{8/5}$ (Figure 4.5). Markedly different are the tandem welds which show a "normalised" structure because one or more of the downstream thermal spikes is capable of re-austenitising the cast structure and increasing $t_{8/5}$ to the extent that bainitic ferrite is the dominant constituent in the fusion zone (Figures 4.10, 4.11). This supports the model's predictions that the material remains in the 500 °C - 800 °C region for a time long enough to allow the transformation of austenite to bainitic ferrite.

CHAPTER 6

GENERAL DISCUSSION

6.1 SUMMARY OF EXPERIMENTAL AND THEORETICAL INVESTIGATIONS

Both three-dimensional numerical and analytical models of the heat flow during pulsed laser welding have been developed. The results of the models have been compared with experimental measurements of FZ and WZ dimensions. A very good agreement between theory and experiment for the single-beam laser weld beads has been achieved, with minimal assumptions made in the models. This agreement was not as favourable for the tandem-beam conditions selected in the study and the results indicate the inability of the heat conduction model to capture the complexities of the process. These complexities include the plasma formed above the weld area, the formation of a plasma-filled keyhole within the material, the angular dependence of Fresnel absorption, and the effects of surface tension and flow in the molten weld pool. The absorptivity of the 1.06-μm laser radiation by the workpiece is clearly a complex function of a number of variables such as the nature of the surface, the level of oxidation, surface temperature, beam power density, beam angle of incidence, focal position of the laser beam relative to the workpiece surface, different amounts of absorption across the beam itself, and the amount of plasma present.

Futhermore, as model predictions of the penetration rate of the plasma-filled keyhole were determined to be as high as 0.3 m s^{-1} for the AISI 1006 steel spot welds (energy 7 J, focus 0 mm) and 0.6 m s^{-1} for the A5005 spot welds (energy 20 J, focus 0 mm), the associated supersonic vapour velocities are likely to result in shock waves within the keyhole. Since the precise roles of all of these mechanisms have not been determined, an effective absorptivity of the laser beam for each focal position was incorporated into the analysis. This parameter includes, in an approximate way, all of these complex effects.

Full thermal histories of the weldment have also been generated, and the consequences of such predictions have been correlated with the microconstituents of the welds formed. A more direct check of the theoretical work, apart from the measurement of weld bead dimensions and the consequent estimations of temperature contours, was the direct comparison of temperature-time predictions with pyrometric measurements of the surfaces of sheet steel during welding. The measured temperatures were in

reasonable agreement with model predictions. This agreement has been discussed in section 5.5.2 and in the work of Scott[122].

Microstructural characterisation of various laser weld beads on AISI 1006 steel revealed the presence of lath martensite (M_L) and fine bainitic ferrite (FS(A)) in the fusion zone under single-beam welding conditions. These microconstituents are characteristic of very low heat inputs, accompanied by very rapid cooling rates. This type of structure differs from that observed in conventional fusion welds where cooling rates are considerably slower. In addition, the HAZ of these single-beam laser welds was considerably narrower with the partially transformed zone (ICHAZ) being the dominant subregion. The introduction of a second laser beam for pre- or post-heating was found to reduce the cooling rate to the extent that bainitic ferrite appeared as the main microconstituent in the FZ. This supported model predictions that the material remained in the 500 °C - 800 °C region for a time long enough to allow the transformation of austenite to bainitic ferrite.

For both single- and tandem-beam conditions, the Zincseal and Zincalume welds revealed very little lath martensite in the FZ. As zinc and aluminium both produce gamma loops in steel, there is a reduced temperature range in which austenite is stable. These ferrite stabilisers resulted in coarse, columnar grains of ferrite within the FZ for Zincalume, while bainitic ferrite was observed for Zincseal. Just as for the HAZ of all the AISI 1006 steel welds, the HAZ of both the single-beam and tandem-beam welds on each coated steel revealed M or M-A islands within a matrix of coarse ferrite grains. The main differences between the single- and tandem-beam welds appeared to be in the width of the HAZ and the "smoothness" of the weld bead surface. Under tandem welding conditions, the root HAZ width was generally 1.5 to 2 times larger, indicating much slower cooling rates. The surface of each tandem weld bead tended to be very flat, whereas noticeable peaks and troughs were evident in the single-beam welds. These welds were also more prone to the entrapment of porosity. These differences were not reflected in the results of tensile tests on various single- and tandem-beam butt joints, as all of the AISI 1006 steel and Zincseal welds failed outside the weld zone. In the case of Zincalume, however, failure occurred within the weld zone for both the single- and

tandem-beam specimens, with a strength reduction of approximately 8% in each case. Nevertheless, consideration of all of the test results reveals that in general the welds have not degraded the properties of the material.

In contrast to the results of the tensile tests, all of the tandem-beam butt joints displayed better formability than the single-beam butt joints. For example, in the case of AISI 1006 steel, the single-beam butt joint displayed a 22% reduction in formability when compared with the unwelded material. The tandem-beam butt joint only reduced the formability by 10%, indicating an improved microstructure. This improvement implies that the workpiece has undergone less rapid heating and cooling cycles during the tandem laser welding process. For Zincseal, the improvement was just as significant. For Zincalume, however, the problem of ablating the zinc-aluminium coating from the base metal was reflected in the marginal improvement in formability associated with the tandem-beam technique. In spite of this difficulty, the foregoing formability tests clearly demonstrate that the formabilities of the tandem-beam welds produced in this study are superior to those of the corresponding single-beam welds.

6.2 IMPLICATIONS OF THE STUDY

The experimental, numerical and analytical results presented in Chapters 4 and 5 have assisted researchers within the Cooperative Research Centre for Materials Welding and Joining to design a new type of laser processing head[122]. The aim was to construct a processing head which would give the same performance as two separate fibres and heads, while making use of the output from a single optical fibre (Figure 6.1). After the performance of the two heads was studied extensively, it was necessary to understand the optical characteristics of the commercial heads used for most of the experiments. A new optical design based on readily available optical components was then conceived by Scott[122]. This was followed by a design of the housing and necessary adjustments for the optical components. The resulting head could then accept a standard single optical fibre, collimate the diverging laser beam, divide this laser beam into two, and then refocus each beam individually onto the material being welded.

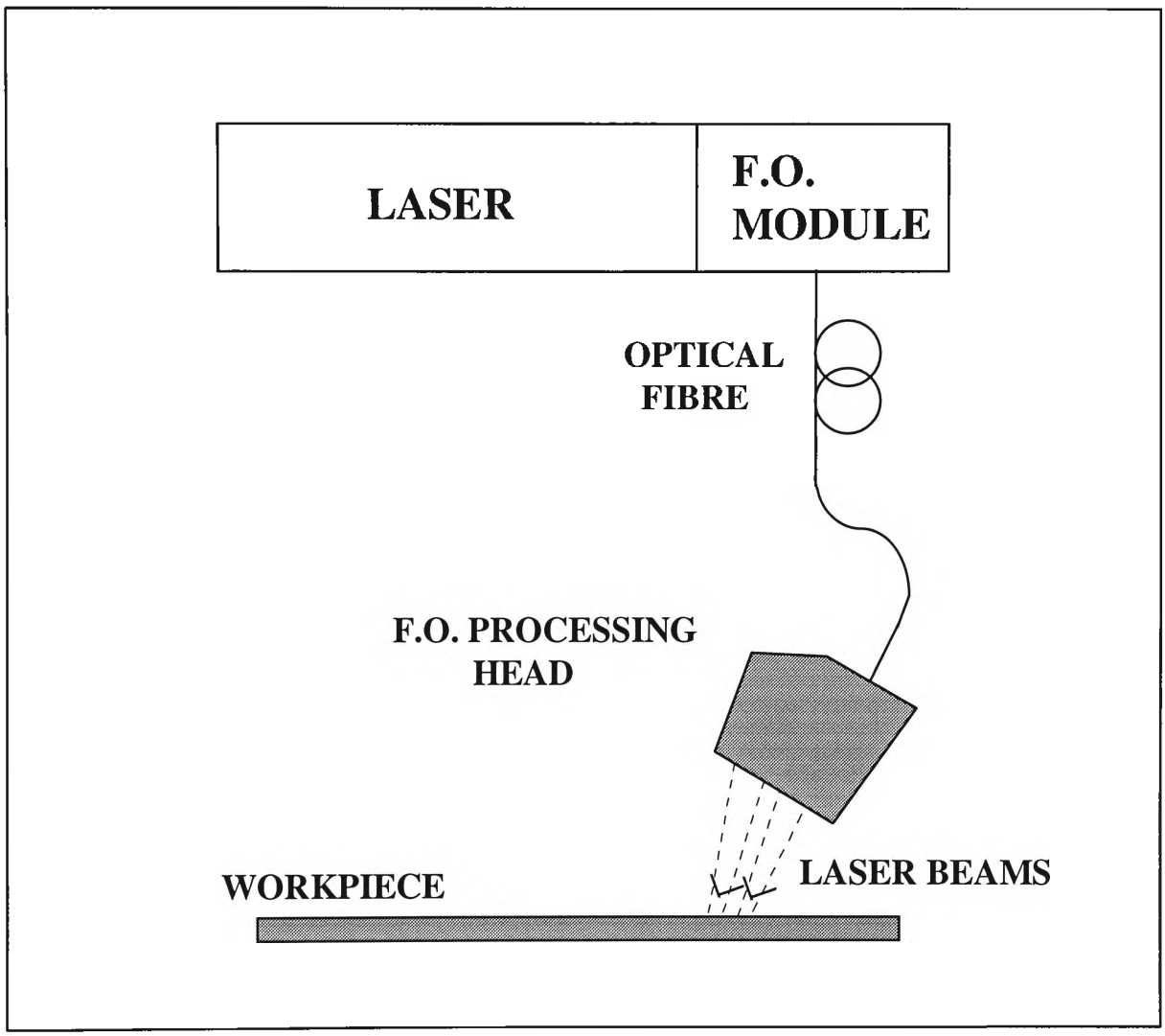

Figure 6.1 Schematic representation of the tandem fibre-optic laser welding head.

The optical design of the commercial LASAG heads used in the experiments consisted of a doublet of effective focal length 50 mm and diameter 40 mm, placed approximately 100 mm from the output end of the 600-μm stepped-index optical fibre. These lenses refocussed the laser beam, after passing through a protection glass of thickness 2 mm, at a position approximately 90 mm from the end of the housing of the head. All the surfaces of these optical components, with the exception of the end of the optical fibre, were anti-reflection coated. This design exhibited spherical aberration, and similar optical characteristics were necessary in the new head in order to achieve results commensurate with those obtained previously.

The new optical design according to Scott is shown in Figure 6.2. In order to adequately collimate the output of the optical fibre, it was necessary to use two lenses. The beam splitter was coated dielectrically to give a selected reflectivity at the wavelength of the Nd:YAG laser. One beam splitter of reflectivity 33% and another of reflectivity 50% (at an angle of incidence of 45°) were made for this head. The design of the head needed to allow the user to select which beam splitter to use for any given application. That part of the beam passing straight through the beam splitter, the main beam, was refocussed using a lens of nominal focal length 100 mm through a protection glass. The minor beam was guided by a mirror through another refocussing lens and protection glass. The focal point of this beam was located close to that of the main beam. The optical design software ZEMAX was used in the design and was also capable of predicting the intensity profile through any section of the optical path. This feature enabled appropriate selection of optical components to ensure similar beam profiles were generated as those measured for the twin head arrangement.

The new tandem fibre-optic laser welding head was designed to accept the standard LASAG optical fibre connector, allow the precise housing of the optical components, and provide adjustment of the focal position of each beam. The relative positions of each beam on the workpiece (inter-beam distance) can also be adjusted. The design also incorporates a gas shroud to shield the weld area from the surrounding oxidising atmosphere.

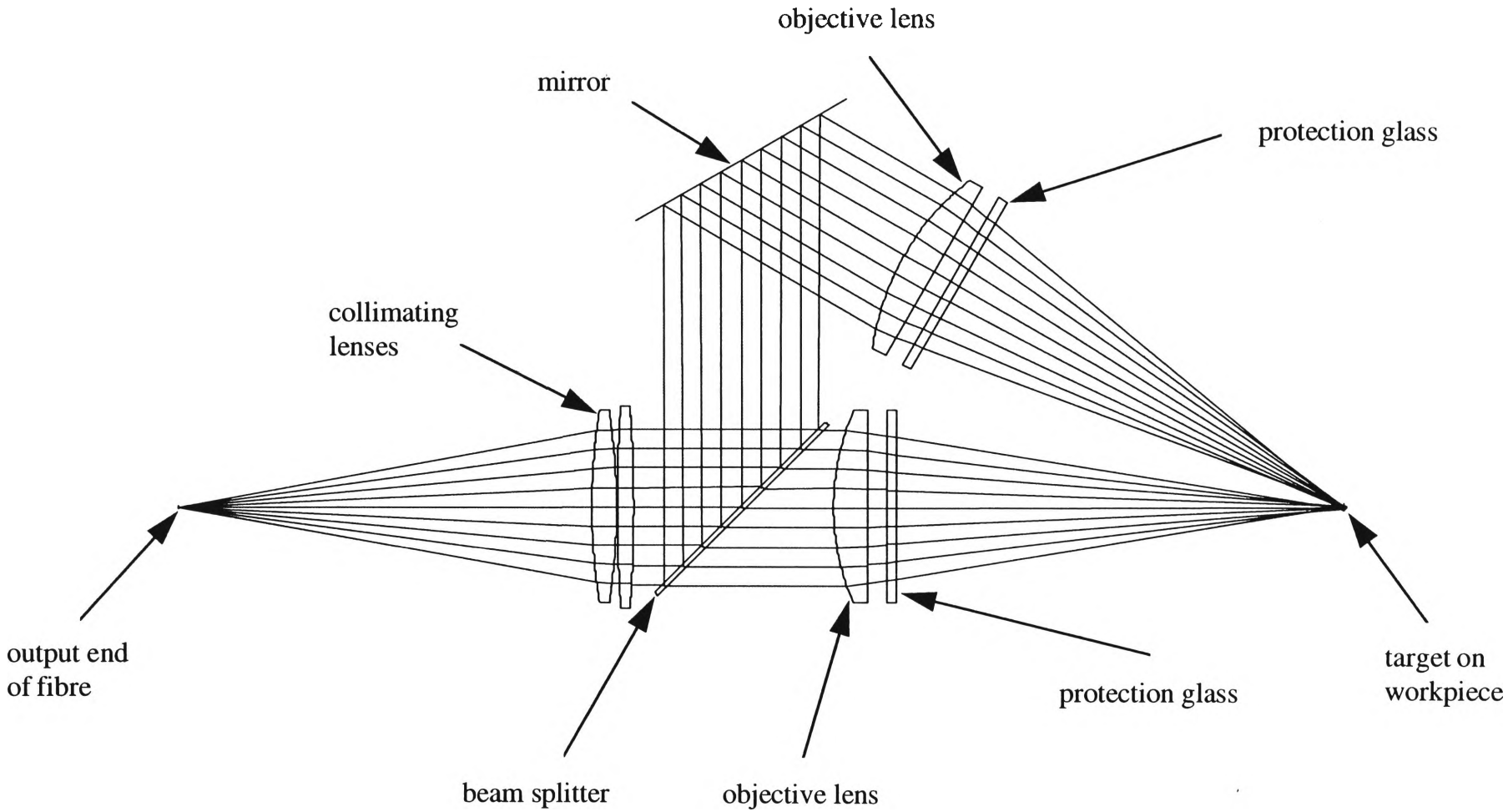

Figure 6.2 Ray diagram showing the optical components of the tandem fibre-optic laser welding head.

CHAPTER 7

CONCLUSIONS

7.1 PRESENT STUDY

The present study involved an experimental and theoretical investigation of fibre-optic pulsed laser welding. Both single-beam and tandem-beam laser radiation were considered. On the basis of this study, the main conclusions are as follows:

1. Three-dimensional finite element models of the heat flow during single- and tandem-beam pulsed laser welding were developed. The main features of each model can be summarised as follows:

    - temperature-dependent thermophysical properties
    - input of experimentally measured beam profiles
    - Beer-Lambert's plasma absorption law
    - convection and radiation to surroundings
    - extension of the parametric design capabilities of the ANSYS program
    - the use of an "effective absorptivity"
    - conduction-limited and keyhole modes.

2. Three-dimensional analytical models of single- and tandem-beam pulsed laser welding were developed to provide a simple and quick check of the numerical models. Owing to the complexity of analytically modelling the temperature rise due to keyhole welding, only the conduction-limited mode of laser welding was modelled. The various development stages of each model were as follows:

    - Rosenthal's instantaneous point source solution
    - stationary Gaussian source solution
    - moving, continuous Gaussian source solution
    - single-beam pulsed laser welding
    - tandem-beam pulsed laser welding.

3. The results of the numerical and analytical models were compared with experimental measurements of fusion zone and weld zone dimensions. Both AISI 1006 steel and A5005 aluminium alloy were modelled. A very good agreement between theory and

experiment for the single-beam laser weld beads was achieved, with minimal assumptions made in the models. This agreement was not as favourable for the tandem-beam conditions selected in the study, although the results clearly demonstrate the importance of the plasma produced during keyhole welding and the inability of the heat conduction model to capture the complexity of the "real" welding process.

4. Full thermal histories of the weldment were generated, and the consequences of such predictions were compared with pyrometric measurements and also correlated with the microconstituents of the welds formed. The measured temperatures were in reasonable agreement with model predictions.

5. Microstructural characterisation of various laser weld beads on AISI 1006 steel, zinc-coated steel ("Zincseal") and zinc-aluminium coated steel ("Zincalume") was performed. Both overlapping and non-overlapping bead configurations were considered. A comparative study of single- and tandem-beam welds by means of various weld assessment techniques was performed. In terms of macrostructural appearance, the main differences between the single- and tandem-beam welds appeared to be in the width of the HAZ and the "smoothness" of the weld bead surface. Under tandem welding conditions, the root HAZ width was generally 1.5 to 2 times larger, indicating much slower cooling rates. The surface of each tandem weld bead tended to be very flat, whereas noticeable peaks and troughs were evident in the single-beam welds. The single-beam welds were more prone to the entrapment of porosity.

6. For AISI 1006 steel, lath martensite (M_L) and fine bainitic ferrite (FS(A)) were observed in the fusion zone under single-beam welding conditions. The introduction of a second laser beam for pre- or post-heating was found to reduce the cooling rate to the extent that bainitic ferrite appeared as the main microconstituent in the FZ. This observation was supported by model predictions.

7. For both single- and tandem-beam conditions, the Zincseal and Zincalume welds revealed very little lath martensite in the FZ. The ferrite stabilisers of zinc and

aluminium resulted in coarse, columnar grains of ferrite within the FZ for Zincalume, while bainitic ferrite was observed for Zincseal.

8. For the single- and tandem-beam welds examined in this work, optical microscopy tended to show only one subregion between the FZ and base metal. This subregion was consistent with the partially-transformed or intercritical region (ICHAZ). Martensite or martensite-austenite (M-A) islands in a ferrite matrix were evident in this region.

9. Optimum butt welding conditions were determined for AISI 1006 steel and the two coated steels. All of the tandem-beam butt joints displayed better formabilities than the corresponding single-beam butt joints. For Zincalume, the difficulty in volatilising the aluminium prior to welding resulted in only a marginal improvement in formability associated with the tandem-beam technique.

10. The experimental, numerical and analytical results have already assisted researchers within the Cooperative Research Centre for Materials Welding and Joining to design a laser processing head. This tandem fibre-optic laser welding head offers the potential to achieve higher weld quality in laser-weldable materials, and to allow the welding of presently difficult-to-weld materials.

7.2 RECOMMENDATIONS FOR FURTHER STUDY

- The most important unresolved issue raised by the foregoing series of experiments and modelling work is the precise role of the plasma during pulsed laser welding. Poorly understood is the relative importance of the partially ionised plasma which is generated in the keyhole compared to the direct absorption at the molten surface of the keyhole by Fresnel absorption. The plasma appears to form an essential part of the process, although if its density becomes either too small or too large, the efficiency of the process decreases. Moreover, no quantitative information is available as to the exact manner in which light is reflected at the walls of the keyhole. Light entering the keyhole is likely to suffer multiple reflections at keyhole walls, as well as scattering effects in the

partially ionised plasma where electrons, atoms and ions scatter radiation to different extents.

- One further issue which has not been explored in the context of the present study is the application of the proposed tandem-beam technique to the welding of aluminium and aluminium alloys. The broad range of coated steels and stainless steels are other prime candidates for this type of investigation. The characterisation of single- and tandem-beam pulsed laser welds of such materials would also play an important role. The use of a tandem laser beam arrangement may enable both pulsed and continuous-wave lasers to successfully weld these materials. As a result, a number of industries would benefit from such improvements, particularly the automotive industry and industries which use the newer alloys of low weldability.

APPENDIX A

DERIVATION OF THE HEAT CONDUCTION EQUATION

APPENDIX A: DERIVATION OF THE HEAT CONDUCTION EQUATION

The heat conduction equation for a moving heat source was employed in both the numerical and analytical models of pulsed laser welding presented in Chapter 5. As this equation represents the basis of each of these models, this appendix presents a full derivation of the equation. The equation is derived by first considering a stationary heat source and the elemental volume for one-dimensional heat conduction shown in Figure A1[143].

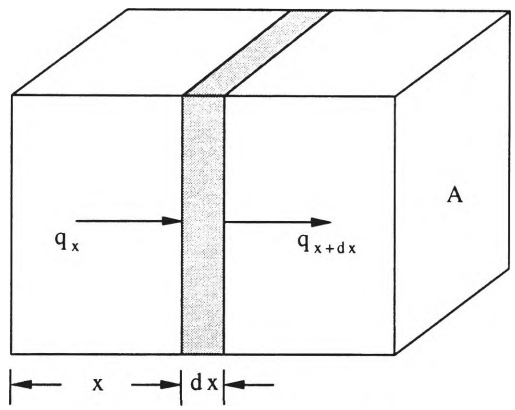

Figure A1 Elemental volume for one-dimensional heat conduction.

For the element of thickness dx, the energy balance is:

rate of energy conducted in left face + rate of energy generated within element

= rate of change in internal energy + rate of energy conducted out right face

(A1)

These quantities are given as follows:

- rate of energy conducted in left face $= q_x = -kA\frac{\partial T}{\partial x}$ (Fourier's law)

(A2)

where:

k = thermal conductivity (W m^{-1} K^{-1})

A = surface area (m^2)

T = temperature (K)

- rate of energy generated within element = qAdx (A3)

- The rate of change in internal energy is obtained by considering the specific heat capacity (c) of the material. This is given by $c = c(T) = dQ_m/dT$, where dQ_m is the heat input per unit mass and dT is the corresponding temperature change.

Multiplying c(T) by the density of the material, ρ(T), and integrating with respect to temperature gives:

$$Q_v = \int_{T_1}^{T} c(\xi)\rho(\xi)\, d\xi \qquad (A4)$$

where Q_v is the quantity of heat necessary to raise a unit volume from temperature T_1 to T.

Assuming c and ρ are constant, differentiating with respect to time and multiplying by Adx gives:

$$\text{- rate of change in internal energy} = \frac{\partial Q_v}{\partial t} Adx = \rho cA \frac{\partial T}{\partial t} dx \qquad (A5)$$

$$\text{- rate of energy out right face} = q_{x+dx} = -kA\frac{\partial T}{\partial x}\bigg)_{x+dx} = q_x + \frac{\partial q}{\partial x} dx$$

(mean value theorem) (A6)

$$\Rightarrow q_{x+dx} = -A\left(k\frac{\partial T}{\partial x} + \frac{\partial}{\partial x}\left(k\frac{\partial T}{\partial x}\right)dx\right) \qquad (A7)$$

Substituting Equations A2, A3, A5 and A7 into equation A1 gives:

$$-kA\frac{\partial T}{\partial x} + qAdx = \rho cA\frac{\partial T}{\partial t}dx - A\left(k\frac{\partial T}{\partial x} + \frac{\partial}{\partial x}\left(k\frac{\partial T}{\partial x}\right)dx\right) \qquad (A8)$$

$$\Rightarrow \frac{\partial}{\partial x}\left(k\frac{\partial T}{\partial x}\right)+q=\rho c\frac{\partial T}{\partial t} \tag{A9}$$

For heat conduction in all three coordinate directions Equation A9 becomes:

$$\frac{\partial}{\partial x}\left(k\frac{\partial T}{\partial x}\right)+\frac{\partial}{\partial y}\left(k\frac{\partial T}{\partial y}\right)+\frac{\partial}{\partial z}\left(k\frac{\partial T}{\partial z}\right)+q=\rho c\frac{\partial T}{\partial t} \tag{A10}$$

Assuming k is constant, Equation A10 simplifies to:

$$\frac{\partial T}{\partial t}-\alpha\nabla^2 T-\frac{q}{\rho c}=0 \tag{A11}$$

$$\text{where } \alpha=\frac{k}{\rho c} \tag{A12}$$

Equation A11 is the heat conduction equation for a stationary heat source. To modify this equation for a moving heat source, consider a quantity of heat which is supplied by a point source moving along the x-axis with a constant velocity v (Figure A2).

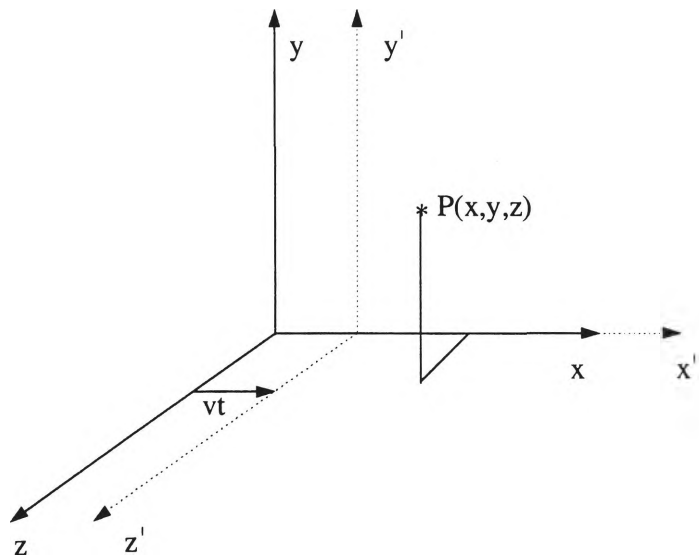

Figure A2 Moving heat source coordinate system.

The point P(x,y,z) at time t in the stationary system becomes P(x', y', z') at time t' in the moving system. Since the translation in the x-direction does not change the other coordinates, y' = y and z' = z. However, $x' = x - vt$. Set t' = t.

It is necessary to transform the variables of the stationary coordinate system where T = f(x,y,z,t). In the new set of variables, T = f(x',y',z',t'). The transformation using the chain rule is therefore:

$$\frac{\partial T}{\partial t} = \frac{\partial T}{\partial x'}\frac{\partial x'}{\partial t} + \frac{\partial T}{\partial t'}\frac{\partial t'}{\partial t} = \frac{\partial T}{\partial x'}(-v) + \frac{\partial T}{\partial t'} \tag{A13}$$

$$\frac{\partial T}{\partial x} = \frac{\partial T}{\partial x'}\frac{\partial x'}{\partial x} = \frac{\partial T}{\partial x'} \tag{A14}$$

$$\frac{\partial T}{\partial y} = \frac{\partial T}{\partial y'}\frac{\partial y'}{\partial y} = \frac{\partial T}{\partial y'} \tag{A15}$$

$$\frac{\partial T}{\partial z} = \frac{\partial T}{\partial z'}\frac{\partial z'}{\partial z} = \frac{\partial T}{\partial z'} \tag{A16}$$

Redefining the moving coordinate system in terms of x, y and z gives the heat conduction equation for a moving heat source:

$$\frac{\partial T}{\partial t} - v\frac{\partial T}{\partial x} - \alpha\nabla^2 T - \frac{q}{\rho c} = 0 \tag{A17}$$

In the present study, the plate or "workpiece" moves in the positive x-direction relative to the stationary heat source(s). This is physically equivalent to the heat source(s) moving in the negative x-direction relative to a stationary workpiece. Equation A17 can be modified accordingly:

$$\frac{\partial T}{\partial t} - v_w\frac{\partial T}{\partial x} - \alpha\nabla^2 T - \frac{q}{\rho c} = 0 \tag{A18}$$

where v_w is the velocity of the workpiece.

APPENDIX B

DERIVATION OF THE ANALYTICAL MODELS OF PULSED LASER WELDING

APPENDIX B: DERIVATION OF THE ANALYTICAL MODELS OF PULSED LASER WELDING

Chapter 5 presented the equations for the temperature increase due to single- and tandem-beam pulsed laser radiation. This appendix presents a full derivation of these equations. The starting point is Rosenthal's instantaneous point source solution.

Instantaneous Point Source

Rosenthal[68] established that the temperature at a point (x,y,z) and time t for an instantaneous point heat source at (x',y',0) and time t' = 0 on a semi-infinite plate is given by:

$$\Delta T = T(x,y,z,t) - T_0 = \frac{q}{4\rho c(\pi\alpha t)^{1.5}} \exp\left(-\frac{(x-x')^2 + (y-y')^2 + z^2}{4\alpha t}\right) \qquad \text{(B1)}$$

where:

T_0 = initial temperature of plate (K)

q = heat input (J)

ρ = density (kg m^{-3})

c = specific heat capacity (J kg^{-1} K^{-1})

α = thermal diffusivity (m^2 s^{-1})

Stationary Gaussian Source

For a Gaussian beam where the beam distribution parameters in the x and y directions are the same, i.e. $\sigma_x = \sigma_y = \sigma$ (m), the heat flux at the surface (J m^{-2}) is given by:

$$q_s = \frac{q}{2\pi\sigma^2}\exp\left(-\frac{x'^2+y'^2}{2\sigma^2}\right) \quad \text{(B2)}$$

$$= \frac{q}{\pi r_c^2}\exp\left(-\frac{r^2}{r_e^2}\right) \quad \text{(B3)}$$

where $r = \sqrt{x'^2+y'^2}$ and $r_e = \sigma\sqrt{2}$, i.e. the distance from the centre of the heat source to the radius at which the heat flux is 1/e times the peak heat flux, $\frac{q}{\pi r_e^2}$ (Figure B1).

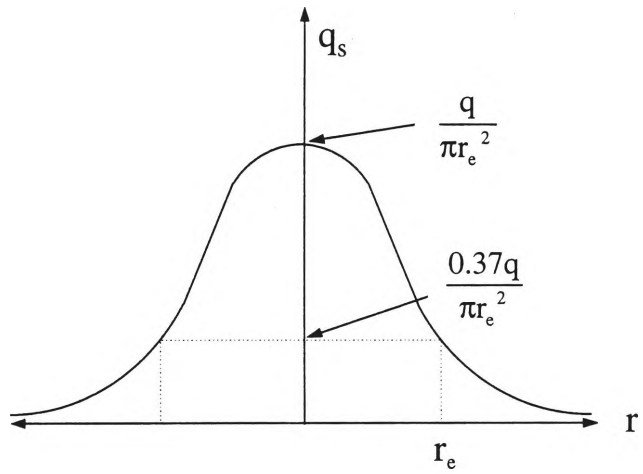

Figure B1 Gaussian distribution.

If the surface is divided into infinitesimally small segments of area dx'dy', the Gaussian heat source can be considered to consist of an infinite number of point heat sources. The temperature increase at (x,y,z) due to a Gaussian heat source can therefore be obtained by summing the contribution from each heat source; i.e. integrating with respect to both x' and y':

$$\Delta T = \int_{-\infty}^{\infty}\int_{-\infty}^{\infty} \frac{q\,dx'\,dy'}{2\pi\sigma^2 4\rho c(\pi\alpha t)^{1.5}} \exp\left(-\frac{x'^2+y'^2}{2\sigma^2}\right)\exp\left(-\frac{(x-x')^2+(y-y')^2+z^2}{4\alpha t}\right) \quad \text{(B4)}$$

Rearranging Equation B4 gives:

$$\Delta T = \frac{q\exp\left(\frac{-z^2}{4\alpha t}\right)}{8\pi\sigma^2\rho c(\pi\alpha t)^{1.5}} \int_{-\infty}^{\infty}\exp\left(-\frac{x'^2}{2\sigma^2}-\frac{(x-x')^2}{4\alpha t}\right)dx' \int_{-\infty}^{\infty}\exp\left(-\frac{y'}{2\sigma^2}-\frac{(y-y')^2}{4\alpha t}\right)dy' \quad \text{(B5)}$$

Both integrals on the right-hand side of Equation B5 can be evaluated using the following identity:

$$\int_{-\infty}^{\infty}\exp\left(-\left(ax'^{2}+2bx'+c\right)\right)dx' = \left[0.5\sqrt{\frac{\pi}{a}}\exp\left(\frac{b^{2}-ac}{a}\right)\operatorname{erf}\left(\sqrt{a}x'+\frac{b}{\sqrt{a}}\right)\right]_{-\infty}^{\infty} \quad ; a \neq 0$$

(Ref. 144) (B6)

$$= \sqrt{\frac{\pi}{a}}\exp\left(\frac{b^{2}-ac}{a}\right) \tag{B7}$$

Rearranging the first integral gives:

$$\int_{-\infty}^{\infty}\exp\left(-\left(\left(\frac{1}{2\sigma^{2}}+\frac{1}{4\alpha t}\right)x'^{2}+2\left(-\frac{x}{4\alpha t}\right)x'+\frac{x^{2}}{4\alpha t}\right)\right)dx'$$

$$= \sqrt{\frac{\pi}{a}}\exp\left(\frac{b^{2}-ac}{a}\right) \tag{B8}$$

where:

$$a = \frac{1}{2\sigma^{2}}+\frac{1}{4\alpha t} \tag{B9}$$

$$b = -\frac{x}{4\alpha t} \tag{B10}$$

$$c = \frac{x^{2}}{4\alpha t} \tag{B11}$$

Simplifying Equation B8 gives:

$$\sqrt{\frac{\pi}{a}}\exp\left(\frac{b^{2}-ac}{a}\right) = \sqrt{\frac{\pi}{a}}\exp\left(\frac{d^{2}-ad}{a}x^{2}\right) \tag{B12}$$

$$\text{where} \quad d = \frac{1}{4\alpha t} \tag{B13}$$

Likewise, the second integral becomes:

$$\int_{-\infty}^{\infty}\exp\left(-\left(\left(\frac{1}{2\sigma^{2}}+\frac{1}{4\alpha t}\right)y'^{2}+2\left(-\frac{y}{4\alpha t}\right)y'+\frac{y^{2}}{4\alpha t}\right)\right)dy'$$

$$= \sqrt{\frac{\pi}{a}}\exp\left(\frac{d^{2}-ad}{a}y^{2}\right) \tag{B14}$$

Substituting Equations B12 and B14 into Equation B5 gives:

$$\Delta T = \frac{q \exp\left(\frac{-z^2}{4\alpha t}\right)}{8a\sigma^2 \rho c(\pi\alpha t)^{1.5}} \exp\left(\frac{d^2 - ad}{a}\left(x^2 + y^2\right)\right) \qquad \text{(B15)}$$

Substituting the expressions for "a" and "d" (B9 and B13) into Equation B15 gives:

$$\Delta T =$$

$$\frac{q}{\rho c} \frac{1}{2\sqrt{\pi\alpha\left(t + t_0\right)}} \exp\left(\frac{-x^2}{4\alpha(t + t_0)}\right) \frac{1}{2\sqrt{\pi\alpha\left(t + t_0\right)}} \exp\left(\frac{-y^2}{4\alpha(t + t_0)}\right) \frac{1}{\sqrt{\pi\alpha t}} \exp\left(\frac{-z^2}{4\alpha t}\right) \qquad \text{(B16)}$$

$$\text{where } t_0 = \frac{\sigma^2}{2\alpha} \qquad \text{(B17)}$$

Equation B16 has the form:

$$\Delta T = \frac{q}{\rho c} f_1(x,t) f_2(y,t) f_3(z,t) \qquad \text{(B18)}$$

where $f_1(x,t)$ and $f_2(y,t)$ are both solutions for a point source in an infinite one-dimensional medium. In each case the point source has already operated for a time, t_0, at time t = 0. $f_3(z,t)$ is the solution for a point source in a one-dimensional semi-infinite medium in which the point source is permitted to operate from time t = 0.

A final rearrangement of Equation B18 gives:

$$\Delta T = \frac{q \exp\left(\frac{-z^2}{4\alpha t}\right)}{4\pi k\left(t + t_0\right)\sqrt{\pi\alpha t}} \exp\left(-\frac{x^2 + y^2}{4\alpha(t + t_0)}\right) \qquad \text{(B19)}$$

Moving, Continuous Gaussian Source

Consider a Gaussian heat source which:

(a) starts moving at (x,y,z) = (0,0,0) and time t = 0 in the positive x-direction with a velocity v; and

(b) operates between time $t = t_s$ and time $t = t_f$ with a power $\dot{q}$.

To determine the temperature increase at a point P(x,y,z), three cases must be considered,viz:

(1) $t \leq t_s$;

(2) $t_s < t \leq t_f$; and

(3) $t > t_f$.

CASE 1 $(t \leq t_s)$

For $t \leq t_s$, $\Delta T = 0$

CASE 2 $(t_s < t \leq t_f)$

The time interval between t_s and t_f can be divided into infinitesimally small intervals dt'. The amount of heat introduced within each interval is therefore $\dot{q}dt'$. Each of these contributions represents a point heat source. Modifying Equation B19 to sum all of these contributions gives:

$$\Delta T = \int_{t_s}^{t} \frac{\dot{q}\exp\left(\frac{-z^2}{4\alpha(t-t')}\right)}{4\pi k(t-t'+t_0)\sqrt{\pi\alpha(t-t')}} \exp\left(-\frac{(x-vt')^2+y^2}{4\alpha(t-t'+t_0)}\right) dt' \qquad \text{(B20)}$$

Let $t'' = t - t'$

$\Rightarrow dt' = -dt''$

Limits of integration

$t'' = t - t_s$, when $t' = t_s$

$t'' = 0$, when $t' = t$

$\Rightarrow \Delta T =$

$$\int_0^{t-t_s} \frac{\dot{q}\exp\left(\frac{-z^2}{4\alpha t''}\right)}{4\pi k(t''+t_0)\sqrt{\pi\alpha t''}} \exp\left(-\frac{(\xi+v(t+t_0)-vt')^2+y^2}{4\alpha(t''+t_0)}\right) dt'' \qquad \text{(B21)}$$

where $\xi = x - v(t + t_0)$ (B22)

$$\Rightarrow \Delta T = \frac{\dot{q}}{4\pi k}\int_0^{t-t_s} \frac{\exp\left(\frac{-z^2}{4\alpha t''}\right)}{(t''+t_0)\sqrt{\pi\alpha t''}} \exp\left(-\frac{(\xi + v(t''+t_0))^2 + y^2}{4\alpha(t''+t_0)}\right) dt'' \quad \text{(B23)}$$

$$= \frac{\dot{q}}{4\pi k\sqrt{\pi\alpha}} \exp\left(-\frac{v\xi}{2\alpha} - \frac{v^2 t_0}{4\alpha}\right)\int_0^{t-t_s} \frac{dt''}{(t''+t_0)\sqrt{t''}} \exp\left(-\frac{\xi^2 + y^2}{4\alpha(t''+t_0)} - \frac{z^2}{4\alpha t''} - \frac{v^2 t''}{4\alpha}\right) \quad \text{(B24)}$$

Equation B24 can be modified into a recognisable form if the substitution $t'' = \eta^2 t_0$ is made.

$$\Rightarrow dt'' = 2\eta t_0 d\eta$$

Limits of integration

$\eta = 0$, when $t'' = 0$

$\eta = \sqrt{\frac{t-t_s}{t_0}}$, when $t'' = t - t_s$

$$\Rightarrow \Delta T = \frac{\dot{q}}{2\pi k\sqrt{\pi\alpha t_0}} \exp\left(-\frac{v\xi}{2\alpha} - \frac{v^2 t_0}{4\alpha}\right)\int_0^{\sqrt{\frac{t-t_s}{t_0}}} \frac{d\eta}{1+\eta^2} \exp\left(-\frac{\xi^2 + y^2}{4\alpha t_0(\eta^2 + 1)} - \frac{z^2}{4\alpha t_0 \eta^2} - \frac{v^2 \eta^2 t_0}{4\alpha}\right) \quad \text{(B25)}$$

$$= \frac{\dot{q}}{2\pi k\sqrt{\pi\alpha t_0}} \exp\left(-\frac{v\xi}{2\alpha} - \frac{v^2 t_0}{4\alpha}\right)\int_0^{\sqrt{\frac{t-t_s}{t_0}}} \frac{d\eta}{1+\eta^2} \exp\left(-\frac{M}{\eta^2 + 1} - \frac{N}{\eta^2} - P\eta^2\right) \quad \text{(B26)}$$

where:

$$M = \frac{\xi^2 + y^2}{4\alpha t_0} \quad \text{(B27)}$$

$$N = \frac{z^2}{4\alpha t_0} \tag{B28}$$

$$P = \frac{v^2 t_0}{4\alpha} \tag{B29}$$

When $t = \infty$ (quasi-steady state),

$$\Delta T = \frac{\dot{q}}{2\pi k\sqrt{\pi\alpha t_0}} \exp\left(-\frac{v\xi}{2\alpha} - \frac{v^2 t_0}{4\alpha}\right)\int_0^{\infty} \frac{d\eta}{1+\eta^2} \exp\left(-\frac{M}{\eta^2+1} - \frac{N}{\eta^2} - P\eta^2\right) \tag{B30}$$

CASE 3 $(t > t_f)$

In this case, the limits of integration in Equation B26 need to be changed as follows:

When $t' = t_s$, $t'' = t - t_s$ and $\eta = \sqrt{\frac{t-t_s}{t_0}}$.

When $t' = t_f$, $t'' = t - t_f$ and $\eta = \sqrt{\frac{t-t_f}{t_0}}$.

$$\Rightarrow \Delta T = \frac{\dot{q}}{2\pi k\sqrt{\pi\alpha t_0}} \exp\left(-\frac{v\xi}{2\alpha} - \frac{v^2 t_0}{4\alpha}\right)\int_{\sqrt{\frac{t-t_f}{t_0}}}^{\sqrt{\frac{t-t_s}{t_0}}} \frac{d\eta}{1+\eta^2} \exp\left(-\frac{M}{\eta^2+1} - \frac{N}{\eta^2} - P\eta^2\right) \tag{B31}$$

Equation B31 must be solved numerically. The iterative use of Simpson's rule was found to provide the desired accuracy within a very few number of steps. Simpson's rule of integration is a piecewise quadratic approximation according to:

$$\int_a^b f(x)dx \approx \frac{h}{3}(f_0 + 4f_1 + 2f_2 + 4f_3 + \ldots + 2f_{2m-2} + 4f_{2m-1} + f_{2m}) \tag{B32}$$

where $h = \left(\frac{b-a}{2m}\right)$ and $f_j = f(x_j)$

A simple Fortran program was written to perform this integration.

Pulsed Laser Welding

For a series of pulses, the temperature rise at a point P(x,y,z) is obtained by summing the temperature rise associated with each pulse. Only the limits of integration change from one pulse to the next. Equation B31 therefore becomes:

$$\Delta T = \frac{\dot{q}}{2\pi k\sqrt{\pi\alpha t_0}} \exp\left(-\frac{v\xi}{2\alpha} - \frac{v^2 t_0}{4\alpha}\right) \sum_{n=1}^{n_{tot}} \int_{a_n}^{b_n} \frac{d\eta}{1+\eta^2} \exp\left(-\frac{M}{\eta^2+1} - \frac{N}{\eta^2} - P\eta^2\right) \tag{B33}$$

The expressions for a_n and b_n in terms of pulse number (n), pulse duration (t_p) and repetition rate (f) are:

$t \le (n-1)/f$:	$a_n = 0$ $b_n = 0$
$(n-1)/f < t \le t_p + (n-1)/f$:	$a_n = 0$ $b_n = \sqrt{\frac{t-(n-1)/f}{t_0}}$
$t > t_p + (n-1)/f$:	$a_n = \sqrt{\frac{t-t_p-(n-1)/f}{t_0}}$ $b_n = \sqrt{\frac{t-(n-1)/f}{t_0}}$

Tandem-Beam Pulsed Laser Welding

Consider two pulsed Gaussian heat sources which are separated by a distance d. Let the first heat source have a peak power density $\dot{q}_1$ and a beam distribution parameter σ_1. At time t = 0, the centre of the first heat source is at (0,0,0). Let the second heat source have a peak power density $\dot{q}_2$ and a beam distribution parameter σ_2. At time t = 0, the

centre of the second heat source is at (d,0,0). Both heat sources are synchronised and move in the positive x-direction with a velocity v.

From Equation B33, the temperature rise at a point P(x,y,z) is therefore:

$$\Delta T = \sum_{m=1}^{2} \frac{\dot{q}_m}{2\pi k\sqrt{\pi\alpha t_m}} \exp\left(-\frac{v\xi_m}{2\alpha} - \frac{v^2 t_m}{4\alpha}\right) \sum_{n=1}^{n_{tot}} \int_{a_{nm}}^{b_{nm}} \frac{d\eta_m}{1+\eta_m^2} \exp\left(-\frac{M_m}{\eta_m^2+1} - \frac{N_m}{\eta_m^2} - P_m\eta_m^2\right) \tag{B34}$$

where:

$$t_1 = \frac{\sigma_1^2}{2\alpha} \qquad t_2 = \frac{\sigma_2^2}{2\alpha} \tag{B35a, B35b}$$

$$\xi_1 = x - v(t+t_1) \qquad \xi_2 = x - d - v(t+t_2) \tag{B36a, B36b}$$

$$M_1 = \frac{\xi_1^2 + y^2}{4\alpha t_1} \qquad M_2 = \frac{\xi_2^2 + y^2}{4\alpha t_2} \tag{B37a, B37b}$$

$$N_1 = \frac{z^2}{4\alpha t_1} \qquad N_2 = \frac{z^2}{4\alpha t_2} \tag{B38a, B38b}$$

$$P_1 = \frac{v^2 t_1}{4\alpha} \qquad P_2 = \frac{v^2 t_2}{4\alpha} \tag{B39a, B39b}$$

$$\eta_1 = \sqrt{\frac{t''}{t_1}} \qquad \eta_2 = \sqrt{\frac{t''}{t_2}} \tag{B40a, B40b}$$

The limits of integration, a_{nm} and b_{nm}, are:

$t \le (n-1)/f$:

$$a_{n1} = 0 \qquad a_{n2} = 0$$
$$b_{n1} = 0 \qquad b_{n2} = 0$$

$(n-1)/f < t \le t_p + (n-1)/f$:

$$a_{n1} = 0 \qquad a_{n2} = 0$$

$$b_{n1} = \sqrt{\frac{t-(n-1)/f}{t_1}} \qquad b_{n2} = \sqrt{\frac{t-(n-1)/f}{t_2}}$$

$t > t_p + (n-1)/f$:

$$a_{n1} = \sqrt{\frac{t-t_p-(n-1)/f}{t_1}} \qquad a_{n2} = \sqrt{\frac{t-t_p-(n-1)/f}{t_2}}$$

$$b_{n1} = \sqrt{\frac{t-(n-1)/f}{t_1}} \qquad b_{n2} = \sqrt{\frac{t-(n-1)/f}{t_2}}$$

REFERENCES

1. Scott, D.A., Frewin, M.R., Baumer, J. and Emms, S.B. Tandem fibre-optic laser welding, Australian Welding Research Report No. 10, Cooperative Research Centre for Materials Welding & Joining and the Welding Technology Institute of Australia, Sydney, Aug. 1995.

2. Bransch, H.N., Wang, Z.Y., Liu, J.T., Weckman, D.C. and Kerr, H.W. "Determining weld quality in pulsed Nd:YAG laser spot welds", *J. Laser Applications*, vol. 3, no. 3, pp. 25-34, 1991.

3. Bransch, H.N. "Welding with high-power pulsed and cw Nd:YAG lasers", *Photonics spectra*, vol. 25, no. 9, pp. 107-112, 1991.

4. Svelto, O. Principles of lasers (ed. D.C. Hanna), 2nd edn, Plenum Press, New York, 1982.

5. Hoult, A.P. "Cutting and welding with high power solid state lasers", in *Proc. Int. Conf. on Advances in Joining and Cutting Processes* (ed. K.I. Johnson), pp. P17-1 to P17-8, Harrogate, Oct./Nov. 1989, Abington Publishing, Cambridge, 1990.

6. Martyr, D.R. "Applying high power lasers to shipbuilding", *Welding Review*, vol. 6, no. 2, pp. 106-114, 1987.

7. Norris, I.M. "High power laser welding of structural steels - current status", in *Proc. Int. Conf. on Advances in Joining and Cutting Processes* (ed. K.I. Johnson), pp. P55-1 to P55-23, Harrogate, Oct./Nov. 1989, Abington Publishing, Cambridge, 1990.

8. Powley, C. and Hoskins, C. "Cut, drill, join and treat - using lasers", *Machinery and Production Engineering*, vol. 150, no. 3838, pp. 22-23, 1992.

9. Wirth, P. "Laser welding in the German automotive industry", in *Proc. Conf. on the Laser vs. the Electron Beam in Welding, Cutting and Surface Treatment* (ed. R. Bakish), pp. 164-170, Reno, Nevada, 1985, Bakish Materials Corp., Englewood, New Jersey, 1985.

10. Nasla, A.S. Welding characteristics of a pulsed 1 kW Nd:YAG laser with fibre optic beam delivery system, Confidential Report No. 436, The Welding Institute, Dec. 1991.

11. Scheuerman, R. "High powered, fibre optic delivered, Nd:YAG, and their application in industry", in *Proc. 26th Int. Symp. on Automotive Technology and Automation*, pp. 89-94, Aachen, Germany, Sep. 1993, Automotive Automation, Croyden, 1993.

12. Tönshoff, H.K., Meyer-Kobbe, C. and Beske, E. "New possibilities in material processing with kW-solid state lasers", in *Proc. High-Power Solid State Lasers and Applications* (ed. C.L. Ireland), vol. 1277, pp. 199-208, SPIE, Bellingham, Washington, 1990.

13. Weber, J. "Laser beam welding with fibre optics heats both sides simultaneously", *Welding Journal*, vol. 67, no. 11, pp. 47-48, 1988.

14. Beck, T., Reng, N. and Richter, K. "Fiber type and quality dictate beam delivery characteristics", *Laser Focus World*, vol. 29, no. 10, pp. 111-115, 1993.

15. Ishide, T., Matsumoto, O., Nagura, Y. and Nagashima, T. "Optical fiber transmission of 2 kW cw YAG laser and its practical application to welding", in *Proc. High-Power Solid State Lasers and Applications* (ed. C.L. Ireland), vol. 1277, pp. 188-198, SPIE, Bellingham, Washington, 1990.

16. Buchholz, J. "Characteristics of flexible fiber cable for transmission of 1 kWatt cw YAG laser radiation for cutting and welding", in *Proc. Beam Diagnostics and Beam Handling Systems* (ed. A. Sona), vol. 1024, pp. 65-70, Hamburg, Germany, Sep. 1988, SPIE, Bellingham, Washington, 1988.

17. Grisoni, L. "Optical fibre Nd-YAG laser beam delivery systems", in *Proc. Beam Diagnostics and Beam Handling Systems* (ed. A. Sona), vol. 1024, pp. 54-64, Hamburg, Germany, Sep. 1988, SPIE, Bellingham, Washington, 1988.

18. Frewin, M.R. and Scott, D.A. "Review of analytical and numerical modelling techniques for continuous and pulsed laser welding", in *Proc. Int. Conf. on Materials in Welding and Joining*, pp. 131-136, Adelaide, Aug. 1995, Institute of Metals and Materials Australasia, Melbourne, 1995.

19. Banas, C. "High power laser welding", in *The Industrial Laser Annual Handbook* (eds D. Belforte and M. Levitt), pp. 69-86, PennWell Books, Tulsa, Oklahoma, 1986.

20. Kimura, S., Nishio, M., Sasaki, M., Nakamura, E. and Takahashi, T. "Welding characteristics with high power CO_2 laser", in *Proc. 5th Int. Conf. on Production Engineering*, pp. 472-477, Tokyo, 1984, Japan Society of Precision Engineering, Tokyo, 1984.

21. LaFlamme, G.R. and Powers, D.E. "A detailed comparison of the EBW and LBW processes", in *Proc. 2nd Int. Conf. on Recent Trends in Welding Science and Technology* (eds S.A. David and J.M. Vitek), pp. 481-485, Gatlinburg, Tennessee, May 1989, ASM Int., Materials Park, Ohio, 1990.

22. Prokhorov, A.M., Konov, V.I., Ursu, I. and Mihailescu, I.N. Laser heating of materials (eds E.R. Pike and W.T. Welford), IOP Publishing, Bristol, 1990.

23. Darchuk, J.M. and Migliore, L.R. "Material and process guidelines help the potential user evaluate laser welding", *Lasers & Applications*, vol. 4, no. 3, pp. 59-66, 1985.

24. Born, M. and Wolf, E. Principles of optics - electromagnetic theory of propagation, interference and diffraction of light, 6th edn, Pergamon Press, Oxford, 1980.

25. Swift-Hook, D.T. and Gick, A.E.F. "Penetration welding with lasers", *Welding Journal*, vol. 52, no. 11, pp. 492s-499s, 1973.

26. Peretz, R. "New parameter correlations for deep penetration welding with high energy focussed beams", *Optics and Lasers in Engineering*, vol. 10, no. 1, pp. 3-16, 1989.

27. Chiang, S. and Albright, C.E. "The limit of joint penetration in high energy density beam welding", *Welding Journal*, vol. 72, no. 3, pp. 117s-121s, 1993.

28. Hoult, A.P., "Welding, cutting and drilling with the 1 kW solid-state oscillator-amplifier laser", in *Proc. 6th Int. Conf. on Lasers in Manufacturing* (ed. W.M. Steen), pp. 23-30, Birmingham, May 1989, IFS Publications, Bedford, 1989.

29. Herziger, G. "Laser material processing", In *Proc. 4th Symp. on Gas Flow and Chemical Lasers* (ed. M. Onorato), pp. 55-57, Stresa, Italy, Sep. 1982, Plenum Press, New York, 1985.

30. Williams, S.W., Salter, P.L., Scott, G. and Harris, S.J. "New welding process for galvanised steel", in *Proc. 26th Int. Symp. on Automotive Technology and Automation*, pp. 49-56, Aachen, Germany, Sep. 1993, Automotive Automation, Croyden, 1993.

31. VanderWert, T. "Low power (1 kW and below) laser welding", in *The Industrial Laser Annual Handbook* (eds D. Belforte and M. Levitt), pp. 58-68, PennWell Books, Tulsa, Oklahoma, 1986.

32. Cremers, D.A., Lewis, G.K. and Korzekwa, D.R. "Measurement of energy deposition during pulsed laser welding", *Welding Journal*, vol. 70, no. 7, pp. 159s-167s, 1991.

33. Eggersglüß, J., Kröhnert, G. and Drube, J. "Welding of thin sheet metals", in *Proc. Laser Assisted Processing* (eds L.D. Laude and G. Rauscher), vol. 1022, pp. 38-42, Hamburg, Germany, Sep. 1988, SPIE, Bellingham, Washington, 1989.

34. Scott, D.A. Tandem fibre-optic laser welding, Australian Welding Research Report No. 9, Cooperative Research Centre for Materials Welding & Joining and the Welding Technology Institute of Australia, Sydney, July 1995.

35. Steen, W.M. Laser material processing, Springer-Verlag, London, 1991.

36. Mannik, L. and Brown, S.K. "A relationship between laser power, penetration depth and welding speed in the laser welding of steels", *J. Laser Applications*, pp. 22-25, vol.2, no. 5, 1990.

37. Dawes, C. Laser welding - a practical guide, Abington Publishing, Cambridge, 1992.

38. Aruga, S., Matsui, E., Okino, K., Takenaka, H., Sato, K., Kyusho, Y. and Washio, K. "Efficient and high-quality overlap welding of car-body aluminium alloy metal sheets with high power Nd:YAG laser by flexible fibre beam delivery", in *Proc. 2nd Conf. on Laser Advanced Material Processing* (eds A. Matsunawa and S. Katayama), pp. 517-522, Niigata, Japan, June 1992, High Temperature Society of Japan, Osaka, Japan, 1992.

39. Tosto, S., Cantello, M., Cruciani, D., Perotti, G., Onorato, M. and Savorelli, P. "Current research into laser welding aluminium alloys", in *Proc. 7th. Int. Symp. on Gas Flow and Chemical Lasers*, vol. 1031, pp. 600-604, Vienna, Austria, Aug. 1988, SPIE, Bellingham, Washington, 1989.

40. Yamaoka, H., Yuki, M., Murayama, T., Tsuchiya, K. and Irisawa, T. "CO_2 laser welding of aluminium A6063 alloy", *Welding Int.*, vol. 6, no. 10, pp. 766-773, 1992.

41. Shaw, L.H. and Cox, M.J. "High aspect ratio Nd/YAG laser welding", in *Proc. Int. Conf. on Advances in Joining and Cutting Processes* (ed. K.I. Johnson), pp. P53-1 to P53-9, Harrogate, Oct./Nov. 1989, Abington Publishing, Cambridge, 1990.

42. Bagger, C., Laursen, S. and Olsen, F. "Comparison of a pulsed CO_2 laser and a pulsed Nd:YAG laser for welding", in *Proc. 11th Int. Cong. on the Applications of Lasers and Electro-Optics* (eds D. Farson, W.M. Steen and I. Miyamoto), vol. 1990, pp. 537-545, Orlando, Florida, Oct. 1992, SPIE, Bellingham, Washington, 1993.

43. Sahoo, P., Collur, M.M. and DebRoy, T. "Effects of oxygen and sulfur on alloying element vaporisation rates during laser welding", *Met. Trans. B*, vol. 19B, no. 12, pp. 967-972, 1988.

44. Hall, B.E. and Wallach, E.R. "The microstructure and properties of autogenous and wire feed laser welds in steel plate", in *Proc. Int. Conf. on Advances in Joining and Cutting Processes* (ed. K.I. Johnson), pp. P21-1 to P21-11, Harrogate, Oct./Nov. 1989, Abington Publishing, Cambridge, 1990.

45. Galsworthy, J.C. and Oakley, P.J. "An assessment of the laser welding of 12 mm thick quenched and tempered steel plate", in *Proc. Int. Conf. on Advances in Joining and Cutting Processes* (ed. K.I. Johnson), pp. P50-1 to P50-15, Harrogate, Oct./Nov. 1989, Abington Publishing, Cambridge, 1990.

46. Metzbower, E.A. "Laser beam welding: thermal profiles and HAZ hardness", *Welding Journal*, vol. 69, no.7, pp. 272s-278s, 1990.

47. International Institute of Welding. Guide to the weldability of C-Mn steels and C-Mn microalloyed steels, Doc. IIS/IIW-382-71, 1971.

48. Van Ooij, W.J., Edwards, R.A. and Neiheisel, G.L. "Cosmetic corrosion of welded hot dip galvanised steel panels", *SAE Trans.*, vol. 100, no. 5, pp. 1266-1280, 1991.

49. Marshall, H.L. "High-power, high-pulse-rate YAG laser seam welding", in *Proc. Industrial Applications of High Power Laser Technology* (ed. J.F. Ready), vol. 86, pp. 60-67, San Diego, Cal., Aug. 1976, SPIE, Bellingham, Washington, 1977.

50. Cremers, D.A., Dixon, R.D., Estler, R.C., Lewis, G.K., Lyman, J.L., Muenchausen, R.E., Nogar, N.S. and Piltch, M.S. "Direct laser-materials interaction", *High Temperature Science*, vol. 27, pp. 439-457, 1990.

51. Washio, K., Takenaka, H., Okino, K., Aruga, S., Matsui, E. and Kyusho, Y. "Welding and cutting car-body metal sheets with fiber delivered output from high power Nd:YAG lasers", *NEC Research and Development*, vol. 33, no. 1, pp. 102-109, 1992.

52. Havrilla, D. and Webber, T. "Laser welding takes the lead", *Lasers and Optronics*, no. 3, pp. 30-40, 1991.

53. Getts, T.J. "Joining external automobile panels", *The Fabricator*, vol. 22, no. 7, p. 108, 1992.

54. Roessler, D.M., Jenuwine, W.C., Koons, J.N. and Speranza, J.J. "Laser material processing in General Motors Corporation", in *Proc. 25th. Int. Symp. on Automotive Technology and Automation*, pp. 37-51, Florence, Italy, June 1992, Automotive Automation, Croydon, 1992.

55. Norris, I.M., Hoult, M., Peters, C. and Wileman, P. "Materials processing with a 3 kW Nd:YAG laser", in *Proc. 2nd Conf. on Laser Advanced Material Processing* (eds A. Matsunawa and S. Katayama), pp. 489-494, Niigata, Japan, June 1992, High Temperature Society of Japan, Osaka, Japan, 1992.

56. Heyden, J., Nilsson, K. and Magnusson, C. "Laser welding of zinc coated steel", in *Proc. 5th Int. Conf. of Lasers in Manufacturing* (ed. H. Hügel), pp. 195-206, Stuttgart, Germany, Sep. 1988, IFS Publications, Bedford, 1988.

57. Bode, R., Giesel, D., Selige, A. and Warneke, W. "Thyssen Stahl - a partner for automotive steel sheet", *Steel Times Int.*, vol. 14, no. 2, pp. 14-17, 1990.

58. Irving, B. "Will the YAG laser revolutionise automotive manufacturing?", *Welding Journal*, vol. 72, no. 7, pp. 52-56, 1993.

59. Masumoto, I., Shinoda, T. and Ishiyama, H. "Application of laser beam welding to thin steel sheet", *Trans. Japan Welding Society*, vol. 20, no. 2, pp. 50-55, 1989.

60. Salminen, A.S., Moisio, T.J.I. and Martikainen, J.K. "Design for laser-welded products", in *Proc. 8th Int. Cong. on the Applications of Lasers and Electro-*

Optics (ed. M. Long), vol. 1404, pp. 75-84, Orlando, Florida, Oct. 1989, Bellingham, Washington, 1989.

61. Neiheisel, G. and Cary, R. "From scrap reclamation to tailored blanks", *Industrial Laser Review*, vol. 6, no. 6, pp. 5-9, 1991.

62. Uddin, M.N. "How laser welding is changing the auto industry", *Industrial Laser Review*, pp. 11-14, vol. 6, no. 2, 1991.

63. Wang, P.-C. "Calculation of laser weld specification for automotive sheet steel", *General Motors Research Laboratories Publication*, pp. 1-18, June 1991.

64. Porter, C.A. "Producing sheet metal blanks using lasers", *The Fabricator*, vol. 22, no. 7, pp. 98-102, 1992.

65. Ayres, K.R. and Hilton, P.A. "CO_2 laser butt welding of coated steels for the automotive industry", in *Proc. 26th Int. Symp. on Automotive Technology and Automation*, pp. 65-72, Aachen, Germany, Sep. 1993, Automotive Automation, Croyden, 1993.

66. Larsson, J.K. "One decade of experience from laser materials processing - a powerful foundation for improved product quality", in *Proc. 26th Int. Symp. on Automotive Technology and Automation*, pp. 29-40, Aachen, Germany, Sep. 1993, Automotive Automation, Croyden, 1993.

67. Goldak, J., Bibby, M., Moore, J., House, R. and Patel, B. "Computer modelling of heat flow in welds", *Met. Trans. B*, vol. 17B, no. 9, pp. 587-600, 1986.

68. Rosenthal, D. "The theory of moving sources of heat and its application to metal treatments", *Trans. ASME*, vol. 43, no. 11, pp. 849-866, 1946.

69. Klemens, P.G. "Heat balance and flow conditions for electron beam and laser welding", *J. Appl. Phys.*, vol. 47, no. 5, pp. 2165-2174, 1976.

70. Andrews, J.G. and Atthey, D.R. "Hydrodynamic limit to penetration of a material by a high-power beam", *J. Phys. D: Appl. Phys.*, vol. 9, pp. 2181-2194, 1976.

71. Cline, H.E. and Anthony, T.R. "Heat treating and melting material with a scanning laser or electron beam", *J. Appl. Phys.*, vol. 48, no. 9, pp. 3895-3900, 1977.

72. Davis, M., Kapadia, P. and Dowden, J. "Modelling the fluid flow in laser beam welding", *Welding Journal*, vol. 65, no. 7, pp. 167s-174s, 1986.

73. Weckman, D.C., Mallory, L.C. and Kerr, H.W. "A technique for the prediction of average weld pool width and depth for GTA welds on stainless steels", *Zeitschrift für Metallkunde*, vol. 80, no. 7, pp. 459-468, 1989.

74. Steen, W.M., Dowden, J., Davis, M. and Kapadia, P. "A point and line source model of laser keyhole welding", *J. Phys. D: Appl. Phys.*, vol. 21, pp. 1255-1260, 1988.

75. Akhter, R., Davis, M., Dowden, J., Kapadia, P., Ley, M. and Steen, W.M. "A method for calculating the fused zone profile for laser keyhole welds", *J. Phys. D: Appl. Phys.*, vol. 22, pp. 23-28, 1989.

76. Dowden, J., Kapadia, P. and Postacioglu, N. "An analysis of the laser-plasma interaction in laser keyhole welding", *J. Phys. D: Appl. Phys.*, vol. 22, pp. 741-749, 1989.

77. Finke, B.R., Kapadia, P.D. and Dowden, J.M. "A fundamental plasma based model for energy transfer in laser material processing", *J. Phys. D: Appl. Phys.*, vol. 23, pp. 643-654, 1990.

78. Tosto, S. "Modelling of the thermal field induced by laser irradiation in the presence of heat sinks or sources", *Lasers in Engineering*, vol. 2, no. 1, pp. 61-74, 1993.

79. Kaplan, A. "A model of deep penetration laser welding based on calculation of the keyhole profile", *J. Phys. D: Appl. Phys.*, vol. 27, pp. 1805-1814, 1994.

80. Tayal, M.J. Laser surface treatment of steel using Nd:YAG laser, PhD Dissertation, Michigan State University, Michigan, 1992.

81. Mazumder, J. and Steen, W.M. "Heat transfer model for cw laser material processing", *J. Appl. Phys.*, vol. 51, no. 2, pp. 941-947, 1980.

82. Chan, C., Mazumder, J. and Chen, M.M. "A two-dimensional transient model for convection in laser melted pool", *Met. Trans. A*, vol. 15A, no. 12, pp. 2175-2184, 1984.

83. Paul, A. and DebRoy, T. "Free surface flow and heat transfer in conduction mode laser welding", *Met. Trans. B*, vol. 19B, no. 12, pp. 851-858, 1988.

84. Molino, G., Penasa, M., Perlini, G., Tiziani, A. and Zambon, A. "Thermal modelling of the laser welding process using a realistic power distribution of the beam", in *Proc. 3rd European Conference on Laser Treatment of Materials* (eds H. Bergmann and R. Kupfer), pp. 195-205, Erlangen, Germany, Sep. 1990, Sprechsaal Publishing, Coburg, Germany, 1990.

85. Gratzke, U., Kapadia, P.D. and Dowden, J. "Heat conduction in high speed laser welding", *J. Appl. Phys. D: Appl. Phys.*, vol. 24, pp. 2125-2134, 1991.

86. Aden, M., Beyer, E., Herziger, G. and Kunze, H. "Laser-induced vaporization of a metal surface", *J. Phys. D: Appl. Phys.*, vol. 25, pp. 57-65, 1992.

87. Dowden, J., Chang, W., Kapadia, P. and Strange, C. "Dynamics of the vapour flow in penetration welding with a laser at medium welding speeds", *J. Phys. D: Appl. Phys.*, vol. 24, pp. 519-532, 1991.

88. Bechtel, J.H. "Heating of solid targets with laser pulses", *J. Appl. Phys.*, vol. 46, no. 4, pp. 1585-1593, 1975.

89. Zacharia, T., David, S.A., Vitek, J.M. and DebRoy, T. "Heat transfer during Nd:YAG pulsed laser welding and its effect on solidification structure of austenitic stainless steels", *Met. Trans. A* , vol. 20A, no. 5, pp. 957-967, 1989.

90. Russo, A.J., Akau, R.L. and Jellison, J.L. "Thermocapillary flow in pulsed laser beam weld pools", *Welding Journal*, vol. 69, no. 1, pp. 23s-29s, 1990.

91. Vishnu, P.R., Li, W.B. and Easterling, K.E. "Heat flow model for pulsed welding", *J. Materials Science and Technology*, vol. 7, no. 7, pp. 649-659, 1991.

92. Gellert, B. and Egli, W. "Melting of copper by an intense and pulsed heat source", *J. Phys. D: Appl. Phys.*, vol. 21, pp. 1721-1726, 1988.

93. Jette, A.N. and Benson, R.C. "Modelling of pulsed-laser cleaning of metal optical surfaces at cryogenic temperatures", *J. Appl. Phys.*, vol. 75, no. 6, pp. 3130-3141, 1994.

94. Arutyunyan, R.V., Baranov, V.Y., Bol'shov, L.A., Malyuta, D.D., Mezhevov, V.S. and Pis'mennyi, V.D. "Thermohydrodynamic models of the interaction of pulsed-periodic radiation with matter", *Soviet J. Quantum Electronics*, vol. 17, no. 2, pp. 163-168, 1987.

95. Frewin, M.R. and Scott, D.A. "Laser Welding, Part I - Review of analytical and numerical modelling techniques for continuous and pulsed laser welding", submitted to *Welding Journal*, June 1997.

96. Von Allmen, M., Blaser, P., Affolter, K. and Stürmer, E. "Absorption phenomena in metal drilling with Nd-lasers", *IEEE. J. Quantum Electronics*, vol. 14, no. 2, pp. 85-88, 1978.

97. Steen, W.M. "Arc augmented laser processing of materials", *J. Appl. Phys.*, vol. 52, no. 11, pp. 5636-5641, 1980.

98. Brite/Euram Project BE-3037. "Plasma and laser enhanced arc welding for automatic application", J. Wendelstorf (coordinator), Braunschweig, Germany, 1990.

99. Matsuda, J., Utsumi, A., Katsumura, M., Hamasaki, M. and Nagata, S. "TIG or MIG arc augmented laser welding of thick mild steel plate", *Joining & Materials*, vol. 1, no. 1, pp. 31-34, 1988.

100. Grünenwald, B., Shen, J., Dausinger, F. and Hügel, H. "Laser cladding with composite powders using temperature control and beam combining", in *Proc. 26th Int. Symp. on Automotive Technology and Automation*, pp. 287-294, Aachen, Germany, Sep. 1993, Automotive Automation, Croyden, 1993.

101. Killpatrick, D. "Laser beam shaping takes the next step", *Industrial Laser Review*, vol. 8, no. 7, p. 18, 1993.

102. Belforte, D.A. "Solution to split beam metal cutting", *Industrial Laser Review*, vol. 8, no. 12, pp. 6-7, 1993.

103. Belforte, D.A. "Shaping laser beams", *Industrial Laser Review*, vol. 8, no. 12, pp. 7-8, 1993.

104. Banas, C. "High-power production lasers", *Industrial Laser Review*, vol. 7, no. 2, pp. 5-9, 1992.

105. Glumann, C., Rapp, J., Bea, M., Dausinger, F. and Hügel, H. "Combination of two high power lasers - a new dimension in laser materials processing", in *Proc. 26th Int. Symp. on Automotive Technology and Automation*, pp. 239-246, Aachen, Germany, Sep. 1993, Automotive Automation, Croyden, 1993.

106. Kannatey-Asibu, E. "Split-beam laser welding", in *Proc. 2nd Int. Conf. on Recent Trends in Welding Science and Technology* (eds S.A. David and J.M. Vitek), pp. 443-451, Gatlinburg, Tennessee, May 1989, ASM Int., Materials Park, Ohio, 1990.

107. Kannatey-Asibu, E. "Thermal aspects of the split-beam laser welding concept", *J. Engineering Materials and Technology*, vol. 113, no. 2, pp. 215-221, 1991.

108. Liu, Y.-N. and Kannatey-Asibu, E. "Laser beam welding with simultaneous Gaussian laser preheating", *Trans. ASME*, vol. 115, no. 1, pp. 34-41, 1993.

109. Okada, A., Kasugai, T., Ei, K., Muramatsu, Y., Hiraoka, K. and Inagaki, M. "CCT diagram data base system by interactive personal computer", *Trans. National Research Institute for Metals*, vol. 29, no. 1, pp. 15-20, 1987.

110. *Proc. 11th Int. Cong. on the Applications of Lasers and Electro-Optics* (eds D. Farson, W.M. Steen and I. Miyamoto), vol. 1990, Orlando, Florida, Oct. 1992, SPIE, Bellingham, Washington, 1993.

111. Chen, Z.D., West, D.R.F. and Steen, W.M. "Laser melting of alloy cast irons", in *Proc. 5th Int. Cong. on Applications of Lasers and Electro-Optics* (eds C.M. Banas and G.L. Whitney), pp. 27-35, Arlington, Virginia, Nov. 1986, IFS Publications, Bedford, 1987.

112. Stoop, J. and Metzbower, E.A. "A metallurgical characterisation of HY-130 steel welds", *Welding Journal*, vol. 57, no. 11, pp. 345-353, 1978.

113. Thaulow, C., Paauw, A.J. and Guttormson, K. "The heat-affected zone toughness of low-carbon microalloyed steels", *Welding Journal*, vol. 66, no. 9, pp. 266s-279s, 1987.

114. Vitek, J.M., Dasgupta, A. and David, S.A. "Microstructural modification of austenitic stainless steels by rapid solidification", *Met. Trans. A*, vol. 14A, no. 9, pp. 1833-1841, 1983.

115. Savage, W.F., Lundin, C.D. and Aronson, A.H. "Weld metal solidification mechanics", *Welding Journal*, vol. 44, no. 4, pp. 175s-181s, 1965.

116. Lancaster, J.F. Metallurgy of welding (ed. M. Dunn), 5th edn, Chapman & Hall, London, 1993.

117. Jones, H. Rapid solidification of metals and alloys, Chameleon Press, London, 1982.

118. Harrison, P.L. and Farrar, R.A. "Application of continuous cooling transformation diagrams for welding of steels", *Int. Materials Review*, vol. 34, no. 1, pp. 35-51, 1989.

119. Kenny, B.G., Kerr, H.W., Lazor, R.B. and Graville, B. "Ferrite transformation characteristics and CCT diagrams in weld metals", *Metal Construction*, vol. 17, no. 6, pp. 374R-381R, 1985.

120. Coyle, R.J. "A microstructural study of pulsed and continuous laser welded stainless steel", in *Proc. Lasers in Materials Processing* (ed. E.A. Metzbower), pp. 185-194, L.A., Cal., Jan. 1983, ASM, Metals Park, Ohio, 1983.

121. Degenkolbe, J., Uwer, D. and Wegmann, H.G. "Characterisation of weld thermal cycles with regard to their effect on the mechanical properties of welded joints by the cooling time $t_{8/5}$ and its determination", *Thyssen Technische Berichte*, Heft 1, pp. 57-73, 1985.

122. Scott, D.A. Tandem fibre-optic laser welding head, CRC Final Report, Project 93-16, July 1997.

123. Standards for Australian Aluminium Mill Products, part 1, p. 7, The Aluminium Development Council of Australia, Sydney, 1968.

124. Annual Book of ASTM standards, Section 3 - Metals Test Methods and Analytical Procedures, volume 3.01, p. 157, American Society for Testing and Materials, Philadelphia, 1993.

125. Annual Book of ASTM standards, Section 3 - Metals Test Methods and Analytical Procedures, volume 3.01, pp. 668-670, American Society for Testing and Materials, Philadelphia, 1993.

126. Grange, R.A., Hribal, C.R. and Porter, L.F. "Hardness of tempered martensite in carbon and low-alloy steels", *Met. Trans. A*, vol. 8A, no. 11, pp. 1775-1785, 1977.

127. Bhadeshia, H.K.D.H. and Svensson, L.-E. "Modelling the evolution of microstructure in steel weld metal", in *Mathematical Modelling of Weld Phenomena* (eds H. Cerjak and K.E. Easterling), pp. 109-180, The Institute of Materials, London, 1993.

128. Fredriksson, H. "Segregation phenomena in Fe-base alloys", *Scand. J. of Met.*, vol. 5, no. 1, pp. 27-32, 1976.

129. International Institute of Welding, IIW Doc. 835-85, 1985; also in *Welding in the World*, vol. 24, no. 7/8, p. 144, 1986.

130. Atlas for Bainitic Microstructures, vol. 1, Bainite Committee of Iron and Steel Institute of Japan, 1992.

131. Laughlin, D.E., Sekerko, R.F. and Waymon, C.M. Solid-state phase transformations (ed. H. Aaronson), TMS-AIME, Warrendale, Penn., 1982.

132. Easterling, K. Introduction to the Physical Metallurgy of Welding, 2nd edn, Butterworth-Heinemann, Oxford, 1992.

133. Nishioka, K. and Tamehiro, H. "High strength titanium-oxide bearing line pipe steel for low-temperature service", in *Proc. Int. Conf. on Microalloyed HSLA Steels*, pp. 24-30, Chicago, Illinois, Sep. 1988, ASM, Metals Park, Ohio, 1988.

134. Alloying Elements in Steel (eds E.C. Bain and H.W. Paxton), 2nd edn, ASM, Metals Park, Ohio, 1961.

135. Duley. W.W. "A summary of beam material interactions during laser processing", in *Proc. Int. Conf. on Laser Advanced Materials Processing*, pp. 19-24, Osaka, Japan, May 1987, High Temperature Society of Japan, Osaka, Japan, 1987.

136. Brown, S. and Song, H. "Finite element simulation of welding of large structures", *J. Eng. Ind.*, vol. 114, no. 11, pp. 441-451, 1992.

137. Kim, C.S. Thermophysical properties of stainless steels, Technical Report ANL-75-55, Argonne National Laboratory, Argonne, Illinois, 1975.

138. Material properties of A5005 alloy, supplied by K & K associates on the world-wide web, http://www.kkassoc.com/~takinfo/prop1.htm.

139. Vinokurov, V.A. Welding Stresses and Distortion, trans. by J.E. Baker (ed. The Welding Institute, Abington, Cambridge), pp. 118-119, The British Library, Boston Spa, England, 1977.

140. ANSYS Revision 5.0 User Manual, Swanson Analysis Systems, pp. 31-34, 1992.

141. Frewin, M.R., Dunne, D.P. and Scott, D.A. "Microstructural characterisation of pulsed Nd:YAG laser welds in AISI 1006 steel", pp. 39-44, Sydney, May 1996, Institute of Metals and Materials Australasia, Melbourne, 1996.

142. Xie, J. and Kar. A. "Mathematical modelling of melting during laser materials processing", *J. Appl. Phys.*, vol. 81, no. 7, pp. 3015-3022, 1997.

143. Carslaw, H.S. and Jaeger, J.C. Conduction of heat in solids, 2nd edn, pp. 6-15, Oxford Science Publications, Oxford, 1959.

144. Abramowitz, M. and Stegun, I.A. Handbook of mathematical functions, 3rd edn, p. 303, U.S. Government Printing Office, Wash., D.C., 1965.

Form 1

UNIVERSITY OF WOLLONGONG

DECLARATION RELATING TO DISPOSITION OF THESIS - PhD

This is to certify that I ..... MICHAEL RICHARD FREWIN .....

being a candidate for the degree of ..... PhD .....

am fully aware of the policy of the University relating to the retention and use of higher degree theses, namely that the University retains a copy of any thesis submitted for examination and that the University holds that no thesis submitted for a higher degree should be retained in the library for record purposes only but, within copyright privileges of the author, should be public property and accessible for consultation at the discretion of the Librarian.

In the light of these provisions I grant the University Librarian permission to publish or to authorise publication of my thesis in whole or in part, or grant access to it, as he deems fit.

I also authorise publication by University Microfilms of a 350 word abstract in Dissertation Abstracts International (DAI).

Signature ..... M. Frewin .....

Witness .....

Date ..... 28/7/97 .....